

EXPERIMENTAL STUDIES OF GEOCHEMICAL REACTIONS THAT AFFECT
THE MOBILITY OF METALS AND NANOPARTICLES OF ENVIRONMENTAL
INTEREST

A Dissertation

Submitted to the Graduate School
of the University of Notre Dame
in Partial Fulfillment of the Requirements
for the Degree of

Doctor of Philosophy

by

Lindsay Ann Seders

Jeremy B. Fein, Director

Graduate Program in Civil Engineering and Geological Sciences

Notre Dame, Indiana

October 2010

©Copyright 2010

Lindsay Ann Seders

EXPERIMENTAL STUDIES OF GEOCHEMICAL REACTIONS THAT AFFECT
THE MOBILITY OF METALS AND NANOPARTICLES OF ENVIRONMENTAL
INTEREST

Abstract

by

Lindsay Ann Seders

Adsorption and adhesion of metals and engineered nanoparticles onto geosorbents can have a significant impact on their fate and transport. Interactions with fixed mineral and bacterial surfaces may remove contaminants from solution and decrease their mobility, although removal may be selective. Conversely, when the surfaces themselves are mobile as colloids, the transport of contaminants may be enhanced by adsorption and adhesion reactions. Natural organic matter (NOM), a complex mixture of organic molecules, is widespread in environmental systems and can influence adsorption and adhesion through aqueous and surface complexation reactions. This research focuses on the interactions of NOM, cadmium (Cd(II)), and nanoparticles with geosorbents, as well as the potential reactivity of bacterial exudates, under a range of aqueous conditions. Three experimental studies will be described: 1) flow-through column experiments to study the effects of NOM on Cd(II) mobility and of Cd(II) on NOM sorptive fractionation in various types of mineral sands; 2) an investigation of influence of pH,

nanoparticle size, and nanoparticle concentration on the adhesion of titanium dioxide nanoparticles to silica and iron-coated silica grains; and 3) the use of potentiometric titrations and chemical equilibrium modeling to evaluate the proton binding of bacterial exudates collected from Gram-positive (*Bacillus subtilis*) and Gram-negative (*Shewanella oneidensis*) bacterial species. From the results of these laboratory studies, it is possible to better understand contaminant mobility in realistic geologic systems.

CONTENTS

Figures.....	v
Tables.....	viii
Acknowledgments.....	ix
Chapter 1: Introduction.....	1
1.1. Overview.....	1
1.2. Background.....	2
1.2.1. Mobility of Natural Organic Matter and Cadmium.....	2
1.2.2. TiO ₂ Nanoparticle Adhesion to Geosorbents.....	4
1.2.3. Proton Binding of Bacterial Exudates.....	6
Chapter 2: Mobility of Cd(II) and Natural Organic Matter through Naturally Nanoparticle-Coated Sands.....	8
2.1. Introduction.....	8
2.2. Materials and Methods.....	10
2.2.1. Natural Organic Matter and Geosorbents.....	10
2.2.2. Geosorbent Characterization.....	11
2.2.3. Sample Solutions and Columns.....	11
2.2.4. UV/vis Analysis.....	13
2.2.5. ICP-OES and HPSEC Measurements.....	14
2.3. Results and Discussion.....	15
2.3.1. Characteristics of the Geosorbents.....	15
2.3.2. Ionic Strength and pH Effects.....	15
2.3.3. Cadmium.....	24
2.4. Conclusions.....	27
Chapter 3: Experimental Study of TiO ₂ Nanoparticle Adhesion to Silica and Fe(III) Oxide-Coated Silica Surfaces.....	29
3.1. Introduction.....	29
3.2. Materials and Methods.....	32
3.2.1. Nanoparticles and Geosorbents.....	32
3.2.2. Sorbent Characterization.....	33
3.2.3. Batch Experiments.....	34
3.2.4. UV/vis Analysis.....	35

3.2.5. Adhesion Isotherm Calculations	39
3.3. Results and Discussion	41
3.3.1. UV/vis Absorbance Profiles	41
3.3.1.1. Uncoated Silica Grains	41
3.3.1.2. Iron-Coated Silica Grains	46
3.3.2. TiO ₂ Adhesion	46
3.3.2.1. Uncoated Silica Grains	46
3.3.2.2. Iron-Coated Silica Grains	52
3.3.2.3. TiO ₂ Adhesion Isotherms.....	55
3.4. Conclusions.....	61
Chapter 4: Proton Binding of Bacterial Exudates Determined through Potentiometric Titrations	63
4.1. Introduction.....	63
4.2. Materials and Methods.....	65
4.2.1. Experimental.....	65
4.2.1.1. Bacterial Growth and Exudate Preparation.....	65
4.2.1.2. Potentiometric Titrations	66
4.2.2. Chemical Equilibrium Modeling	67
4.3. Results and Discussion	69
4.3.1. Exudate Solutions	69
4.3.2. Exudate Titrations.....	72
4.3.3. Titration Modeling.....	79
4.4. Conclusions.....	91
Chapter 5: Conclusions.....	93
Appendix A: Breakthrough Curves, Absorbance Ratios, and Molecular Weight Distributions.....	97
A.1 Comparison of 254, 280, and 350 nm NOM Breakthrough Curves in Oyster Sand	97
A.2 Hematite and Corundum Breakthrough Curves.....	102
A.3 Comparison Breakthrough Curves.....	104
A.4 280 nm/254 nm Absorbance Ratios	105
A.5 350 nm/254 nm Absorbance Ratios	107
A.6 Influent Molecular Weight Distributions as a Function of pH	109
A.7 Retained NOM Molecular Weight Distributions	110
A.8 Cd(II) Breakthrough Curves	112
A.9 280 nm/254 nm Absorbance Ratios with Cd	113
A.10 350 nm/254 nm Absorbance Ratios with Cd	114
A.11 Retained NOM Molecular Weight Distributions with Cd	115
Appendix B: Absorbance and Adhesion Data	117
B.1 Control Experiments	117
B.2 TiO ₂ Adhesion onto Uncoated and Fe-Coated Silica.....	119

Appendix C: Calculated Values from Exudate Titrations	121
References.....	125

FIGURES

- Figure 2.1: NOM retention on Oyster sand increased as a function of ionic strength at a) pH 5 and b) pH 8. Gray bars represent effluent sampling times for HPSEC analysis..... 17
- Figure 2.2: NOM retention at 0.001 M as a function of pH. Similar retention was observed at pH 5 and 6 and at pH 7 and 8; overall retention decreased with increasing pH. Gray bars represent effluent sampling times for HPSEC analysis. 18
- Figure 2.3: MW distributions of NOM retained in the column at each sampling period compared to the influent MW distribution from experiments conducted with 5 ppm C at pH 6 in 0.01 M NaClO₄. Dashed vertical line represents the MW peak of the influent solution..... 21
- Figure 2.4: MW distributions of the ‘total’ effluent NOM (black lines) and ‘total’ adsorbed NOM (gray lines) of the four HPSEC samples for each of the 5 ppm C experiments at pH 6 or 8 in 0.001 M NaClO₄ and 0.01 M NaClO₄ with or without Cd. The black vertical line represents the peak log MW of the influent solution. 22
- Figure 2.5: 5 ppm C NOM increased Cd adsorption onto Oyster sand in 0.01 M NaClO₄ at pH 8 but only slightly at pH 5..... 25
- Figure 2.6: Cd slightly decreased NOM adsorption onto Oyster sand in 0.01 M NaClO₄ at pH 8 but not 5. Gray bars represent effluent sampling times for HPSEC analysis. 26
- Figure 3.1: a) pH dependence of the 50 mg/L standards for the 26 nm TiO₂ particles from pH 3-8. b) Particle size dependence of the 50 mg/L standards at pH 4..... 37
- Figure 3.2: 50 nm TiO₂ standards (in mg/L) at pH 3 are shown as black solid curves. The dashed curve is the absorbance profile for the 200 mg/L 50 nm TiO₂ suspension after it was exposed to silica particles at pH 3. Note the agreement in the shapes of the absorbance profiles. 42

Figure 3.3: a) 50 nm TiO₂ standards (in mg/L) at pH 4 are shown as black solid curves. The dashed curve is the absorbance profile of the 200 mg/L 50 nm TiO₂ suspension after it was exposed to silica particles at pH 4. b) 16 nm TiO₂ standards (in mg/L) at pH 4 are shown as gray solid curves. The dashed curve is the absorbance profile of the 200 mg/L 50 nm TiO₂ suspension after it was exposed to silica particles at pH 4..... 43

Figure 3.4: 50 nm TiO₂ standards (in mg/L) at pH 7 are shown as black solid curves. The dashed curve is the absorbance profile of the 200 mg/L 50 nm TiO₂ suspension after it was exposed to silica particles at pH 7..... 45

Figure 3.5: TiO₂ nanoparticle adhesion to uncoated silica grains at pH 3-8 (a-f). Open squares represent the 50 nm TiO₂, black diamonds the 26 nm TiO₂, and gray triangles the 16 nm TiO₂. The black line represents 100% adhesion. In cases where adhesion was close to the detection limit, the data are not presented. 48

Figure 3.6: The extent of nanoparticle adhesion onto uncoated silica grains as a function of pH, shown for all three TiO₂ nanoparticle sizes at two initial concentrations: a) 115 mg/L and b) 175 mg/L. 51

Figure 3.7: The extent of 26 nm TiO₂ adhesion onto uncoated and Fe-coated silica grains as a function of pH at two initial concentrations: a) 115 mg/L and b) 175 mg/L.52

Figure 3.8: a) Adhesion isotherms from experiments involving uncoated silica grains at pH 5 for all three nanoparticle sizes. The experimental data are shown as squares (50 nm), diamonds (26 nm), and triangles (16 nm). The calculated Langmuir isotherms are shown as the black (26 nm) and gray (16 nm) lines, and the K_d fit is the dashed line (50 nm). b) The Langmuir linearization of the 26 nm experimental data at pH 5 with the calculated linear regression equation..... 56

Figure 3.9: K (either K_L or K_d ; see Table 3.1) values as a function of pH from experimental measurements involving all three nanoparticle sizes and the uncoated silica grains, and from experiments involving the 26 nm nanoparticles and the Fe-coated silica grains. The dashed lines represent K values for various nanoparticle distributions between suspension and adhesion..... 61

Figure 4.1 Measured [TOC] (ppm C) as a function of the initial *B. subtilis* (diamonds) or *S. oneidensis* (squares) concentration at 0.01 M (black), 0.1 M (gray), or 0.3 M (white) NaClO₄. The dashed lines separate the field for the *B. subtilis* data (top) from the field for the *S. oneidensis* data (bottom). 70

Figure 4.2 FTIR spectra of a) <i>B. subtilis</i> and b) <i>S. oneidensis</i> 100 g/L exudate solutions. The black line is pure NaClO ₄ and the exudates made in 0.01 M, 0.1 M, and 0.3 M NaClO ₄ are represented by the gray, black dashed, and gray dashed lines, respectively.	71
Figure 4.3 Representative examples of forward (black squares) and reverse (white triangles) potentiometric titration data from exudate solutions made using 100 g/L <i>B. subtilis</i> (normalized per g/L bacteria) and a) 0.01 M, b) 0.1 M, or c) 0.3 M NaClO ₄	73
Figure 4.4 Representative examples of forward (black squares) and reverse (white triangles) potentiometric titration data from exudate solutions made using 100 g/L <i>S. oneidensis</i> (normalized per g/L bacteria) and a) 0.01 M, b) 0.1 M, or c) 0.3 M NaClO ₄	74
Figure 4.5 Representative fit of a 3-site model (gray curve) to the potentiometric titration data (squares) for the exudate solution made using 100 g/L <i>B. subtilis</i> in 0.1 M NaClO ₄ . Some titration data points have been removed for visualization purposes.	80
Figure 4.6 Comparison of the calculated pK _{a(i)} values for a) <i>B. subtilis</i> and b) <i>S. oneidensis</i> exudate solutions made using 40, 80, and 100 g/L bacterial concentrations and 0.01 (black), 0.1 (gray), or 0.3 (white) M NaClO ₄	82
Figure 4.7 Comparison of the calculated site concentrations (moles of site per g bacteria) for <i>B. subtilis</i> exudates at a) site 1, b) site 2, c) site 3, and d) total sites from solutions with 40, 80, and 100 g/L initial bacterial concentrations and 0.01 M (black), 0.1 M (gray), or 0.3 M (white) NaClO ₄	82
Figure 4.8 Comparison of the calculated site concentrations (moles of site per g bacteria) for <i>S. oneidensis</i> exudates at a) site 1, b) site 2, c) site 3, and d) total sites from solutions with 40, 80, and 100 g/L initial bacterial concentrations and 0.01 M (black), 0.1 M (gray), or 0.3 M (white) NaClO ₄	84

TABLES

Table 2.1 M_w values of NOM.....	23
Table 3.1 Isotherm fit parameters	58
Table 4.1 Total buffering capacity (mol/g) of bacterial exudates and bacterial cells, calculated for the pH range of 3 to 9.....	77
Table 4.2 Calculated $pK_{a(i)}$ values and site concentrations (mol/g) from the 3-site model using forward and reverse data from potentiometric titrations on exudate solutions made with 100 g/L <i>B. subtilis</i> in 0.1 M NaClO ₄	81
Table 4.3 Calculated $pK_{a(i)}$ values and site concentrations (mol/g) averaged for all initial bacterial concentrations and ionic strengths for <i>B. subtilis</i> exudates, <i>S. oneidensis</i> exudates, and the two types of exudates combined.	89

ACKNOWLEDGMENTS

To Jeremy Fein and Patricia Maurice who advised me during my time at Notre Dame, thank you for your support and guidance. I am fortunate to have had not one, but two, advisors who shared their knowledge and experience with me and who have been instrumental in my academic and professional development. Thank you both for your time over the years. Without you, this work never would have been possible.

I would like to thank my committee members, Dr. Chongzheng Na and Dr. Joshua Shrout, as well as the members of my research proposal committee, Dr. Peter Burns and Dr. Clive Neal, for their time and their feedback.

Without the assistance of Jennifer Szymanowski, I would still be working on my last project—thank you for all of your help in the lab over the years. For the analytical instruments and the training and technical support necessary to use them, thanks also go to the Center for Environmental Science and Technology and its staff: Dennis Birdsell, Jon Loftus, and Suzyanne Guzicki.

I am also grateful to those who have assisted in my projects over the years. Dr. Steve Silliman provided the sand used in the first project, as well as valuable discussion, and Dr. Marya Lieberman and Bo Gao in the Department of Chemistry and Biochemistry performed XPS analysis on the sand. Summer REU students Mike Wells and Amy Thomas assisted with data collection for the column experiments. Without our collaborations with Dr. Pratim Biswas at Washington University in St. Louis and his

students, Dr. Jingkun Jiang and Manoranjan Sahu, the second project would not have been possible. In addition, Dr. Elizabeth Haack has been kind enough to help with the interpretation of the FTIR data from the third project.

To the current and former members of my research groups, especially Paul Schramm, Dr. Janice Kenney, Sarrah Dunham-Cheatham, Ling Sheng, and Tom Duster, thank you for your feedback, your assistance in the lab, and your friendship.

Funding for this research was provided by an NSF-Environmental Molecular Science Institute grant to the University of Notre Dame (EAR02-21966).

Finally, I would like to thank my friends and family, who have supported me and believed in me all these years. My parents have given me so much, for which I will always be thankful. I am also especially grateful to my fiancé Casey Dietrich for his encouragement, love, and understanding and for helping me to survive graduate school.

CHAPTER 1: INTRODUCTION

1.1. Overview

As the availability of clean freshwater becomes more limited, it is becoming increasingly important to develop an understanding of the transport of mass—natural and man-made, harmful and innocuous—in water-rock systems of environmental interest. Heavy metals and manufactured nanoparticles are contaminants of particular interest due to their known or potential effects on human health, and the presence of natural components of an aqueous system, such as natural organic matter (NOM), (nano)particulate metal-oxide coatings, or bacteria and their exudates, have the potential to influence the mobility of a variety of contaminants because they are ubiquitous and may participate in a range of adsorption, dissolution, and redox reactions. There are a number of factors that affect the transport of dissolved mass and suspended nanoparticles through the environment, including ionic strength, pH, and interactions with mineral surfaces and/or bacteria and bacterial exudates. The research described here examines several questions related to the adsorption and adhesion of NOM, Cd(II), and nanoparticles onto geosorbents, as well as the potential reactivity of bacterial exudates in environmental systems.

1.2. Background

1.2.1. Mobility of Natural Organic Matter and Cadmium

Natural organic matter (NOM) is ubiquitous in aqueous environmental systems and is composed of a complex mixture of organic molecules with a range of molecular weights, aromaticities, and functional groups (Aiken et al., 1985). Two important components of NOM are the humic acid (HA) and fulvic acid (FA) fractions. Whereas fulvic acid is soluble at all pH values, humic acid is insoluble in water below pH 2. The FA fraction also tends to be lower in molecular weight (MW), lighter in color, and less aromatic than the HA fraction (Aiken et al., 1985). Different NOM fractions may have different reactivities with respect to processes such as sorption, bioavailability, and mobility. For example, higher MW components tend to be more hydrophobic and less mobile than lower MW components and to bind metals and other contaminants to a greater extent (Cabaniss et al., 2000 and references therein).

Reactive surfaces in nature often either consist of, or are coated with, (nano)particulate Fe oxides, Al oxides, and/or clays (Nugent et al., 1998; Brown and Parks, 2001; Penn et al., 2001; Hochella et al., 2008; Theng and Yuan, 2008), which can alter surface properties and affect NOM and metal fate and transport. For example, NOM components of intermediate to high MW have been shown to adsorb preferentially onto Al oxide, Fe oxide, and clay mineral surfaces over the lower MW components, resulting in 'adsorptive fractionation' (e.g. Tipping, 1981; McKnight et al., 1992; Meier et al., 1999; Namjesnik-Dejanovic et al., 2000; Zhou et al., 2001; Hur and Schlautman, 2003; Pullin et al., 2004). NOM adsorption also varies with solution conditions such as pH,

ionic strength, and metal ion concentration (e.g., Tipping, 1981; Stumm, 1992; Vermeer et al., 1998; Namjesnik-Dejanovic et al., 2000; Weng et al., 2006).

The large body of literature on NOM adsorption to Fe and Al oxides and clays, as well as the common occurrence of (nano)particulate coatings on aquifer sands, together suggest that NOM mobility should be retarded in many sandy aquifers by the porous media. Given that NOM and metals may affect one another's adsorption, this NOM retention could also have an important effect on metal fate and transport. The experiments described in Chapter 2 were designed to expand our understanding of NOM adsorption and mobility in porous media through:

- (1) flow-through column experiments, which more closely mimic subsurface transport than is possible with batch experiments, using primarily quartz sands naturally coated with Al- and Fe-rich nanoparticles, along with hematite and corundum sands;
- (2) the use of an NOM reverse osmosis isolate that contains both humic and fulvic acid. Although NOM mobility has been investigated previously using column experiments (e.g., Dunnivant et al., 1992; Gu et al., 1996; Münch et al., 2002; Guo and Chorover, 2003; Chi and Amy, 2004; Wei et al., 2010), this study used an unfractionated NOM source that has been used in a previous batch adsorption study (Pullin et al., 2004);
- (3) the analysis of column influent and effluent by high pressure size exclusion chromatography and UV/vis spectroscopy to characterize changes in NOM MW distributions and light absorbance properties upon passing through the porous media;
- (4) a focus on both pH (5-8) and ionic strength (0.001-0.1 M) effects on adsorption to an extent that has not been performed previously. Many studies have shown that NOM adsorption tends to increase with decreasing pH to pH ~ 4; however, ionic strength effects on adsorption are less well understood. HA adsorption to Fe and Al oxides is strongly dependent on and increases with increasing ionic strength (Schlautman and Morgan, 1994; Wershaw et al., 1996; Vermeer et al., 1998; Au et al., 1999; Saito et al., 2004; Weng et al., 2006), whereas studies of ionic strength effects on FA adsorption have produced mixed results (Schlautman and Morgan, 1994; Filius et al., 2000; Weng et al., 2006);

(5) an examination of how NOM and the heavy metal contaminant cadmium, Cd(II), may influence one another's adsorption and mobility through the porous media. Cd(II) is a metal of interest due to its toxicity and presence at both natural and contaminated sites, and previous research has indicated the possibility of mutual effects on the adsorption of these components (Frimmel and Huber, 1996; Vermeer et al., 1998; Collins et al., 1999; Vermeer et al., 1999).

With the use of flow-through columns, unfractionated NOM, and sands with natural (nano)particulate grain coatings, these experiments will more closely replicate the interactions occurring in a complex groundwater system, and the results will make it possible to better understand the processes affecting the mobility of Cd and NOM in such an environment.

1.2.2. TiO₂ Nanoparticle Adhesion to Geosorbents

The use of engineered nanoparticles has expanded rapidly in recent years such that many consumer products now contain nanoparticles (Wiesner et al., 2006), especially titanium dioxide (TiO₂) nanoparticles. As a result, TiO₂ nanoparticles are known to be entering the environment both intentionally (e.g., Mattigod et al., 2005; Pena et al., 2005; Theron et al., 2008; Oyama et al., 2009) and unintentionally (Kaegi et al., 2008). Once in the environment, there may be many undesired consequences, such as the inhibition of the growth of natural bacterial populations (Adams et al., 2006). Exposure to nano-sized TiO₂ particles also has the potential to be toxic to other larger organisms, including humans (Long et al., 2006; Nel et al., 2006; Wiesner et al., 2006; Limbach et al., 2007; Wang et al., 2007; Simon-Deckers et al., 2008; Brunet et al., 2009). However, despite their widespread use and potential for environmental release, the controls on the fate and mobility of TiO₂ nanoparticles in the subsurface are poorly understood.

Both aggregation and surface adhesion can affect the mobility of engineered nanoparticles in geologic systems, and many previous studies have focused on aggregation processes. TiO₂ nanoparticle aggregates are prevalent under a wide range of aqueous conditions and form from nanoparticles of many primary sizes (Lecoanet et al., 2004; Dunphy Guzman et al., 2006; Ridley et al., 2006; Choy et al., 2008; Domingos et al., 2009; Jiang et al., 2009; Fatisson et al., 2009; French et al., 2009). Nanoparticle aggregation behavior can also affect or be affected by interactions with geosorbents, such that TiO₂ nanoparticles remain disaggregated and mobile in certain soils and under certain aqueous conditions but aggregate and become immobile due to straining and/or adhesion in others (Dunphy Guzman et al., 2006; Choy et al., 2008; Fang et al., 2009; Fatisson et al., 2009; Joo et al., 2009), which significantly influences particle transport.

There have been few studies to examine the adhesion behavior of TiO₂ nanoparticles onto well-characterized, uniform geosorbents, so quantitative models of nanoparticle transport behavior in geologic systems are poorly constrained. The study described in Chapter 3 was designed to:

- (1) characterize the influence of pH (3-8), nanoparticle size (16-50 nm), and nanoparticle concentration (10-200 mg/L) on the adhesion of TiO₂ nanoparticles to silica grains. In previous transport studies (Dunphy Guzman et al., 2006; Choy et al., 2008; Fang et al., 2009; Joo et al., 2009), it has been difficult to differentiate between nanoparticle adhesion and straining of large nanoparticle aggregates in order to understand the relative effects of electrostatic controls versus aggregation controls on TiO₂ transport;
- (2) use a single nanoparticle size fraction (26 nm) to conduct adhesion experiments with Fe(III) oxide-coated silica grains in order to determine the effect of geosorbent mineral surface composition on particle adhesion behavior.

These experiments are some of the first to study the adhesion of TiO₂ nanoparticles onto geosorbents, and the results will provide information on factors with

the potential to influence TiO₂ nanoparticle adhesion, and thus mobility, in environmental systems.

1.2.3. Proton Binding of Bacterial Exudates

Bacteria play an important role in many environmental processes including adsorption and/or reduction of metals, which can influence metal transport (e.g., Beveridge and Murray, 1976; Lovely, 1993; Brown and Parks, 2001; Newman and Banfield, 2002; Borch et al., 2010); precipitation or dissolution of various minerals (e.g., Fortin and Beveridge, 1997; Bennett et al., 2001); and the degradation of natural organic matter and certain anthropogenic contaminants, which can be used in remediation strategies (e.g., Young et al., 2005; Mroziak and Piotrowska-Seget, 2010; Tiquia, 2010). Most of these processes involve the bacterial cell wall and/or bacterial metabolism directly. However, bacteria also exude a wide range of organic molecules through active metabolic processes, as well as lysis and decay. These bacterial exudates are dissolved organic molecules exuded from whole cells and are different from the non-aqueous extracellular polymeric substances often produced by bacteria as an important component of biofilms. There is now growing evidence that these exudates can contribute to important geochemical processes. For example, metal reduction can occur in the presence of bacterial exudates (Ohnuki et al., 2007; Kenney et al., 2010), and bacterial exudates have been shown to accelerate mineral dissolution (Lee and Fein, 2000; Perry et al., 2003; Perry et al., 2005; Pokrovsky et al., 2009). The observed effects of the bacterial exudates suggest that they contain proton-active organic acid functional groups as these are the most likely means of interacting with metals and mineral surfaces.

Despite the indications that bacterial exudates can affect geochemical processes, there has been virtually no work conducted to quantify their environmental concentrations or characteristics. The research described in Chapter 4 was designed to:

- (1) use potentiometric titrations to determine the extent of proton binding exhibited by bacterial exudates made using a Gram-positive (*Bacillus subtilis*) and a Gram-negative (*Shewanella oneidensis*) bacterial species with a range of initial bacterial concentrations (40-100 g/L bacteria) and in solutions with a range of ionic strengths (0.01-0.3 M);
- (2) calculate the acidity constants and the concentrations of proton binding sites found in the exudates using chemical equilibrium modeling;
- (3) compare the calculated values for exudates produced from the two bacterial species and at different bacterial concentrations and ionic strengths in order to better understand how differences in cell wall characteristics may influence the properties of bacterial exudates and how changing solution chemistry may affect the production of bacterial exudates;
- (4) compare the proton binding behavior of bacterial exudates with that determined previously for bacterial cells (Borrok et al., 2005; Fein et al., 2005; Mishra et al., 2010);
- (5) use FTIR spectrometry to provide an initial qualitative description of the exudates from the two bacterial species.

The proton binding properties determined for the bacterial exudates in this study are important as they are among the first of their kind and will provide a framework for understanding the interactions of bacterial exudates with other components in geologic and engineered systems.

CHAPTER 2:
MOBILITY OF CD(II) AND NATURAL ORGANIC MATTER THROUGH
NATURALLY NANOPARTICLE-COATED SANDS

2.1. Introduction

Natural organic matter (NOM) is a complex mixture of organic molecules with a range of molecular weights and aromaticities, as well as functional group concentrations and distributions (Aiken et al., 1985). Lower molecular weight (MW) components tend to be more hydrophilic, more mobile, and more bioavailable whereas higher MW components tend to be more hydrophobic and less mobile and to bind metals and other contaminants to a greater extent (Cabaniss et al., 2000). NOM components of intermediate to high MW tend to adsorb preferentially onto Al oxide, Fe oxide, and clay mineral surfaces relative to adsorption of lower MW components; the resulting ‘adsorptive fractionation’ alters the characteristics, and hence reactivity, of the mobile NOM in porous media (e.g., Tipping, 1981; McKnight et al., 1992; Zhou et al., 2001; Hur and Schlautman, 2003).

Pure quartz has a low point of zero charge, generally ~ 2 (Brantley and Chen, 1995), and clean quartz sands therefore tend to be negatively charged over a wide pH range and to adsorb NOM only weakly or not at all (Weigand and Totsche, 1998; Wei et al., 2010). However, many sand grains in nature are coated with (nano)particulate Fe oxides, Al oxides, and/or clays (Nugent et al., 1998; Brown and Parks, 2001; Penn et al.,

2001; Hochella et al., 2008; Theng and Yuan, 2008). Previous studies have shown that NOM adsorption to Fe and Al oxides and clays can be quite strong and may involve a variety of different mechanisms, including: electrostatic interactions between negatively charged NOM and metal-oxide surfaces, which are positively charged below their pH_{pzc} ; ligand exchange; the so-called hydrophobic effect, in which non-polar components are attracted to other non-polar sites either on the surface or on other adsorbed molecules; and/or van der Waals interactions (e.g., Tipping, 1981; Stumm, 1992; Wershaw et al., 1996; Kaiser and Zech, 1999; Hur and Schlautman, 2003). NOM sorption may involve formation of surface-associated organic matter aggregates (Wershaw et al., 1996; Namjesnik-Dejanovic and Maurice, 2000), and NOM may form mixed mineral-organic aggregates with oxide and clay nanoparticles in soils (Chorover et al., 2007). Adsorption has been shown to vary with the detailed nature of the NOM and the mineral sorbent and with solution conditions such as pH, ionic strength, and metal ion concentrations (e.g., Tipping, 1981; McKnight et al., 1992; Stumm, 1992; Vermeer et al., 1998; Kaiser and Zech, 1999; Namjesnik-Dejanovic et al., 2000; Weng et al., 2006). Synthetic Fe-oxide-coated quartz sand has been shown to substantially retard NOM mobility in column experiments (Chi and Amy, 2004). The large body of literature on NOM adsorption to Fe and Al oxides and clays and the common occurrence of (nano)particle coatings on aquifer sands together suggest that NOM mobility should be retarded in many sandy aquifers by the porous media. Given that NOM and metals may affect one another's adsorption (Frimmel and Huber, 1996; Vermeer et al., 1998; Collins et al., 1999; Vermeer et al., 1999), this NOM retention could also have an important effect on metal fate and transport.

The column experiments described herein were designed to expand our understanding of NOM mobility in porous media over a range of pH (5-8) and ionic strength (0.001-0.1 M) conditions using quartz sands naturally coated with Al- and Fe-rich nanoparticles. Column influent and effluent were monitored for changes in NOM MW distributions and light absorbance properties. This study also investigated the effects of NOM on Cd(II) mobility and of Cd(II) on NOM sorptive fractionation.

2.2. Materials and Methods

2.2.1. Natural Organic Matter and Geosorbents

NOM was concentrated on-site from surface water (June 6, 2002) at Nelson's Creek, a first-order stream in the Ottawa National Forest (MI, USA), using a portable RealSoft PROS/IS reverse osmosis (RO) system (Serkiz and Perdue, 1990; Sun et al., 1995). Concentration of NOM by RO, followed by freeze-drying, allowed for long-term sample storage (in a desiccator) and for use in a wide range of experiments and analyses (Pullin et al., 2004). The physicochemical properties of the RO concentrate (diluted) and of raw filtered water collected simultaneously at Nelson's Creek are compared by Pullin et al. (2004).

Three sands were used in the column experiments: commercially available hematite (Virginia Materials-Blasting Abrasives, Norfolk, VA) and corundum (Smurfit-Stone Specialty Packaging Division, New Philadelphia, OH) sands and a naturally coated quartz sand (coating most likely Fe and Al oxides; see below). The naturally coated sand (hereafter referred to as the Oyster sand) was collected from the U.S. Department of

Energy research site in Oyster, Virginia (by S.E. Silliman, Univ. Notre Dame) and described previously (Dong et al., 2002). The hematite and Oyster sands were dry sieved with 20-40 mesh sieves (0.842-0.420 mm), and the more fine-grained corundum was sieved with a 40 mesh sieve (< 0.420 mm). All sands were rinsed repeatedly with distilled, deionized water (DDI) and dried overnight at 55°C.

2.2.2. Geosorbent Characterization

BET surface area analysis was conducted on all three sands using a model SA3100 volumetric sorption analyzer (Coulter Instruments). X-ray diffraction (XRD) was performed on an Oyster sand sample prepared by grinding the sand in ethanol with a mortar and pestle. XRD analysis with a 2θ value from 5 to 60 degrees, in time steps of 0.050 degrees (step time 1 second) was performed on a Bruker D8 Discovery Powder Diffractometer with a Sol-X solid-state detector. A Kratos XSAM 800 X-ray photoelectron spectrometer (XPS) using a Mg $K\alpha$ X-ray source with an energy of Mg X-rays = 1253.6 eV was used to analyze ground and whole Oyster sand samples to determine the composition of the sand in ‘bulk’ (ground sample) and at the surface (whole sample). The samples were mounted on sample stubs with conductive carbon tape, and data were analyzed using Kratos Vision 2 software.

2.2.3. Sample Solutions and Columns

NOM transport behavior was measured as a function of pH (pH 5, 8 in hematite and corundum sands; pH 5, 6, 7, 8 in Oyster sand) and ionic strength (0.001 M, 0.01 M, 0.1 M NaClO₄). NOM sample solutions were made from a stock solution prepared using

dried Nelson's Creek RO isolate and deionized (MilliQ) water. After rehydration, the concentrated NOM solution was filtered using a 0.22 μm filter, and the dissolved organic carbon concentration ([DOC]) was measured (Shimadzu TOC-5000). A portion of this stock solution was combined with NaClO_4 electrolyte solutions to make the appropriate NOM solutions. Experiments were also conducted at 0.01 M NaClO_4 with Cd alone (pH 5, 8) and with NOM (5 or 20 ppm C) plus Cd (pH 5, 6, 7, 8). Cd solutions (2.5 ppm) were made using 1000 ppm Cd ICP stock in 2% HCl (Fisher Scientific; Pittsburgh, PA). Column experiments also used the non-adsorbing conservative tracer sulforhodamine B (Sigma-Aldrich; St. Louis, MO) at the three ionic strengths and pH 5 and 8. pH was adjusted using 0.01, 0.1, or 1.0 M HCl or NaOH.

Columns had a borosilicate glass barrel 10 cm long and 1.0 cm in diameter (Kimble-Kontes; Vineland, NJ) and were packed by adding background electrolyte solution followed by one of the sands while tapping gently to remove air bubbles. A gravity feed system with flow from bottom to top was used to pass the solutions through the stationary sand grains. 20-25 mL of background electrolyte were allowed to flow through the column prior to introducing the experimental solution. All experiments were continuous-flow column experiments. The flow rate for all experiments was ~ 2 mL/min, which was controlled by adjusting the influent tubing pressure. Column experiments were conducted in at least duplicate or until reproducible data were obtained. Prior to each use, columns were rinsed ten times with DDI water, five times with acetone, and dried at 60°C .

2.2.4. UV/vis Analysis

An in-line (Hewlett Packard 8453) UV/vis spectrophotometer monitored absorbance ($\lambda = 200\text{-}600$ nm) of column effluent. Three key wavelengths included: 254 nm, which tends to detect a broad range of NOM molecules; 280 nm, which is often associated with the benzene rings representative of the more aromatic higher MW components; and 350 nm, which is strongly correlated with lignin phenols (Traina et al., 1990; Zhou et al., 2000; Hernes and Benner, 2003). NOM breakthrough curves were determined using absorbance at 254 nm. Molar absorptivity is typically calculated as absorbance at a specific wavelength normalized to [DOC]. Because it was not possible to measure [DOC] of the effluent simultaneously with in-line absorbance, absorbance at 254 nm was used as a proxy for [DOC] with the understanding that some NOM components may not be detected at this wavelength (e.g., Namjesnik-Dejanovic et al., 2000; Pullin et al., 2004). Thus, absorbance ratios at 280 nm/254 nm and 350 nm/254 nm were used as molar absorptivity surrogates. Absorbance at 565 nm was used to determine the breakthrough of the sulforhodamine B tracer solutions.

Absorbance of influent solutions ($\lambda = 200$ to 600 nm) were measured using a Varian Cary 3 spectrophotometer with 1.0 cm quartz cells. All breakthrough curves were normalized to the absorbance of the starting solution (at 254 nm for the NOM solutions or 565 nm for the tracer solutions) and plotted as a function of dimensionless pore volumes. The normalized breakthrough curves were then compared for various experimental conditions. Retention of the NOM in the columns will be discussed in terms of overall retention at a given pore volume (i.e., $y = 0$ indicates complete retention and $y = 1$ indicates no retention). 50% retention ($\text{abs}/\text{abs}_0 = 0.5$) will also be compared.

2.2.5. ICP-OES and HPSEC Measurements

Samples (5 mL and 1.5 mL) of column influent and effluent (after passing through the in-line spectrophotometer) were collected for analysis by Inductively Coupled Plasma-Optical Emission Spectrometry (ICP-OES) or High Pressure Size Exclusion Chromatography (HPSEC). ICP-OES (Perkin Elmer Optima 2000 DV) was used to measure metal concentrations (Cd, Fe, Al, Si) in influent and effluent solutions. All solutions were acidified prior to analysis, and Y was used as an internal standard. HPSEC was conducted to determine NOM MW distributions (Chin et al., 1994; Zhou et al., 2000) in effluent NOM samples at four times during each column experiment, as well as in a sample of the influent NOM solution prior to its introduction into the column. HPSEC samples were analyzed in triplicate with a Waters 2695 HPLC system, Waters Protein Pak 125 modified silica column, and 0.01 M NaCl mobile phase. UV/vis detection (Waters 2996 photodiode array) at 254 nm was used. Retention time on the HPSEC column was calibrated to log MW using standards ranging from 58 to 15,200 daltons (Da): acetone (Aldrich, 58 Da), salicylate (Aldrich, 138 Da), and four polystyrene sulfonate (PSS) polymers from Polysciences, Inc. (1,430 Da; 4,950 Da; 6,530 Da; 15,200 Da) (Zhou et al., 2000).

MW of NOM retained in the columns at each time period was calculated as:

$$\text{influent log MW} - \text{effluent log MW at } t_i = \text{retained log MW at } t_i \quad (2.1)$$

where t_i was one of the four sampling intervals. The MW distribution of the influent solution was then compared with the distributions of the NOM retained in the column at each sampling period. To better understand the MW distribution of adsorbed NOM in the presence of exchange that may be occurring over time, the sum or ‘total’ effluent and

adsorbed MW distributions were calculated (separately) by summing the distributions at each of the four sampling intervals. The weight average MW (M_w), which is the weight of the molecule to which the average atom belongs, was calculated as by Cabaniss et al., (2000) and Zhou et al. (2000).

2.3. Results and Discussion

2.3.1. Characteristics of the Geosorbents

BET specific surface areas are 0.361, 0.025, and 0.017 m²/g for the Oyster, hematite, and corundum sands, respectively. XRD analysis of the Oyster sand revealed predominantly quartz with minor amounts of feldspar and possibly some clay. XPS analysis of the Oyster sand showed that the ground (representing ‘bulk’) sample composition was Si (66%), Al (9.5%), and Fe (3%); the surfaces of the grains (measured on whole samples) were enriched in Al (32%) and Fe (7%) relative to Si (26%). Penn et al. (2001) analyzed sands from approximately the same locality as the Oyster sand by high resolution TEM and reported that they were “predominantly a mixture of Si- and Al-rich nanophases of variable crystallinity, with interspersed smectite and agglomerates of goethite nanoparticles.” The XPS results were thus consistent with this previously reported (nano)particulate coating.

2.3.2. Ionic Strength and pH Effects

NOM breakthrough curves are presented in the absence of Cd(II) as a function of ionic strength and pH (Figure 2.1 and Figure 2.2). At one pore volume, retention of the

conservative tracer was at about 50%, which is expected for a non-reactive solute experiencing only molecular diffusion and mechanical dispersion (Freeze and Cherry, 1979). NOM solutions all showed much greater retention than the tracer (50% retention not reached until ≥ 2 pore volumes), and at all ionic strengths, NOM retention was greatest at pH 5-6 and less at pH 7-8 (e.g., Figure 2.2: at 0.001 M, 50% retention at 2.8 and 2.6 pore volumes for pH 5 and 6, respectively, and at 2.0 pore volumes for both pH 7 and 8). Overall retention increased with increasing ionic strength (Figure 2.1: 50% retention at pH 5: 2.8, 5.8, and 7.6 pore volumes at 0.001, 0.01, and 0.1 M, respectively) and decreased with increasing pH (Figure 2.1: 50% retention at pH 8: 2.0, 4.3, and 6.5 pore volumes at 0.001, 0.01, and 0.1 M, respectively). For comparison, breakthrough curves made using 280 and 350 nm, which correlate to specific NOM constituents, are shown in Figure A1. Breakthrough curves for the hematite and corundum sands (Figure A2) also show increased NOM retention with increasing ionic strength and decreasing pH. Because the specific surface areas of the pure Fe and Al oxide sands are over an order of magnitude smaller than that of the Oyster sand, it is only possible to compare trends in the data and not absolute differences in retention.

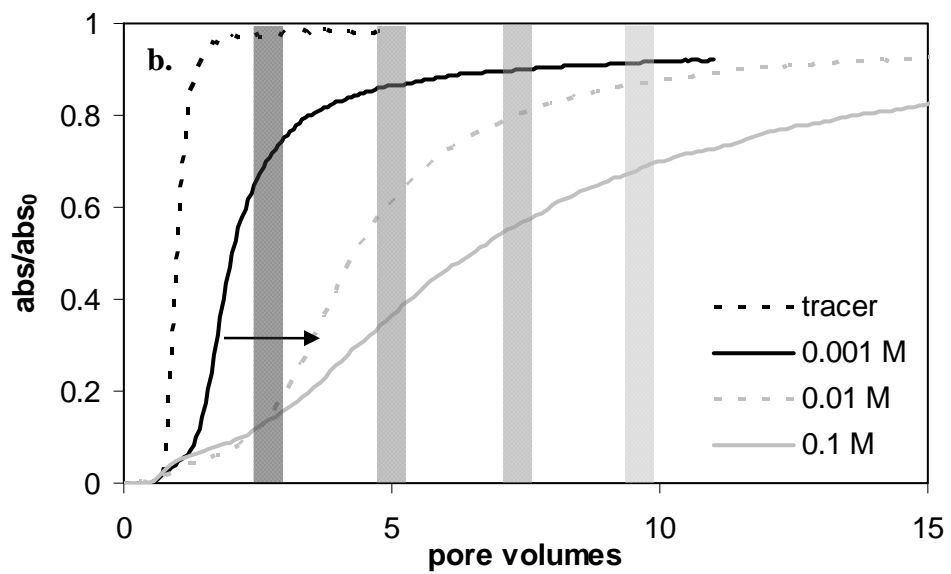
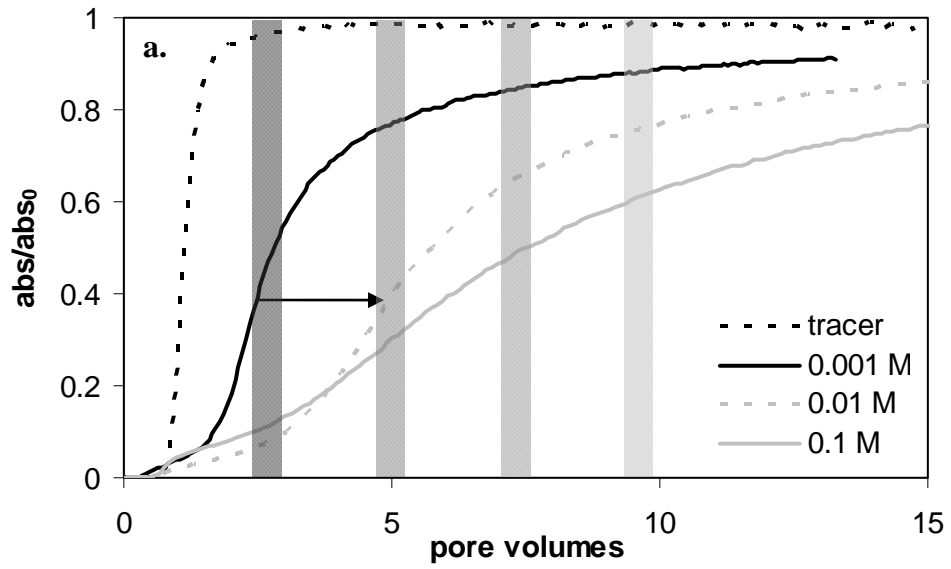


Figure 2.1: NOM retention on Oyster sand increased as a function of ionic strength at a) pH 5 and b) pH 8. Gray bars represent effluent sampling times for HPSEC analysis.

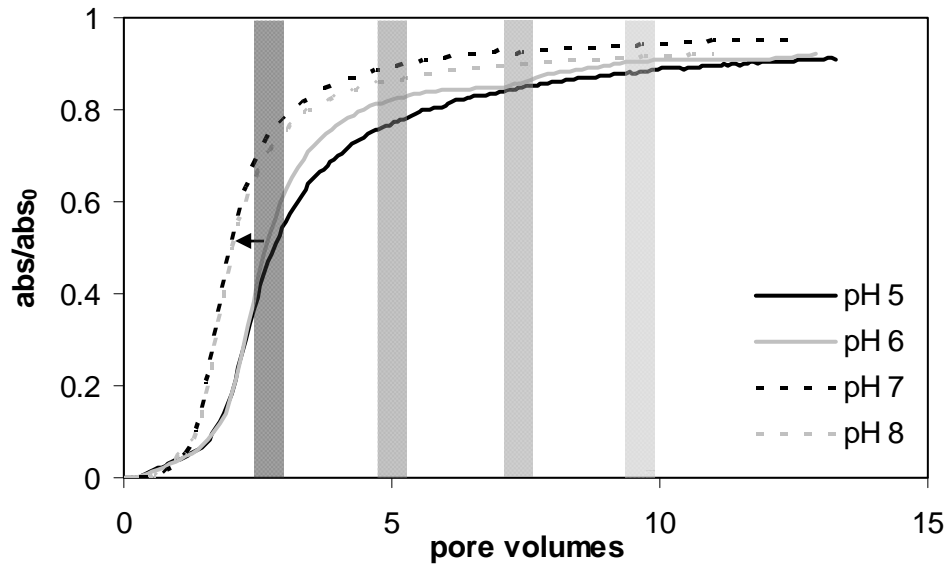


Figure 2.2: NOM retention at 0.001 M as a function of pH. Similar retention was observed at pH 5 and 6 and at pH 7 and 8; overall retention decreased with increasing pH. Gray bars represent effluent sampling times for HPSEC analysis.

NOM retention is attributed to adsorption onto the column sands rather than to degradation and/or straining because: 1) experiments were short in duration, limiting potential for NOM degradation; 2) previous batch and column experiments have shown adsorption of NOM onto mineral surfaces (e.g., Tipping, 1981; Dunnivant et al., 1992; Gu et al., 1996; Meier et al., 1999; Namjesnik-Dejanovic et al., 2000; Zhou et al., 2001; Guo and Chorover, 2003; Chi and Amy, 2004); 3) previous experiments performed in flow-through columns using an uncoated quartz sand and various NOM samples resulted in little retention of NOM (Weigand and Totsche, 1998; Wei et al., 2010); and 4) breakthrough curves presented in this paper for the hematite and Oyster sands are distinctly different. The hematite and Oyster sands have a similar grain size but

substantially different surface areas. If straining is the primary driver of retention, then the breakthrough curves for the Oyster and hematite sands should be similar; however, this is not the case as much less retention is observed when less total surface area is present (e.g., Figure A3).

The decrease in NOM adsorption with increasing pH (Figure 2.2) is likely due to an increase in repulsion between the increasingly negative surface and NOM and a decrease in the protonation of surface sites (e.g., Tipping, 1981; Vermeer et al., 1998). Retention was also enhanced by increasing ionic strength. Humic acid (HA) adsorption to Fe and Al oxides has been shown to increase with increasing ionic strength (Schlautman and Morgan, 1994; Wershaw et al., 1996; Vermeer et al., 1998; Au et al., 1999; Saito et al., 2004; Weng et al., 2006), whereas studies of ionic strength effects on fulvic acid (FA) adsorption have produced mixed results (Schlautman and Morgan, 1994; Filius et al., 2000; Weng et al., 2006). It is likely that a combination of surface charge, charge screening, and conformation effects governs NOM adsorption under changing ionic strength conditions (e.g., Wershaw et al., 1996; Vermeer et al., 1998; Au et al., 1999; Münch et al., 2002).

In all cases, the initial 280 nm/254 nm ratio in the column effluent was less than in the influent (~0.7 and 0.8, respectively), indicating preferential retention, hence adsorption, of more aromatic components and greater mobility of less aromatic components (Figure A4). Similar trends were observed in the 350 nm/254 nm absorbance ratio (~0.2 to 0.3), indicating preferential adsorption of lignin-derived components (Figure A5). Other investigators have observed a similar decrease in the aromaticity or molar absorptivity at 280 and 350 nm of NOM remaining in solution after

adsorption (e.g., Dunnivant et al., 1992; McKnight et al., 1992; Zhou et al., 2001; Guo and Chorover, 2003; Pullin et al., 2004).

The sampling intervals for the four effluent samples analyzed by HPSEC are highlighted in Figure 2.1. For samples in 0.1 M, peaks broadened substantially and shifted toward lower MW at pH 6-8 (data not shown), suggesting potential breakdown of the NOM in the HPSEC column. Thus, we do not report MW data for samples at 0.1 M. The MW distributions of the influent 0.001 and 0.01 M NOM solutions did not change with pH or ionic strength (Figure A6). The MW distribution of NOM retained in the column at each of the sampling periods is shown in Figure 3. For both the 0.001 (Figure A7) and 0.01 M (Figure 2.3) experiments at pH 6, the MW distribution of the influent NOM matched closely that of the NOM retained in the column at t_1 , consistent with nearly complete initial retention of NOM. This is consistent with results of batch adsorption experiments of NOM on goethite conducted by Zhou et al. (2001), who observed little or no preferential adsorption or ‘sorptive fractionation’ at low sorption densities because of minimal competition between NOM molecules for sorption sites and/or little change to mineral surface charge at low coverages. As the experiments progressed and NOM retention decreased, the peak heights decreased from ~ 0.003 to ≤ 0.0006 . The peaks at t_2 - t_4 shifted right toward higher log MW retained (from log MW 3.2 to 3.3), indicating that as the experiments progressed, the NOM fractions of intermediate to high MW were retained preferentially in the column. Such preferential retention of intermediate to higher MW NOM leading to sorptive fractionation has been observed previously (e.g., Zhou et al., 2001; Namjesnik-Dejanovic et al., 2000; Dunnivant et al., 1992; Gu et al., 1996; Meier et al., 1999; Guo and Chorover, 2003) (see

below). These results also agree with absorbance ratio data suggesting that the more aromatic components, which also tend to be higher in MW, adsorb preferentially. The same effects were observed at pH 8 (Figure A7), but the decrease in retained NOM peak heights (from ~0.003 to ≤ 0.0004) and shift toward higher log MW material retained (from 3.2 to 3.3 or 3.4 for the 0.001 or 0.01 M experiments, respectively) occurred more quickly, along with the overall decrease in retention at this pH. Based on summing of retention data from the four sampling intervals, the MW distributions of the ‘total’ adsorbed NOM were shifted noticeably toward intermediate or higher MW whereas the summed or ‘total’ effluent solutions were skewed more towards lower MW (Figure 2.4).

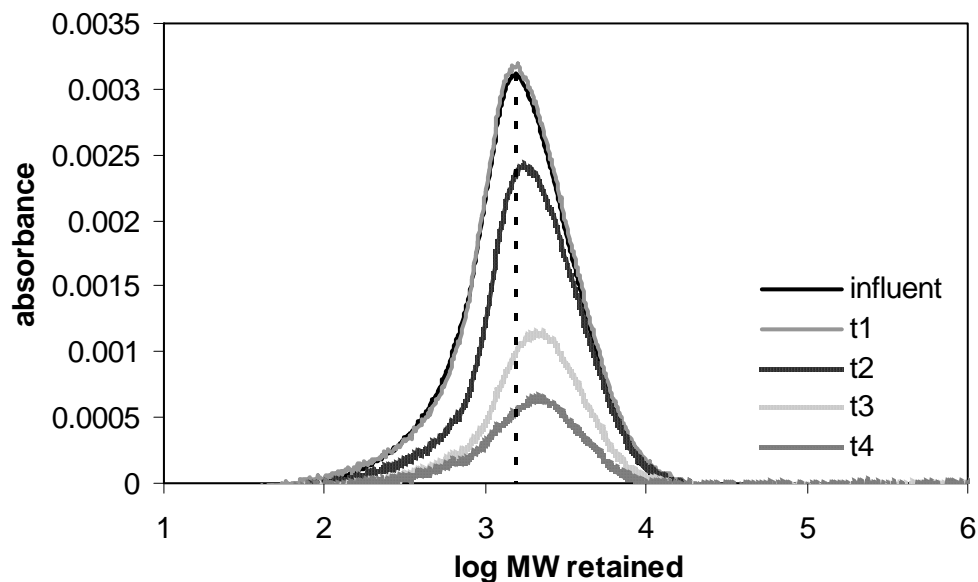


Figure 2.3: MW distributions of NOM retained in the column at each sampling period compared to the influent MW distribution from experiments conducted with 5 ppm C at pH 6 in 0.01 M NaClO₄. Dashed vertical line represents the MW peak of the influent solution.

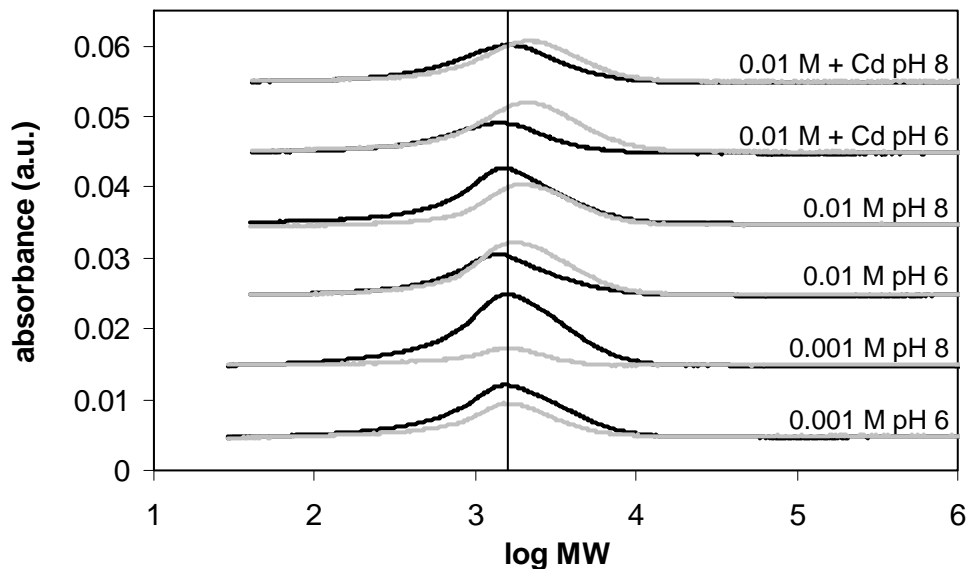


Figure 2.4: MW distributions of the ‘total’ effluent NOM (black lines) and ‘total’ adsorbed NOM (gray lines) of the four HPSEC samples for each of the 5 ppm C experiments at pH 6 or 8 in 0.001 M NaClO₄ and 0.01 M NaClO₄ with or without Cd. The black vertical line represents the peak log MW of the influent solution.

A comparison of the effluent M_w values at different sampling intervals (Table 2.1) also indicated preferential adsorption of high and/or intermediate MW NOM components. The effluent M_w was low at t_1 and gradually increased to nearly the influent M_w by t_4 . This increase occurred more quickly at lower ionic strength. The same general trends were observed at pH 8. In the column experiments presented here, at first essentially all components were retained, although a small proportion of lower MW material was present in the effluent. As the experiments progressed, intermediate and higher MW NOM components were retained preferentially, hence adsorbed, and the

preference for adsorption of higher MW components was more pronounced at lower pH and higher ionic strength (Table 2.1; Figure 2.3, Figure 2.4, Figure A7). Eventually, retention decreased until effluent matched influent.

TABLE 2.1
M_w VALUES OF NOM

pH 6		pH 8	
Sample	M _w	Sample	M _w
0.001 M--5 ppm C			
<i>influent</i>	2030	<i>influent</i>	1970
<i>t</i> ₁	572	<i>t</i> ₁	2090
<i>t</i> ₂	2110	<i>t</i> ₂	2040
<i>t</i> ₃	2010	<i>t</i> ₃	2030
<i>t</i> ₄	2010	<i>t</i> ₄	2050
0.01 M--5 ppm C			
<i>influent</i>	2170	<i>influent</i>	2280
<i>t</i> ₁	411	<i>t</i> ₁	699
<i>t</i> ₂	1240	<i>t</i> ₂	1900
<i>t</i> ₃	1920	<i>t</i> ₃	2120
<i>t</i> ₄	2050	<i>t</i> ₄	2200
0.01 M--5 ppm C + Cd			
<i>influent</i>	2250	<i>influent</i>	2290
<i>t</i> ₁	509	<i>t</i> ₁	522
<i>t</i> ₂	1020	<i>t</i> ₂	1640
<i>t</i> ₃	1610	<i>t</i> ₃	1980
<i>t</i> ₄	1880	<i>t</i> ₄	2070

NOTE: M_w values (in Daltons) of influent and effluent NOM at *t*₁₋₄ from column experiments with 5 ppm C in 0.001 M NaClO₄ and 0.01 M NaClO₄ with or without Cd.

Pullin et al. (2004) performed batch adsorption experiments on goethite using the same RO sample as used here. They found that overall adsorption decreased from pH 3.5 to 5.5, which was due mostly to lesser adsorption of higher MW components as pH increased. Zhou et al. (2001) investigated FA adsorption to goethite at pH 3.5, 5.5, and 7.5. They found that at all three pH values, the intermediate MW fraction (1,251-3,750 Da) dominated adsorption. They also observed that the importance of larger DOM components to overall adsorption decreased from pH 3.5 to pH 5.5 and 7.5. Decreases in adsorption of the highest MW components as pH increases in both batch and column experiments could be due to increased electrostatic repulsion between these highly charged molecules and nearby adsorbed molecules. Such repulsion would likely decrease at higher ionic strength due to charge screening and/or collapse of the double layer. In contrast, at low pH, protonation would lead to more neutral molecules, and hence to stabilization via hydrophobic interactions. In column experiments with synthetic Fe-oxide-coated quartz sand, Chi and Amy (2004) observed preferential adsorption of higher MW components of Suwannee River FA but preferential adsorption of lower MW components of Suwannee River HA at pH ~ 6-7; these differences were thought to be related to differences in hydrophobicity and functional group density associated with the two different NOM fractions.

2.3.3. Cadmium

Cd retention, hence adsorption, increased with increasing pH (Figure 2.5). The presence of NOM only slightly increased Cd adsorption at pH 5 but increased adsorption at pH 8 more substantially, with Cd adsorption increasing to a greater extent in 5 ppm C

(Figure 2.5) than 20 ppm C (Figure A8). NOM has been shown to increase Cd adsorption onto various mineral phases in batch experiments at pH 8-9 (Frimmel and Huber, 1996; Collins et al., 1999; Vermeer et al., 1999). While it is possible that Cd forms a ternary surface complex with NOM at pH 8, spectroscopic evidence is lacking.

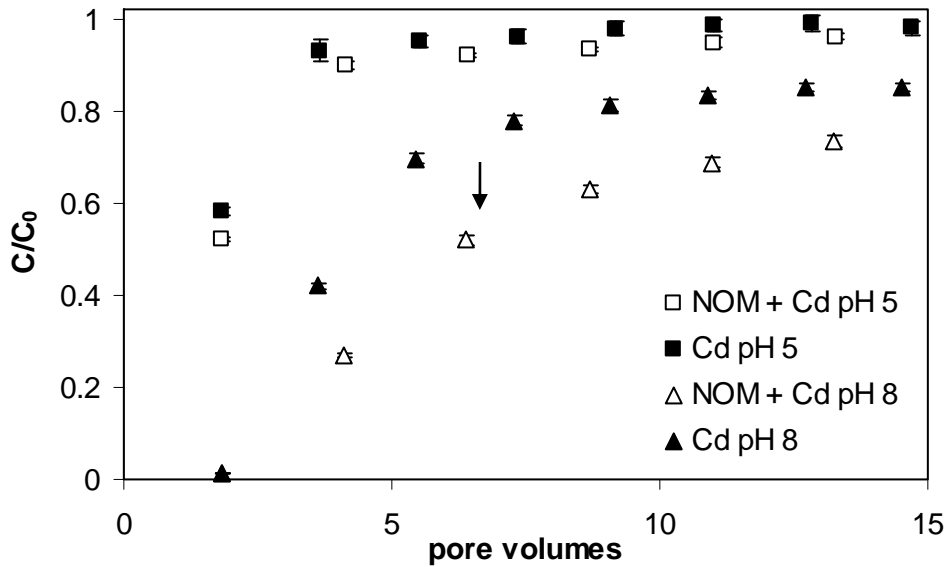


Figure 2.5: 5 ppm C NOM increased Cd adsorption onto Oyster sand in 0.01 M NaClO₄ at pH 8 but only slightly at pH 5.

NOM breakthrough curves for the 5 ppm C, 0.01 M solutions with and without Cd (Figure 2.6) showed that NOM retention at pH 5 was essentially the same regardless of whether or not Cd was present (50% retention at 5.8 pore volumes without Cd and 5.9 pore volumes with Cd); however, at pH 8 slightly more organic matter was retained in the absence of Cd (50% retention at 4.3 pore volumes without Cd and 3.9 pore volumes with

Cd). This (slight) decrease in NOM adsorption in the presence of Cd is the opposite of what Vermeer et al. (1998) observed at pH 9 in batch experiments using HA and hematite and an order of magnitude higher Cd concentration.

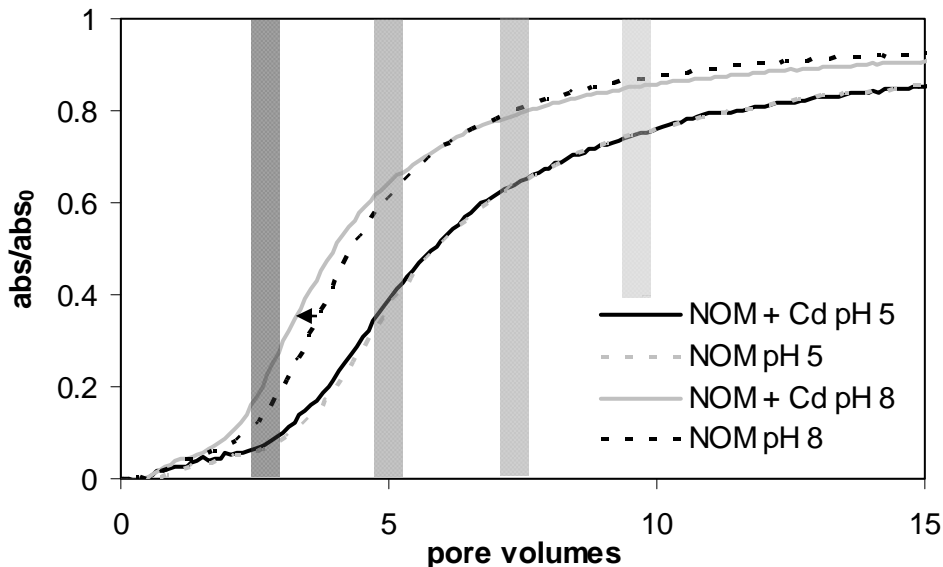


Figure 2.6: Cd slightly decreased NOM adsorption onto Oyster sand in 0.01 M NaClO₄ at pH 8 but not 5. Gray bars represent effluent sampling times for HPSEC analysis.

The slight decrease in NOM adsorption in the presence of Cd at pH 8 could indicate competition between Cd in solution and the mineral surface for complexation or binding of NOM. Aqueous Cd-NOM complexes could be forming which have a lesser affinity for the mineral surface than does the NOM alone, or Cd could be inducing some

change in the conformation of the NOM (in solution and/or on the mineral surface) such that the sorption of NOM decreases.

A comparison of the absorbance ratios and MW distributions for NOM experiments with and without Cd (Figures A9-11) showed that, although Cd only slightly affected NOM adsorption overall, preferential adsorption of the higher MW, more aromatic NOM was still indicated. This is consistent with previous reports that higher MW, more aromatic components tend to associate more readily with metals (Cabaniss et al., 2000), and such association could promote adsorption. The shift in the MW distributions of the 'total' adsorbed NOM (i.e., compiled for the four sampling intervals) appeared to be more pronounced in the presence of Cd than in its absence (Figure 2.4). In addition, the increase in effluent M_w occurred more quickly at pH 8 in the 5 ppm C experiments without Cd than with Cd (Table 2.1). The same general trends were observed at pH 6. Thus, preferential adsorption of higher MW NOM was promoted slightly by the presence of Cd. This was not an effect of increased sorption, hence increased competition, because NOM sorption decreased at pH 8. It may indicate that Cd binding to NOM is MW specific or that some other process, such as Cd-induced conformational changes, is occurring.

2.4. Conclusions

The presence of NOM in a system with Cd led to an increase in Cd retention, hence adsorption; Cd slightly decreased overall NOM adsorption but slightly promoted sorption of the higher MW components. This effect would not be detected based on DOC or UV/vis (at 254 nm) of effluent alone. Preferential adsorption of the higher MW

NOM would decrease the mobility of these larger components, and the greater binding ability of the higher MW NOM would also be likely to contribute to the reduced transport of metals and other contaminants, as was observed in the experiments with Cd.

Preferential adsorption of higher MW NOM would lead to enhanced relative mobility of the lower MW components, which are less aromatic and less likely to bind metals and hydrophobic organic compounds. This MW effect could thus act to limit the transport of such contaminants.

Overall, effects of Cd and NOM on each other's adsorption and retention may be a complex function of NOM properties, porous media surface mineralogy, pH, ionic strength, and most likely other parameters as well. Although previous studies using clean quartz sands showed little NOM retention (Weigand and Totsche, 1998; Wei et al., 2010), the presence of (nano)particulate coatings on the quartz grains used here appeared to result in substantial adsorption of NOM, and hence in enhanced Cd retention. Given that nanoparticles may occur not only as coatings on larger grains but also as 'mobile' colloids (Ryan and Gschwend, 1990; Kretzschmar and Schäfer, 2005), the effects of natural Fe and Al oxide nanoparticles and clays on metal fate and transport are likely to be complex, opening many avenues for future investigation.

CHAPTER 3:
EXPERIMENTAL STUDY OF TiO₂ NANOPARTICLE ADHESION TO SILICA AND
Fe(III) OXIDE-COATED SILICA SURFACES

3.1. Introduction

In recent years, the use of engineered nanoparticles has expanded rapidly into a variety of industries, and many consumer products ranging from shampoo and cosmetics to tires and tennis racquets now contain nanoparticles (Wiesner et al., 2006). Titanium dioxide (TiO₂) nanoparticles are especially common in a number of products and are being introduced into aquatic and subsurface geologic systems either inadvertently, such as through the weathering of exterior paint (Kaegi et al., 2008), or intentionally as a tool for environmental remediation (e.g. Mattigod et al., 2005; Pena et al., 2005; Theron et al., 2008; Oyama et al., 2009). TiO₂ nanoparticles exhibit antibacterial properties, which may be beneficial in pharmaceutical applications but are potentially detrimental in environmental systems where unwanted inhibition of bacterial growth has been shown to occur (Adams et al., 2006). In addition, exposure to nano-sized TiO₂ particles may be toxic (Long et al., 2006; Nel et al., 2006; Wiesner et al., 2006; Limbach et al., 2007; Wang et al., 2007; Simon-Deckers et al., 2008; Brunet et al., 2009). However, despite their widespread industrial use and potential release into the environment, the controls on the fate and mobility of TiO₂ nanoparticles in the subsurface are poorly understood.

Both aggregation and surface adhesion can affect the mobility of engineered nanoparticles in geologic systems. Most previous research has focused on aggregation processes, demonstrating the prevalence of TiO₂ nanoparticle aggregates under a wide range of aqueous conditions and with nanoparticles of many sizes (Lecoanet et al., 2004; Dunphy Guzman et al., 2006; Ridley et al., 2006; Choy et al., 2008; Domingos et al., 2009; Jiang et al., 2009; Fatisson et al., 2009; French et al., 2009). In general, nanoparticle aggregation increases with increasing ionic strength, and aggregation also increases as the suspension pH approaches the zero point of charge (pH_{zpc}) of the nanoparticles (e.g., French et al., 2009; Jiang et al., 2009). Aggregate size also increases as the pH approaches the pH_{zpc} (Dunphy Guzman et al., 2006; Fatisson et al., 2009). The presence of other dissolved components, such as cations, organic matter, or surfactants, can also affect the aggregation behavior of TiO₂ nanoparticles (Tkachenko et al., 2006; Domingos et al., 2009; French et al., 2009; Joo et al., 2009).

Nanoparticle aggregation behavior can affect or be affected by interactions with geosorbents (Dunphy Guzman et al., 2006; Choy et al., 2008; Fang et al., 2009; Fatisson et al., 2009; Joo et al., 2009), significantly influencing particle transport. Dunphy Guzman et al. (2006) found that larger aggregates had higher interaction energies, which led to an increase in nanoparticle deposition; however, TiO₂ nanoparticles and their aggregates were still found to be highly mobile under most conditions. Fatisson et al. (2009) found that the deposition rates of TiO₂ nanoparticles onto silica differed depending upon changes in pH and ionic strength due to the effect of these parameters on particle aggregation. Nanoparticle aggregation and deposition were also observed by Fang et al. (2009) to depend upon the characteristics of the soil with which the

nanoparticles were in contact. High ionic strength, pH, and zeta potential affected TiO₂ settling, while increasing the dissolved organic carbon concentration and clay content helped to stabilize the nanoparticles in suspension. In some cases, the formation of large aggregates within soil columns completely prevented their passage (Fang et al., 2009). Using sand columns, Choy et al. (2008) found almost complete retention of TiO₂ nanoparticles, although the roles of straining and adhesion could not be differentiated. Joo et al. (2009) observed similar retention of TiO₂ nanoparticles in silica columns, but in the presence of an adsorbed polymer, nanoparticle transport was enhanced. Thus, TiO₂ nanoparticles remain disaggregated and mobile in certain soils and under certain aqueous conditions, but they aggregate and become immobile due to straining and/or adhesion in others.

There have been few studies to examine the adhesion behavior of TiO₂ nanoparticles onto well-characterized, uniform geosorbents, so quantitative models of nanoparticle transport behavior in geologic systems are poorly constrained. Furthermore, in transport studies such as those conducted by Dunphy Guzman et al. (2006), Choy et al. (2008), Fang et al. (2009), and Joo et al. (2009), it is difficult to differentiate between nanoparticle adhesion and straining of large nanoparticle aggregates in order to understand the relative effects of electrostatic controls versus aggregation controls on TiO₂ transport. In this study, the influence of pH, nanoparticle size, and nanoparticle concentration on the adhesion of TiO₂ nanoparticles to silica grains was determined. One nanoparticle size fraction was also selected for adhesion experiments with iron-coated silica grains in order to determine the effect of geosorbent mineral surface composition on particle adhesion behavior.

3.2. Materials and Methods

3.2.1. Nanoparticles and Geosorbents

TiO₂ nanoparticles of the same crystalline phase and of different sizes were synthesized in a premix flame aerosol reactor by controlling the temperature and residence time history of the particles in the high temperature combustion zone (Jiang et al., 2007). Titanium tetra-isopropoxide (TTIP, 97%, Aldrich) was used as the precursor for synthesizing the TiO₂ particles. The volumetric flow rates of N₂/TTIP, O₂, and CH₄ were precisely controlled by mass flow controllers. Nanoparticle size and morphology were characterized by scanning or transmission electron microscopy (SEM, Model: JEOL 7001LVF FE-SEM; TEM, Model: JEOL 2100F FE-(S)TEM). The nanoparticles were observed to be spherical, and each size fraction contained a range of particle sizes. The average diameters of the three nanoparticle size fractions used in these experiments were 16 nm, 26 nm, and 50 nm. Crystallinity and phase of the material were determined using X-ray diffractometry (XRD) with a Rigaku D-MAX/A9 diffractometer and Cu K α radiation ($\lambda = 1.5418 \text{ \AA}$). The crystalline phase of the material was anatase as determined from the XRD pattern. The resulting nanoparticles were in powder (dry) form and were used without washing. The pH_{zpc} was determined previously to be approximately pH 6 (Jiang et al., 2009).

The geosorbents used in these experiments were amorphous silica (30-60 mesh) purchased from Sigma Aldrich (St. Louis, MO), as well as this same amorphous silica onto which an Fe(III) oxide coating was applied following the procedure of Ams et al. (2004). The silica grains to which the Fe(III) oxide coating was applied will hereafter be

referred to as simply Fe-coated. In order to minimize pH drift during the experiments, the uncoated silica grains were rinsed prior to use at least five times with 0.01 M NaClO₄ that was adjusted to the pH of a given experiment. The last wash was left rotating overnight before decanting. At values above pH 6, it was necessary to readjust the pH with NaOH several times over the course of at least 24 hours in order to obtain a stable pH. The Fe-coating procedure involved rinsing the silica grains at least 20 times with DI water, so the coated silica grains were rinsed only twice more with 0.01 M NaClO₄ at the experimental pH. The final wash solution was left to rotate for about 90 minutes during which HNO₃ or NaOH was added to stabilize the pH at the desired value for each experiment. The shorter equilibration time was used to minimize the removal/dissolution of the Fe-coating. Both the coated and uncoated silica grains were added to the nanoparticle suspensions wet, and the dry weight of the silica grains was determined by evaporating the liquid from the used geosorbents after completion of the experiments.

3.2.2. Sorbent Characterization

BET surface area of the uncoated and Fe-coated silica grains was analyzed using a Coulter SA 3100 (Beckman Coulter Inc., Fullerton, CA). The silica grains were rinsed with DI water to remove fines and allowed to air dry. The coated grains had already been rinsed well and were analyzed without further rinsing. Approximately 0.3 g of each sample was outgassed at 30°C for 20 hours. Surface areas were measured five times, yielding averages of $739.7 \pm 8.6 \text{ m}^2/\text{g}$ for the uncoated particles and $580.6 \pm 14.8 \text{ m}^2/\text{g}$ for the Fe-coated particles.

3.2.3. Batch Experiments

Batch adhesion experiments were conducted at a fixed ionic strength in 0.01 M NaClO₄, at pH 3, 4, 5, 6, 7, and 8. For each pH condition studied, a parent suspension of 0.01 M NaClO₄, containing 200 mg/L TiO₂ nanoparticles, was prepared in a Teflon container immediately prior to conducting experiments in order to minimize nanoparticle aggregation and settling. The 200 mg/L TiO₂ nanoparticle parent suspension was placed into an ultrasonic water bath (210 W, 50/60 Hz) for 20 minutes to ensure proper suspension of the nanoparticles and to minimize aggregation (Jiang et al., 2009). For consistency, following ultrasonication, the same 200 mg/L TiO₂ nanoparticle parent suspension was used to make the nanoparticle concentration standards without exposure to geosorbents, the experimental suspensions to which geosorbent grains were added, and the experimental geosorbent-free controls that were used to quantify loss to the labware. The nanoparticle concentrations in these suspensions ranged from 2-200 mg/L, and all were made in 30 mL Teflon jars. All of these suspensions were then placed into the ultrasonic water bath for an additional 20 minutes. Immediately following the second ultrasonication, the nanoparticle concentration in each suspension was analyzed by measuring light absorbance from 800-350 nm.

Experiments using the uncoated silica grains were conducted using each of the three sizes of TiO₂; the experiments that involved the Fe-coated silica grains were conducted using only the 26 nm TiO₂ size fraction. To each of the experimental suspensions, 0.5 g of silica grains or Fe-coated silica grains (dry weight) was added. The pH of each standard, experiment, and experimental control was then measured and adjusted if necessary using minute aliquots of concentrated HNO₃ or NaOH, and all

systems were rotated for 3 hours, with hourly pH measurements and readjustments. After the 3 hour reaction time, the final pH of each suspension was measured. The final pH value of each suspension was within ± 0.1 pH units of the desired experimental pH. The geosorbent grains settled as soon as the experimental suspensions were removed from the rotator, and the supernatant from each experiment was transferred with a pipette to a 28 mL Teflon tube. Any settling of the nanoparticles due to aggregation was expected to be identical to the settling that would occur in the standards under the same conditions. The experimental control suspensions were also transferred to Teflon tubes in the same manner as the experimental suspensions in order to evaluate nanoparticle loss to the Teflon jars during the 3 hour reaction time. Standard suspensions were never moved from the Teflon jars, which meant that any nanoparticles adhered to the container walls could be resuspended during the final ultrasonication step.

3.2.4. UV/vis Analysis

All UV/vis analyses were conducted with a Varian Cary 300 Bio UV/Visible double-beam spectrophotometer. A series of absorbance control experiments were conducted that demonstrated that the UV/vis light absorbance profiles over the wavelengths tested for nanoparticle-bearing aqueous suspensions varied markedly with suspension pH, nanoparticle size, and nanoparticle concentration. As was typical for the other nanoparticle sizes and concentrations, the absorbance of the 26 nm TiO₂ at 50 mg/L was lowest at pH 3 and 4 and was markedly higher for suspensions at pH 5-8 (Figure 3.1a). Absorbance also depended upon particle size, with the larger particles typically exhibiting greater light absorbance, especially at the lower wavelengths (Figure 3.1b).

The length of time that the nanoparticle suspensions were allowed to react also influenced the absorbance profiles (data not shown), likely due to aggregation over time and, if allowed to sit long enough, settling. Because of the effects of pH, particle size, and particle aggregation on the UV/vis absorbance behavior of nanoparticle suspensions, the nanoparticle concentration standards, the experimental samples, and the experimental control suspensions were all made following the same procedures and under the same pH conditions. New standards were made for each experiment to eliminate the effects of time on the extent of aggregation.

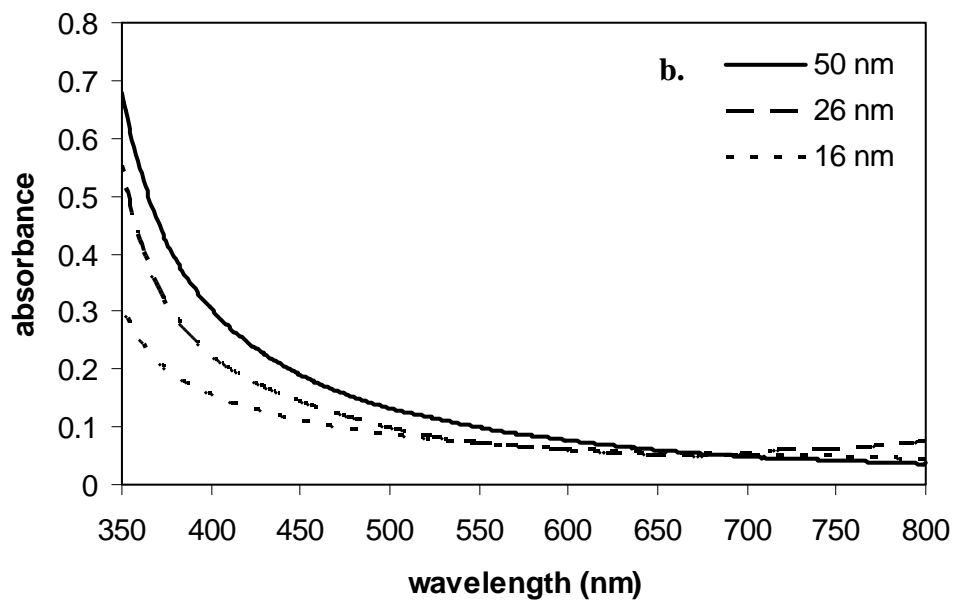
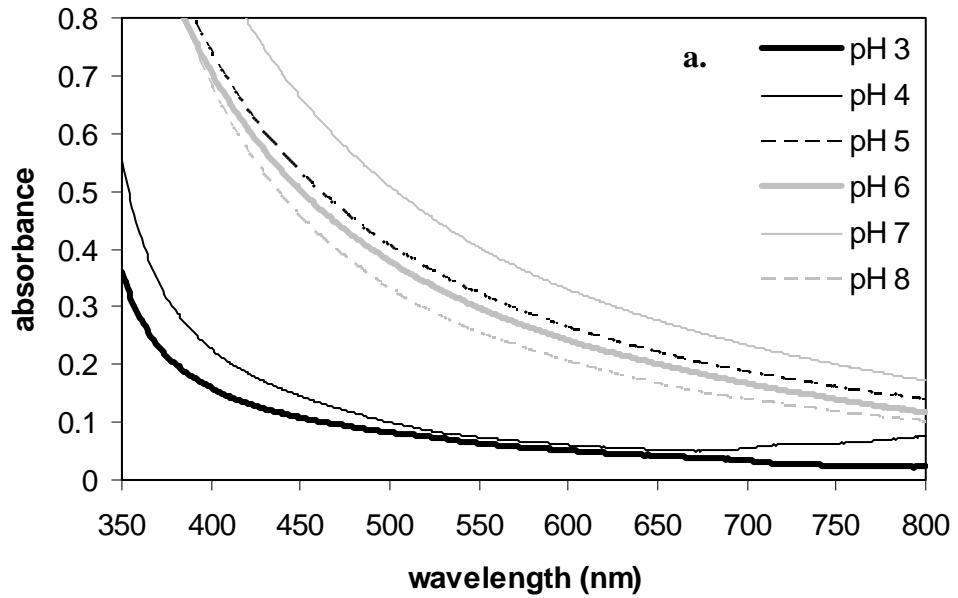


Figure 3.1: a) pH dependence of the 50 mg/L standards for the 26 nm TiO₂ particles from pH 3-8. b) Particle size dependence of the 50 mg/L standards at pH 4.

Prior to each UV/vis measurement, all suspensions were placed in an ultrasonic water bath for 40 minutes and afterward were immediately scanned from 800-350 nm. Using absorbance at 750 nm after background subtraction, calibration curves were created from the standard suspensions and were used to calculate the nanoparticle concentrations remaining in the samples taken from the geosorbent-bearing experiments. The concentration of nanoparticle adhered to the geosorbent was calculated by difference. Selection of 750 nm as the wavelength of interest is explained in Section 3.3.1.1.

Anomalous absorbance behavior was observed at pH 3 and 4 in the Fe-coated silica experiments. Under these pH conditions, the experimental nanoparticle suspensions that were exposed to Fe-coated silica grains exhibited extents of UV/vis absorbance that were higher than their starting absorbance profiles. Background subtraction of a 0.01 M NaClO₄ solution that was rotated with Fe-coated silica for 3 hours was used to account for the portion of each absorbance profile that resulted from the suspension of Fe(III) oxide particles that may have been removed from the Fe-coated silica grains. However, this correction accounted for only a small portion of the observed increase, suggesting that the remainder of the increased absorbance profiles could be attributed to the effects of dissolved iron on nanoparticle aggregation. To test the possible effects of the partial dissolution of the iron coatings, iron control experiments at three different pH values were conducted. 0.01 M NaClO₄ at pH 4, 5, or 8 was rotated with Fe-coated silica for 3 hours with no nanoparticles present in the system. This Fe-0.01 M NaClO₄ solution was then used to make 50 mg/L TiO₂ nanoparticle suspensions, while unexposed 0.01 M NaClO₄ was used to make additional 50 mg/L suspensions. All of these 50 mg/L suspensions were then subjected to the same experimental procedure as

described above, and the absorbance profiles of the suspensions made in Fe-0.01 M NaClO₄ were compared to those made in Fe-free 0.01 M NaClO₄. The absorbance profiles of the pH 4 controls were found to depend upon the background solution used (see Figure B1), with the suspension prepared in the Fe-0.01 M NaClO₄ exhibiting an increased absorbance profile compared to the suspension prepared in Fe-free 0.01 M NaClO₄. This difference was not observed in the control experiments conducted at pH 5 and 8. It is likely that significant concentrations of dissolved Fe under pH 3 and 4 conditions altered the aggregation behavior of the nanoparticle suspensions that were reacted with Fe-coated silica grains, enhancing the extent of UV/vis light absorbance. For this reason, due to difficulties in quantifying the effect, experimental results for the pH 3 and 4 experiments involving Fe-coated grains are not reported.

3.2.5. Adhesion Isotherm Calculations

The Langmuir isotherm approach was used to model the experimental nanoparticle adhesion data. The Langmuir approach is based on the assumption of a finite supply of reaction sites (Langmuir, 1997), and the Langmuir isotherm equation can be expressed as:

$$\frac{x}{m} = \frac{bCN_{\max}}{1 + bC} \quad (3.1)$$

where $\frac{x}{m}$ is the mass of the sorbate (mg TiO₂) divided by the mass of the sorbent (g dry silica grains), b is a constant (L/mg), and C is the concentration of sorbate remaining in suspension (mg TiO₂/L) after equilibration. N_{\max} is the maximum possible adhesion by the sorbent (mg/g) under the experimental conditions, and the Langmuir constant, K_L , is

defined as: $K_L = bN_{max}$. At low sorbate concentrations, K_L approaches the linear distribution coefficient K_d and a linear relationship between C and $\frac{x}{m}$ exists. A linearized form of Equation (3.1) can be expressed as:

$$\frac{1}{\frac{x}{m}} = \frac{1}{bCN_{max}} + \frac{1}{N_{max}} \quad (3.2)$$

Plotting the experimental data as $\frac{1}{\frac{x}{m}}$ vs. $\frac{1}{C}$ and calculating the slope and intercept of

the best-fit line to the data yields values for $(\frac{1}{bN_{max}})$ and $(\frac{1}{N_{max}})$, respectively, and these

values were used to calculate values for K_L and N_{max} . The dataset included a few outlier points which occurred outside the 2σ uncertainty envelope of the linear trend of the data. These data points were plotted in the isotherms but were ignored when calculating N_{max} and K_L values. A number of the datasets, when plotted as isotherms, did not exhibit significant departures from the linearity that characterizes the low C region. When plotted using Equation (3.2), these datasets yielded negative y-intercepts and, hence, negative N_{max} values. These physically impossible values suggest that N_{max} was poorly defined by the data under these conditions, and that adsorption experiments to much higher nanoparticle concentrations would need to be conducted in order to observe the non-linear isotherm behavior that constrains the N_{max} value. In these cases, the K_d equation was used:

$$\frac{x}{m} = K_d C \quad (3.3)$$

which is equivalent to the Langmuir equation at low sorbate concentrations, to model the adhesion results.

3.3. Results and Discussion

3.3.1. UV/vis Absorbance Profiles

3.3.1.1. *Uncoated Silica Grains*

In order to calculate the nanoparticle concentrations remaining in suspension after exposure to the silica grains, it was necessary to select an appropriate wavelength at which to calculate the calibration curves. For the pH 3 experiments, the standards and the suspensions that were reacted with silica grains exhibited UV/vis absorbance profiles with similar shapes (Figure 3.2). Under these conditions, the choice of wavelength affected neither the calibration curve nor the calculated TiO₂ concentrations in the suspensions that were exposed to silica grains. For example, the UV/vis absorbance profile for the 50 nm suspension that started at 200 mg/L indicated that the final suspension concentration was approximately 150 mg/L (Figure 3.2), regardless of the wavelength chosen for the calibration curve. The similarity in absorbance profile shapes between the standards and the experimental samples suggests that adhesion occurring under these conditions did not markedly change the size distribution of the TiO₂ nanoparticle suspensions under pH 3 conditions.

Conversely, at pH 4, the standards and the suspensions that were reacted with silica grains exhibited markedly different UV/vis absorbance profile shapes (Figure 3.3a). The absorbance profiles of the 50 nm TiO₂ suspensions that were exposed to silica grains

not only decreased due to nanoparticle removal from suspension, but they were also shallower than the 50 nm standards at wavelengths shorter than 650 nm. Because the sample suspensions did not exhibit UV/vis absorbance profiles that were parallel to the standards under these conditions, the calculated concentration of TiO₂ nanoparticles in the samples was strongly dependent on the choice of wavelength used to construct the calibration curve. For example, a calibration curve using absorbance of the samples and standards at 650 nm would indicate that approximately 100 mg/L of the suspension that started at 200 mg/L prior to silica grain contact remained in suspension, but a calibration curve using 350 nm would indicate that only 50 mg/L remained (Figure 3.3a).

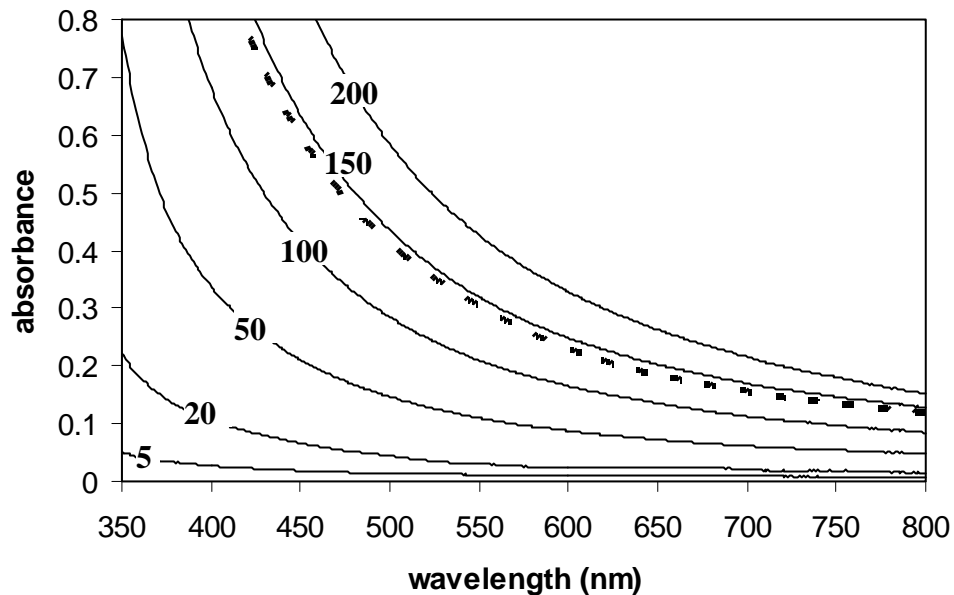


Figure 3.2: 50 nm TiO₂ standards (in mg/L) at pH 3 are shown as black solid curves. The dashed curve is the absorbance profile for the 200 mg/L 50 nm TiO₂ suspension after it was exposed to silica particles at pH 3. Note the agreement in the shapes of the absorbance profiles.

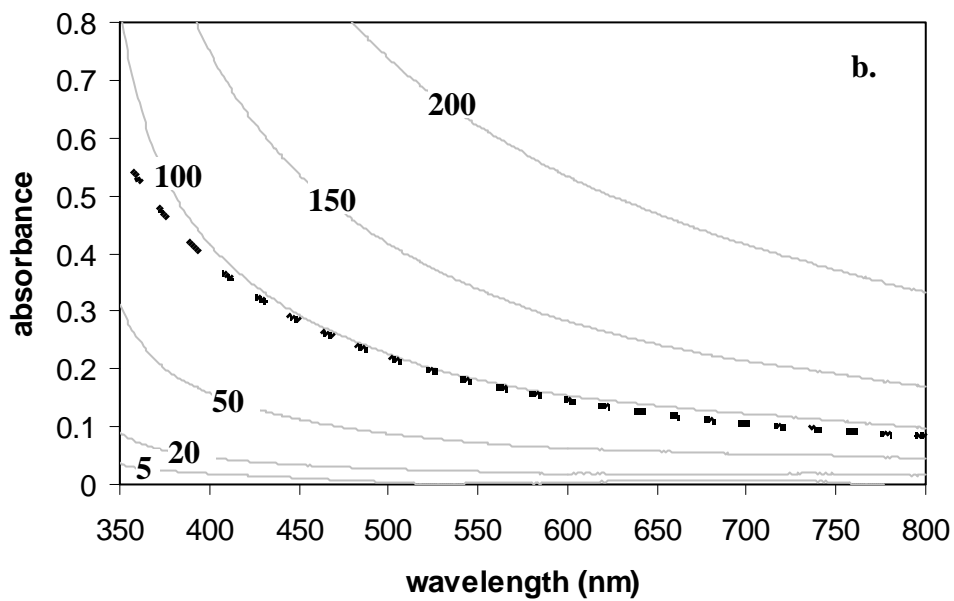
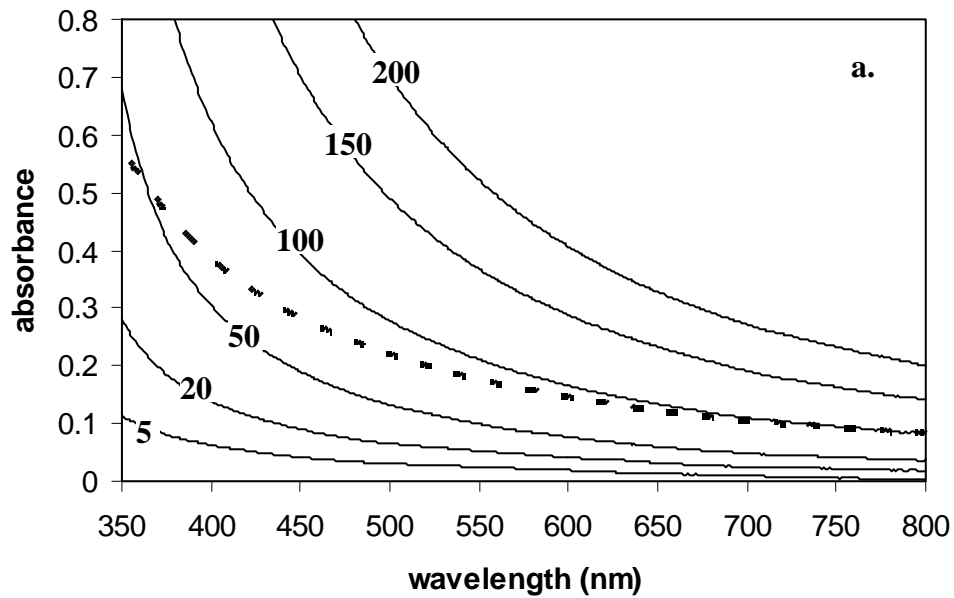


Figure 3.3: a) 50 nm TiO₂ standards (in mg/L) at pH 4 are shown as black solid curves. The dashed curve is the absorbance profile of the 200 mg/L 50 nm TiO₂ suspension after it was exposed to silica particles at pH 4. b) 16 nm TiO₂ standards (in mg/L) at pH 4 are shown as gray solid curves. The dashed curve is the absorbance profile of the 200 mg/L 50 nm TiO₂ suspension after it was exposed to silica particles at pH 4.

Although at pH 4 the 50 nm standards did not provide a good match to the UV/vis absorbance profiles of the 50 nm samples, the absorbance profiles of the 16 nm standards were almost identical to the profiles of the 50 nm samples except below approximately 400 nm (Figure 3.3b). As demonstrated in Figure 3.1b, the steepness of the UV/vis absorbance profiles of nanoparticle suspensions decreased with decreasing particle size. Therefore, the fact that the UV/vis absorbance profiles for the 50 nm suspensions became less steep during interaction with the silica grains strongly suggests that the larger nanoparticles within these suspensions preferentially adhered to the silica surface, leaving the smaller TiO₂ in suspension and resulting in size fractionation. Flattening of the UV/vis absorbance profile of a suspension that was placed in contact with silica grains was also observed under the following conditions: at pH 4 below 650-700 nm in experiments with 26 nm and 16 nm TiO₂ particles and at pH 5 below 750 nm in experiments with 50, 26, and 16 nm TiO₂. For this reason, calibration curves for all experiments were calculated with absorbance values collected at 750 nm where the slopes of the absorbance profiles of the standards and of the suspensions exposed to silica grains were generally in agreement.

The 50 nm experimental samples at pH 6 yielded steeper UV/vis absorbance profiles than did the 50 nm standards at pH 6, especially at wavelengths below 650 nm where the absorbance for a sample could even exceed the absorbance for a standard with the same original nanoparticle concentration. A steeper absorbance profile relative to the standards was also noted in the 26 nm pH 6 experiments below 650 nm and in the 16 nm experiments below 500 nm. The same trends were observed at pH 8. At pH 7 (Figure 3.4), the steepening of the absorbance profiles of the suspensions exposed to silica grains

was more pronounced, and deviations from the standards occurred below 700, 750, and 550 nm for the 50, 26, and 16 nm TiO₂, respectively. The increased absorbance profiles of the nanoparticle suspensions exposed to silica grains compared to the unexposed standards suggests preferential adhesion of the smaller TiO₂ particles within a given size fraction, the opposite of what was observed in experiments conducted at pH < 6. Again, the absorbance values at 750 nm were used to calculate the concentration of nanoparticles remaining in suspension because the standards and suspensions exposed to silica grains exhibited similar absorbance profile slopes at this wavelength.

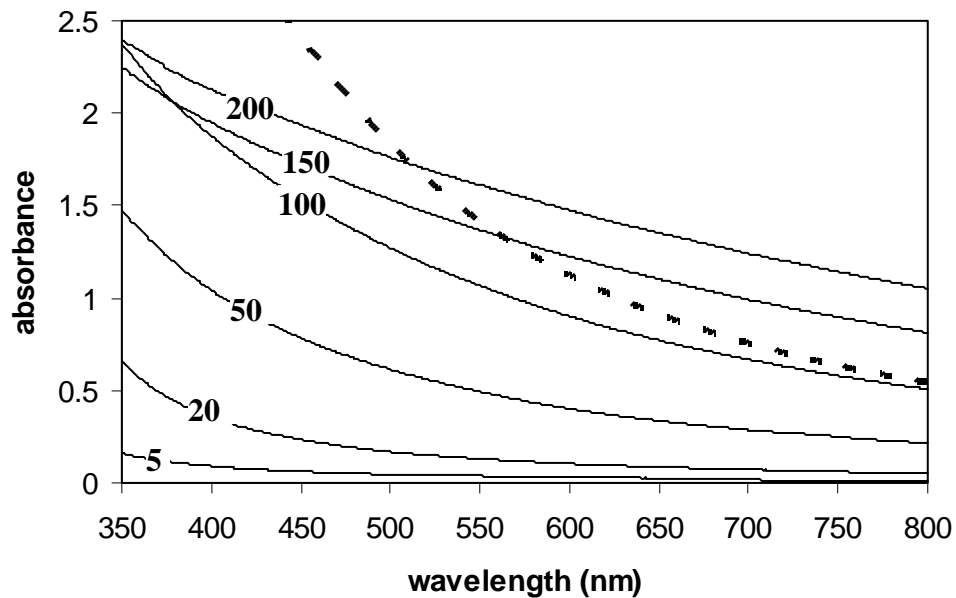


Figure 3.4: 50 nm TiO₂ standards (in mg/L) at pH 7 are shown as black solid curves. The dashed curve is the absorbance profile of the 200 mg/L 50 nm TiO₂ suspension after it was exposed to silica particles at pH 7.

3.3.1.2. *Iron-Coated Silica Grains*

The changes in the absorbance profiles between the 26 nm TiO₂ standards and the 26 nm suspensions exposed to Fe-coated silica grains were generally similar to what was seen in the experiments with uncoated silica, and the UV/vis absorbance profiles for these samples are not depicted. At pH 5, the absorbance profiles of the suspensions exposed to the Fe-coated silica grains exhibited a shallower slope than the standard suspensions below 700 nm. At pH 6, 7, and 8, there was a steepening in the absorbance profiles of the exposed suspensions compared to the standards below approximately 650 nm, although these increases were slight at pH 6 and 8. For these reasons, absorbance at 750 nm was used to calculate the nanoparticle concentrations remaining in suspension in all cases.

3.3.2. TiO₂ Adhesion

3.3.2.1. *Uncoated Silica Grains*

Because adhesion of TiO₂ nanoparticles onto the geosorbents appeared to affect the particle size distribution of the suspensions differently under different pH conditions, it was impossible to perfectly match the particle size distribution of a sample suspension with that of the standards. However, following the approaches outlined above, the most appropriate wavelength was used to calculate the nanoparticle concentrations remaining in suspension and, by difference with the starting concentrations, the adhered nanoparticle concentrations from each set of experiments. In general, the extent of nanoparticle adhesion onto uncoated silica grains increased with increasing nanoparticle concentration, which is typical isotherm behavior (Figure 3.7). However, the sorbent

capacity for adhesion varied markedly as a function of pH, as can be seen by comparing the experimental data to the 100% adhesion lines shown in Figure 3.7a-f. To examine this pH dependence more closely, adhesion as a function of pH is shown for the experiments involving nanoparticle concentrations of 115 mg/L and 175 mg/L (Figure 3.8). pH strongly influenced the adhesion behavior of the three nanoparticle sizes, but it was not a straightforward relationship. Below pH 6, the expected pH_{zpc} for our TiO_2 , the concentration of adhered nanoparticle increased with increasing pH (from 3 to 5) with almost complete removal at pH 5. The 50 and 26 nm TiO_2 adhered similarly at pH 3 and 4, with more of the 50 nm particles removed at pH 5. At pH 3-5, the 16 nm TiO_2 consistently adhered the least of the three sizes. The size effect can be significant, especially at pH 4 where the amount adhered ranges from 84% of the initial 115 mg/L for the 50 nm TiO_2 down to 40% of the 16 nm TiO_2 (Figure 3.8a). Thus, adhesion increased with increasing pH and particle size below pH 6. From pH 5 to 6, all nanoparticle sizes exhibited a decrease in adhesion, and adhesion was independent of pH and nanoparticle size at pH 6 and above. However, it should be noted that the percent of TiO_2 adhered changed much less between pH 6 and 8 than it did between pH 3 and 5.

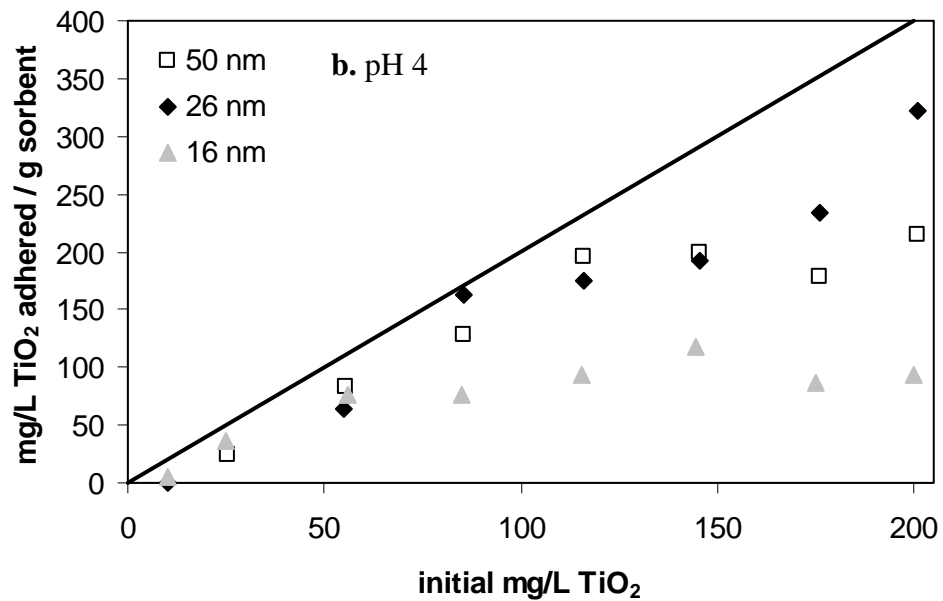
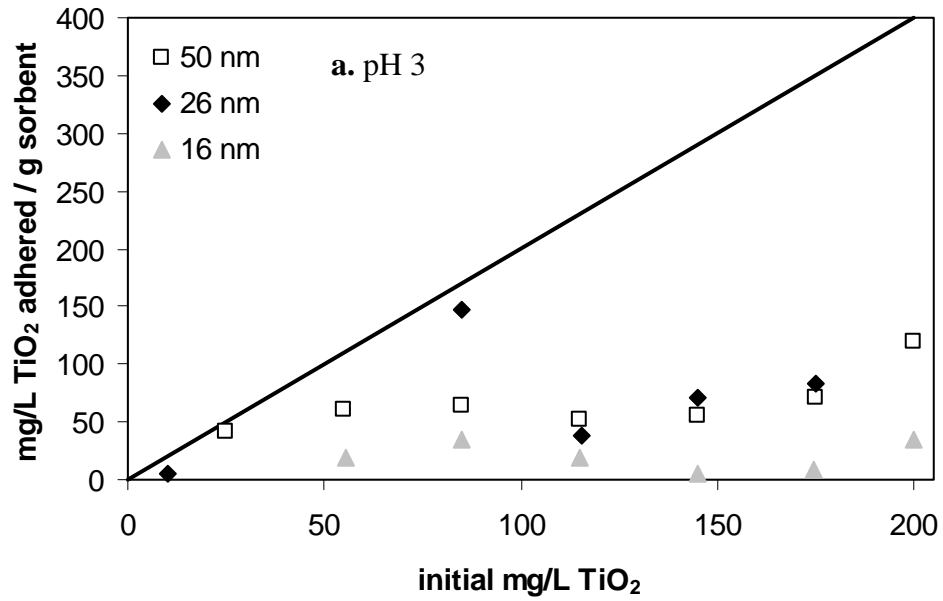


Figure 3.5: TiO₂ nanoparticle adhesion to uncoated silica grains at pH 3-8 (a-f). Open squares represent the 50 nm TiO₂, black diamonds the 26 nm TiO₂, and gray triangles the 16 nm TiO₂. The black line represents 100% adhesion. In cases where adhesion was close to the detection limit, the data are not presented (p. 48-p. 50).

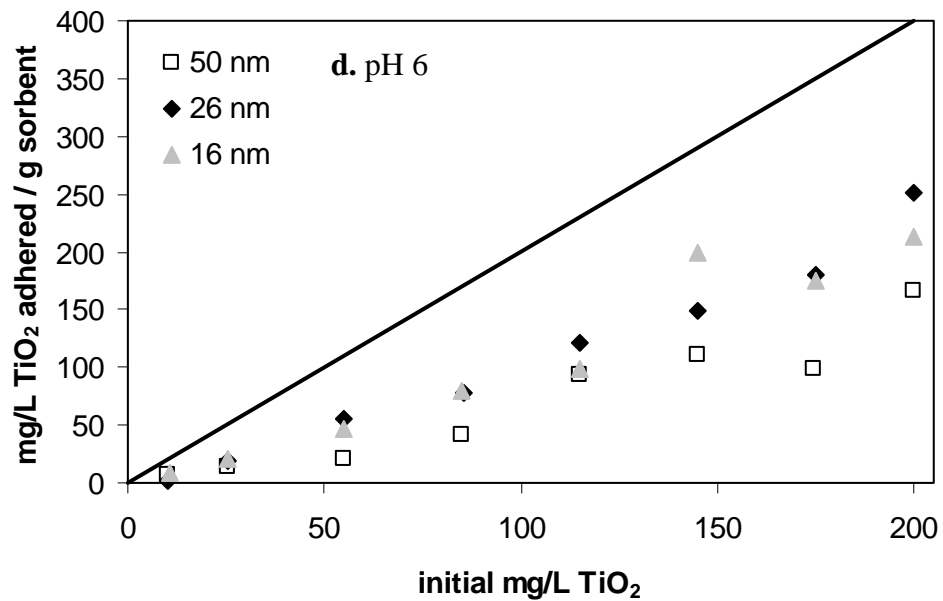
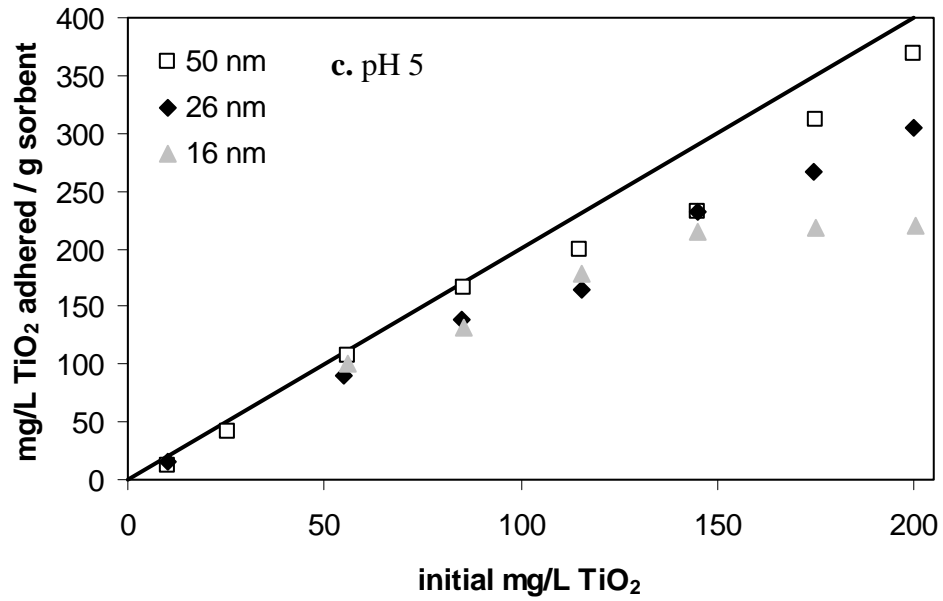


Figure 3.6: TiO₂ nanoparticle adhesion to uncoated silica grains at pH 3-8 (a-f). Open squares represent the 50 nm TiO₂, black diamonds the 26 nm TiO₂, and gray triangles the 16 nm TiO₂. The black line represents 100% adhesion. In cases where adhesion was close to the detection limit, the data are not presented (p. 48-p. 50).

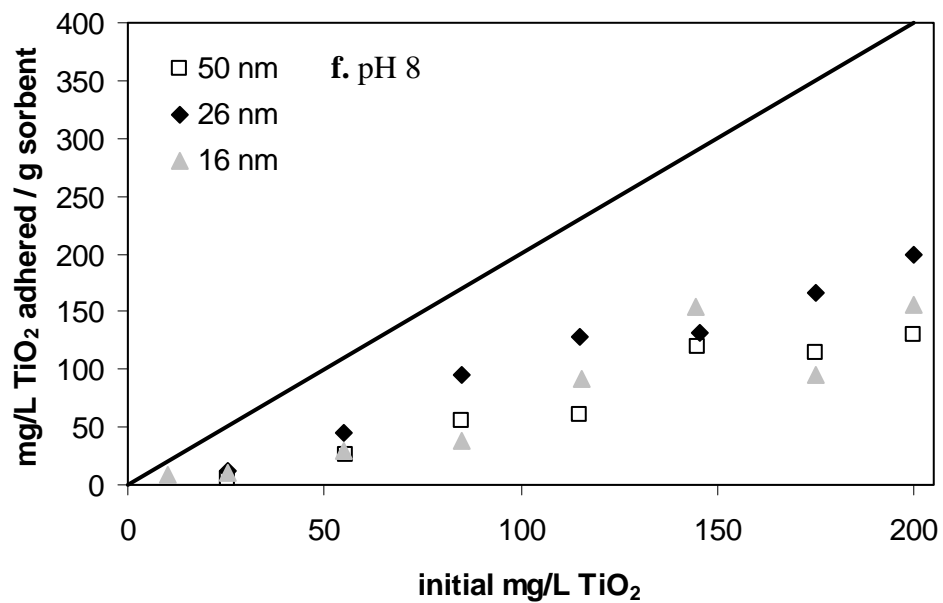
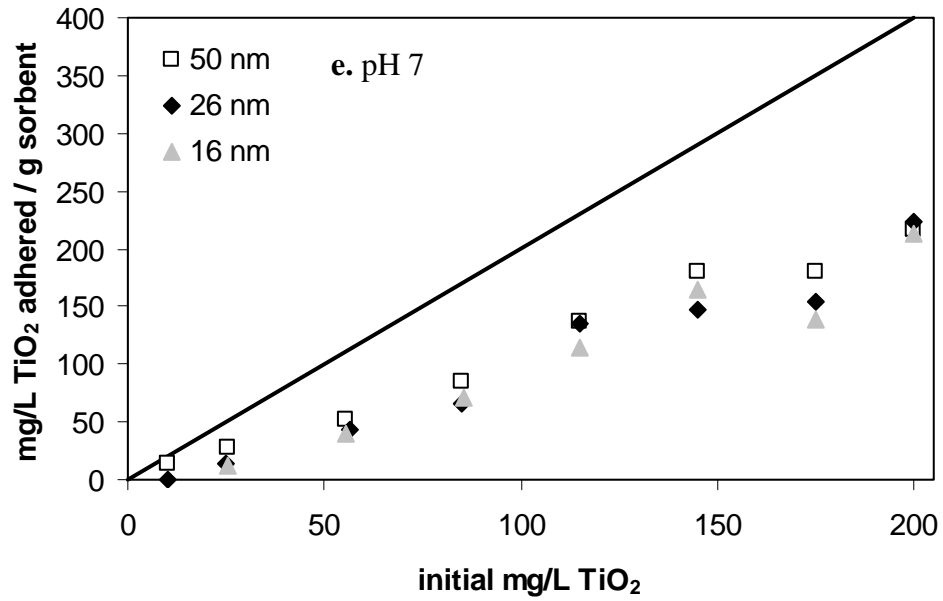


Figure 3.7: TiO₂ nanoparticle adhesion to uncoated silica grains at pH 3-8 (a-f). Open squares represent the 50 nm TiO₂, black diamonds the 26 nm TiO₂, and gray triangles the 16 nm TiO₂. The black line represents 100% adhesion. In cases where adhesion was close to the detection limit, the data are not presented (p. 48-p. 50).

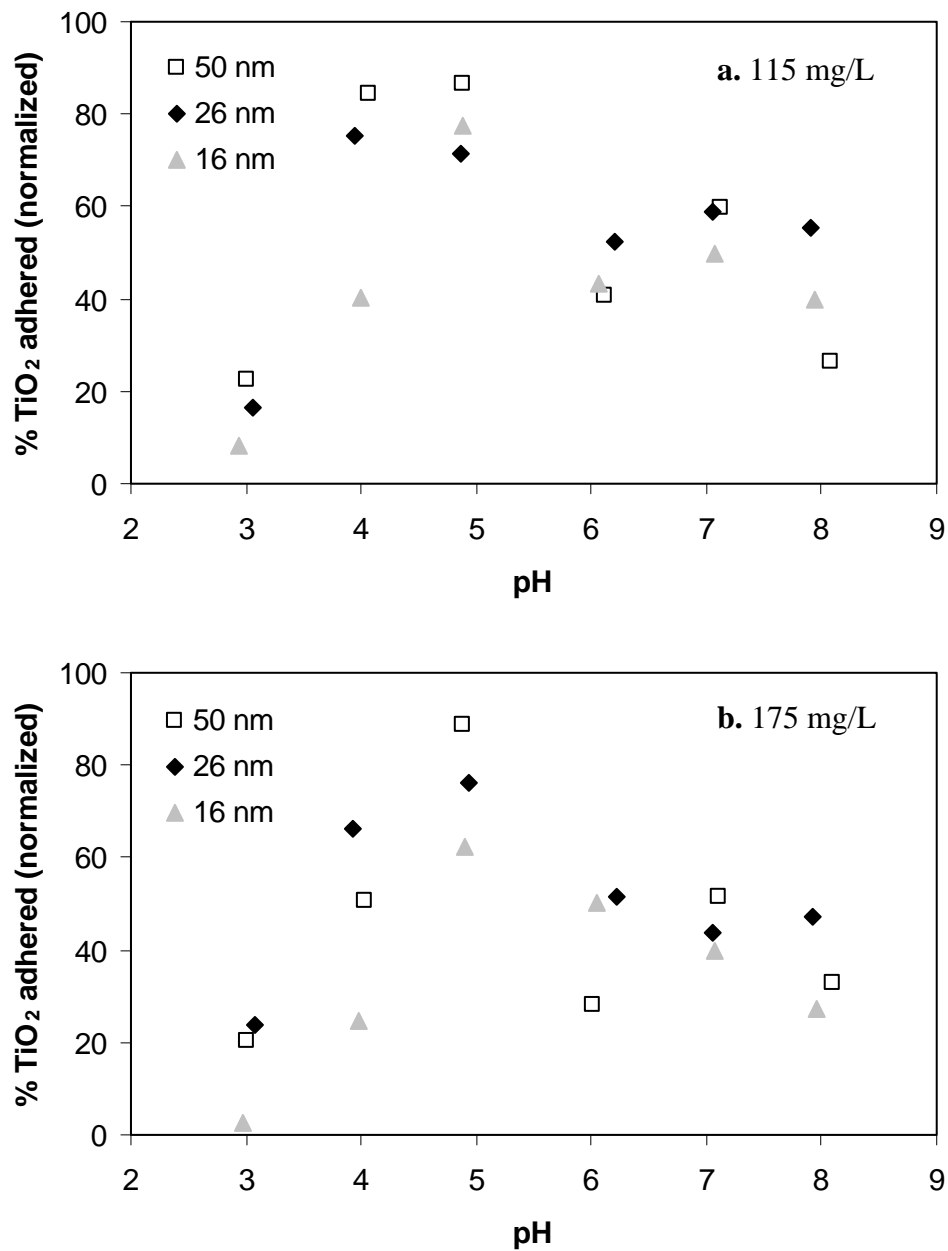


Figure 3.8: The extent of nanoparticle adhesion onto uncoated silica grains as a function of pH, shown for all three TiO₂ nanoparticle sizes at two initial concentrations: a) 115 mg/L and b) 175 mg/L.

3.3.2.2. *Iron-Coated Silica Grains*

The mineralogy and/or surface charge of the geosorbent did not markedly affect the observed extents of adhesion (Figure 3.9). As was observed for the uncoated silica grains, nanoparticle adhesion onto the Fe-coated grains increased with increasing nanoparticle concentration (see Figure B2). Generally, nanoparticle adhesion to the coated and uncoated silica grains was similar from pH 5-8, except at pH 6 where a significantly higher concentration of nanoparticles adhered to the Fe-coated grains compared to the uncoated grains.

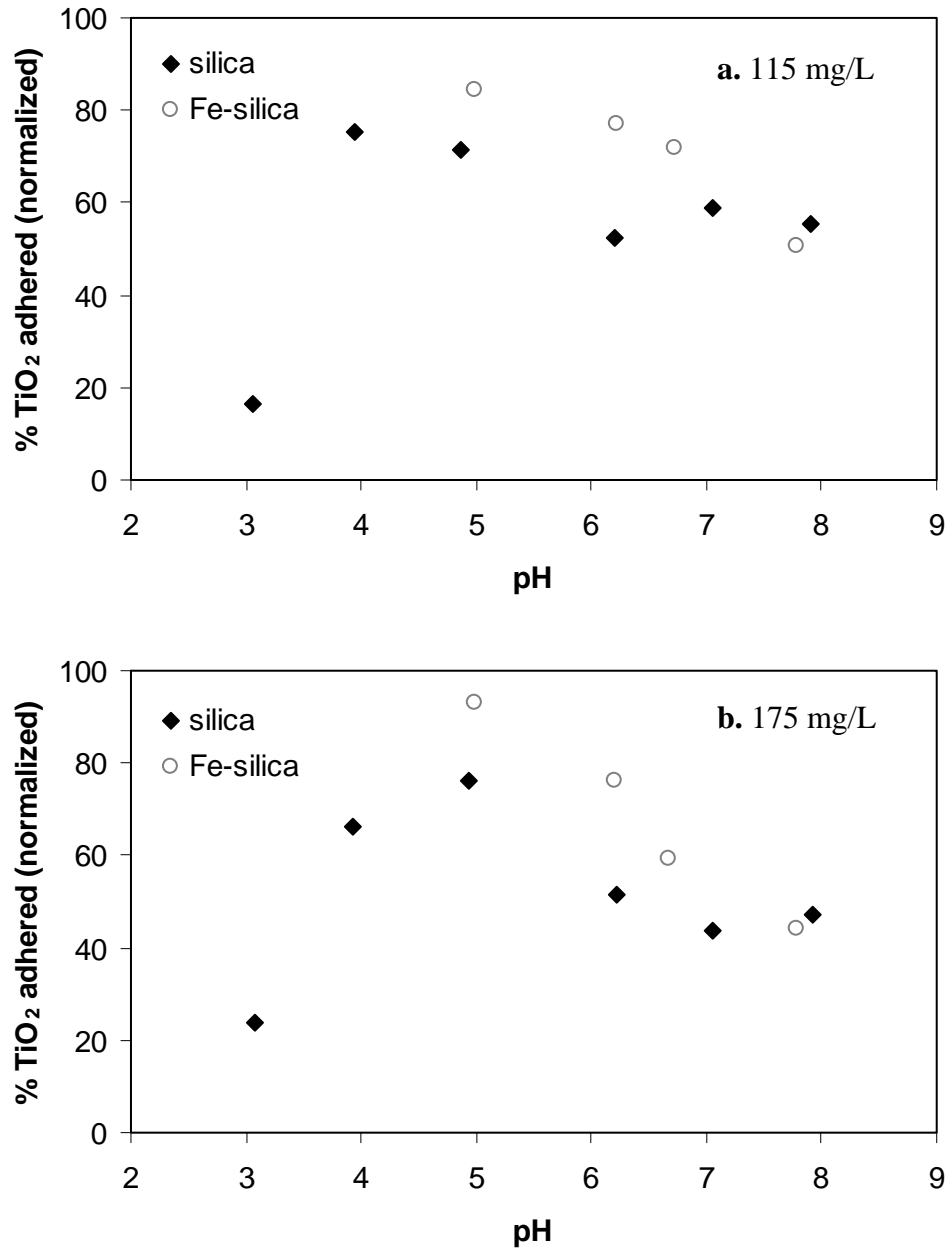


Figure 3.9: The extent of 26 nm TiO₂ adhesion onto uncoated and Fe-coated silica grains as a function of pH at two initial concentrations: a) 115 mg/L and b) 175 mg/L.

These results suggest that adhesion behavior is not controlled by electrostatic forces between the TiO₂ nanoparticles and the geosorbent surfaces. At the pH values used in these experiments, the charge on the silica grains is negative, and the p*H*_{zpc} of the TiO₂ is approximately pH 6. If adhesion is based purely upon electrostatics, then a decrease in TiO₂ adhesion onto the uncoated silica grains would be expected with increasing pH over the entire pH range of this study. Instead, increasing adhesion from pH 3 to pH 5 was observed, with lower extents of adhesion and pH-independent behavior at higher pH values. Furthermore, the surface charges of the uncoated and Fe-coated silica grains are quite different, with the p*H*_{zpc} of the coated grains expected to be between pH 7 and 8 (Ams et al., 2004). Again, based upon electrostatic considerations only, minimal adhesion would be expected below pH 6 where both the nanoparticles and the Fe-coated silica grains are positively charged. From pH 6-7, an increase might be expected where the charges are opposite, but above pH 7 both surfaces are negatively charged and electrostatic repulsive forces would be large. However, the adhesion behaviors of the two geosorbents are broadly similar. It should also be noted that the high BET surface areas measured for both types of geosorbents suggest that the availability of surface sites should not be a limiting factor for TiO₂ adhesion.

The changes in adhesion as a function of pH and the similarities in TiO₂ nanoparticle adhesion onto the silica and Fe-coated silica grain surfaces suggest that it is some property of the nanoparticles that governs their adhesion. Nanoparticle aggregation is strongly affected by suspension pH, with aggregation increasing as the p*H*_{zpc} is approached. Changes in UV/vis absorbance as a function of pH were observed that are suggestive of changes in aggregation. For these reasons, it is likely that the aggregation

state of the nanoparticles plays a dominant role in determining the extent of TiO₂ nanoparticle adhesion onto mineral surfaces.

Differences in nanoparticle surface properties as a function of particle size could explain the observed effects of nanoparticle size on particle adhesion onto the silica grains. For example, nanoparticulate anatase adsorbed less Cd and Pb from solution than larger-grained anatase when normalized to the nanoparticle surface area (Gao et al., 2004; Giammar et al., 2007). Similarly, Waychunas et al. (2005) observed that Hg(II) adsorption onto nanoparticulate goethite decreased with decreasing particle size when adsorption was normalized to surface area, perhaps due to increased disordering on the smaller particle surfaces. Increasing disorder with decreasing nanoparticle size has been observed for hematite and ferrihydrite nanoparticles (Chernyshova et al., 2007; Michel et al., 2007). However, Jiang et al. (2008) found that surface defect sites were more common per unit area on larger TiO₂ particles, and Zhang et al. (2009) observed conflicting effects occurring with decreasing particle size: an increasing proportion of high energy sites led to an increase in surface free energy, but increases in internal distortion decreased surface free energy. It is not clear at this point whether aggregation effects, surface reactivity effects, or other factors cause the differences in the extent of adhesion observed for the different nanoparticle sizes.

3.3.2.3. *TiO₂ Adhesion Isotherms*

The Langmuir adsorption isotherm equation provided a good fit to most of the experimental measurements of TiO₂ nanoparticle adhesion. An example of the model fits for the pH 5 data is shown in Figure 3.10 in both isotherm format (Figure 3.10a for all

particle sizes) and the $\frac{1}{x/m}$ vs. $\frac{1}{C}$ format (Figure 3.10b for the 26 nm particle experiments only). The calculated isotherm parameters for all of the experiments are compiled in Table 3.1. For cases with N_{max} values reported in Table 3.1, there was good linear correlation between $\frac{1}{x/m}$ and $\frac{1}{C}$ (with R^2 values ranging from 0.73 to 0.99), suggesting that the Langmuir model provided a good fit to the experimental data. For the cases with N_{max} values that were not defined by the data, there was a good linear correlation between $\frac{x}{m}$ and C , and hence the K_d approach provided a better representation of the adhesion behavior in these cases (e.g, the 50 nm particle experiments depicted in Figure 3.10a), with R^2 values ranging from 0.70 to 0.99.

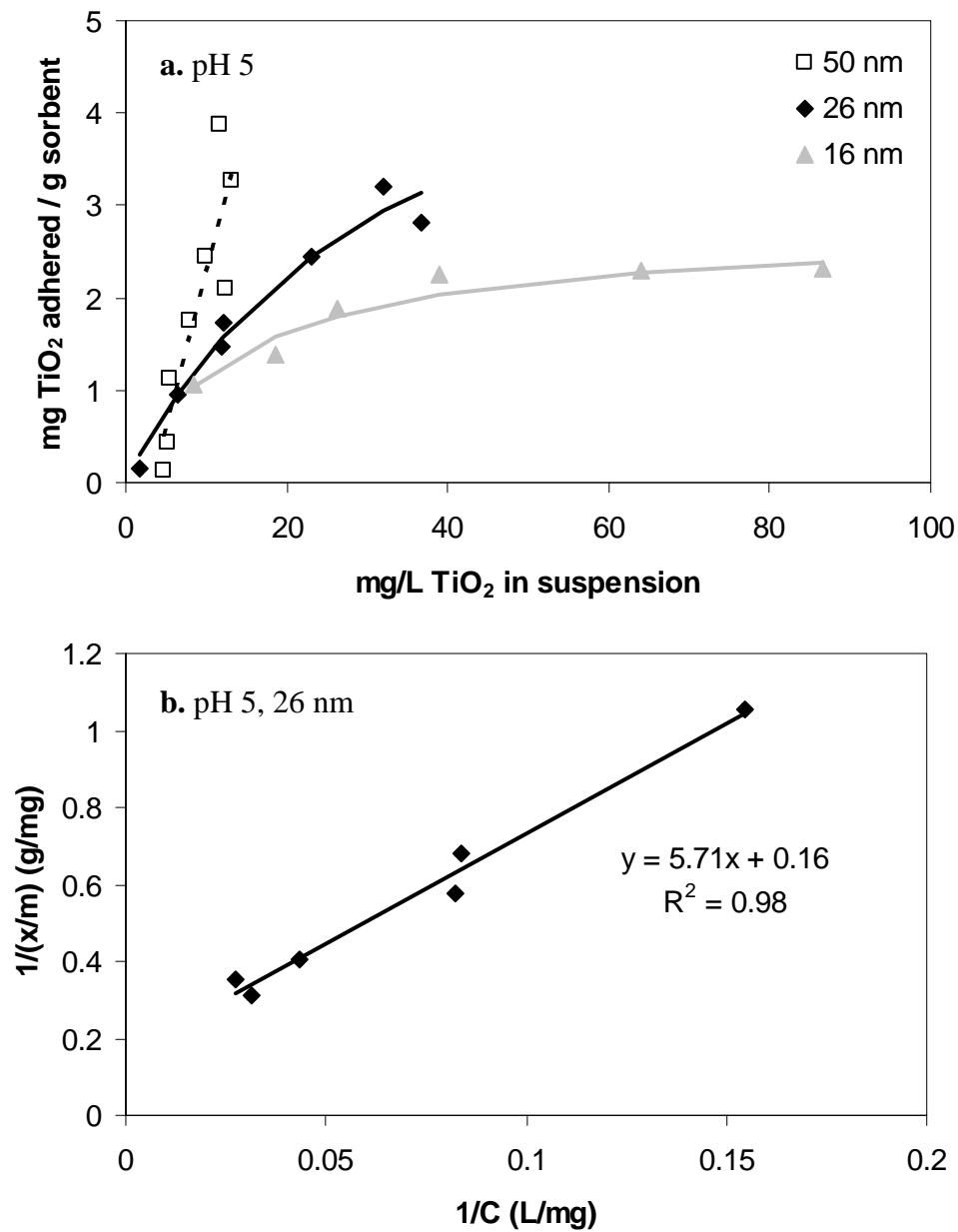


Figure 3.10: a) Adhesion isotherms from experiments involving uncoated silica grains at pH 5 for all three nanoparticle sizes. The experimental data are shown as squares (50 nm), diamonds (26 nm), and triangles (16 nm). The calculated Langmuir isotherms are shown as the black (26 nm) and gray (16 nm) lines, and the K_d fit is the dashed line (50 nm). b) The Langmuir linearization of the 26 nm experimental data at pH 5 with the calculated linear regression equation.

TABLE 3.1
ISOTHERM FIT PARAMETERS

pH	K_L (L/g)	K_d (L/g)	N_{max} (mg/g)	R^2
50 nm TiO₂ on silica grains				
pH 3	1.7×10^{-1}		0.75	0.99
pH 4	7.7×10^{-2}		3.8	0.76
pH 5		3.4×10^{-1}	NR	0.99
pH 6	8.9×10^{-3}		4.7	0.97
pH 7	4.0×10^{-2}		2.2	0.96
pH 8		1.2×10^{-2}	NR	0.89
26 nm TiO₂ on silica grains				
pH 3	6.6×10^{-3}		3.3	0.99
pH 4		4.8×10^{-2}	NR	0.70
pH 5	1.8×10^{-1}		6.2	0.98
pH 6		2.9×10^{-2}	NR	0.98
pH 7		2.4×10^{-2}	NR	0.80
pH 8		2.1×10^{-2}	NR	0.89
26 nm TiO₂ on Fe(III) oxide-coated silica grains				
pH 5	3.4×10^{-1}		4.0	0.98
pH 6		8.2×10^{-2}	NR	0.99
pH 7	5.3×10^{-2}		9.5	0.99
pH 8		2.1×10^{-2}	NR	0.87
16 nm TiO₂ on silica grains				
pH 3	6.9×10^{-3}		0.65	0.73
pH 4	9.6×10^{-2}		1.2	0.94
pH 5	1.9×10^{-1}		2.8	0.95
pH 6		2.7×10^{-2}	NR	0.96
pH 7		2.4×10^{-2}	NR	0.88
pH 8	1.9×10^{-2}		1.3	0.95

NOTE: K_L , N_{max} , and R^2 were calculated from the linearized Langmuir equation. In cases where a negative N_{max} was obtained, the value is not reported (NR) and values for the linear distribution coefficient (K_d) and its fit to the data (R^2) are given instead.

A calculated N_{max} value represents the maximum extent of adhesion possible under a particular set of conditions. Because N_{max} is thought to represent monolayer coverage of the sorbent surface, and because results from experiments with the same concentration of sorbent available for adhesion are compared, the changes in N_{max} values likely reflect changes in aggregation behavior. For example, the N_{max} values for the data shown in Figure 3.10a for the 26 and 16 nm TiO₂ experiments are 6.2 and 2.8 mg/g, respectively. The available surface area for adhesion is the same in these two sets of experiments, but the larger N_{max} for the 26 nm particle experiments may reflect greater aggregation, and hence greater nanoparticle packing on the surface, than occurs for the 16 nm system. Alternatively, the 16 nm particles may aggregate to a greater extent than the 26 nm particles, and increased aggregation could prevent close packing of the aggregates on the mineral surface, leading to decreased adhesion. Previous research has shown that larger TiO₂ nanoparticles formed smaller aggregates than did smaller TiO₂ nanoparticles (Lecoanet et al., 2004; Pettibone et al., 2008; French et al., 2009), and this was also the case for some other metal oxide nanoparticles (He et al., 2008; Darlington et al., 2009). The second explanation is consistent with these observations, but confirmation of this mechanism requires more direct observation of the morphology of the adhered particles. In general, the N_{max} values that were obtained parallel the complex nanoparticle adhesion behaviors that were observed as a function of pH and particle size and that are shown in Figure 3.8 and Figure 3.9. Under some conditions, there was a clear trend with pH and/or particle size, and under other conditions there was not. The N_{max} values for the experiments involving uncoated silica grains were similar to corresponding N_{max} values

for the experiments involving Fe-coated silica grains, conducted at the same pH and particle size conditions.

K_L or K_d values are defined by the slope of the data at low nanoparticle concentrations and represent the distribution of nanoparticles between aqueous suspension and the mineral surface under these conditions. The K values ranged from 6.6×10^{-3} to 3.4×10^{-1} L/g, and while there was no consistent trend with pH or particle size, some generalizations can be made. As can be seen in Figure 3.11, the K values for the 26 and 16 nm TiO_2 were virtually identical to each other across the pH range studied, but the 50 nm particles exhibited markedly different behavior from the two smaller nanoparticle sizes at pH 3 and 5. From pH 6-8, the K values for all three nanoparticle sizes were similar, and there was little change with pH. The values for Fe-coated silica grains were also similar to those calculated for the uncoated silica grains in this pH range. K values represent the distribution of nanoparticles, normalized per gram of sorbent and per liter of suspension. For the experimental sorbent concentrations and suspension volumes, the K values for systems in which 10%, 50%, or 90% of the particles are adhered to the sorbent are 2.2×10^{-3} L/g, 2.1×10^{-2} L/g, and 1.9×10^{-1} L/g, respectively (each distribution is labeled on Figure 3.11). The calculated K values reflect the wide range of partitioning behavior that were observed under the experimental conditions. The K values for the pH 6-8 experiments indicated nearly equal partitioning of the nanoparticles between the suspension and the sorbent surfaces. Some of the experiments yielded K values between the 10% and 50% Adhered lines, while most of the others were between the 50% and 90% Adhered lines. All experimental K values were below the 95% Adhered value of 4.0×10^{-1} L/g. Although Langmuir and K_d modeling parameters are difficult to

extrapolate to realistic conditions (e.g., Koretsky, 2000), the values calculated here suggest that a wide range of partitioning behaviors are possible in the environment.

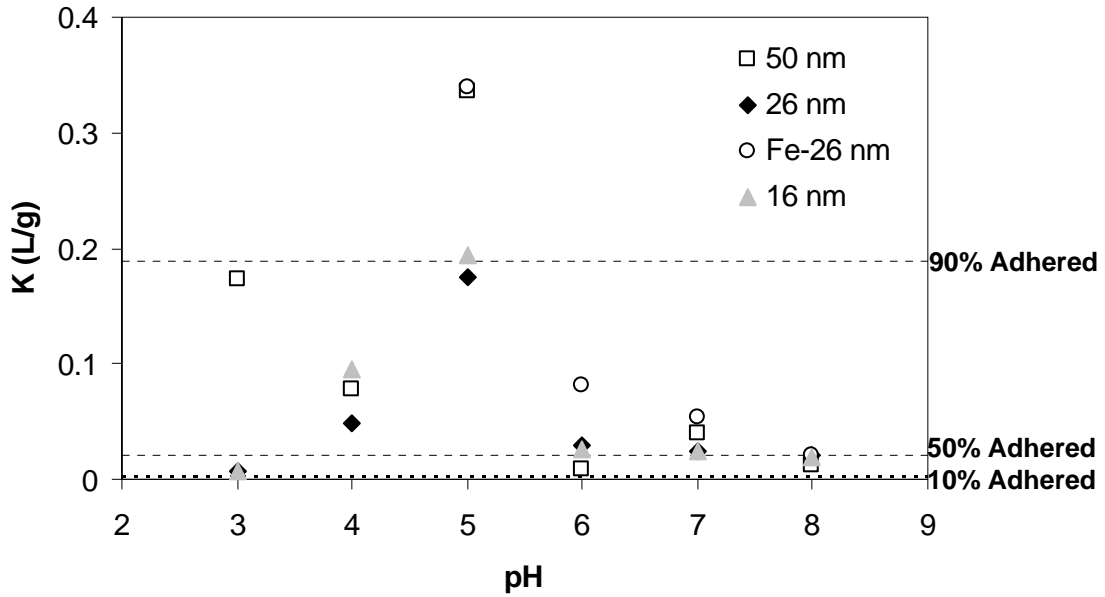


Figure 3.11: K (either K_L or K_d ; see Table 3.1) values as a function of pH from experimental measurements involving all three nanoparticle sizes and the uncoated silica grains, and from experiments involving the 26 nm nanoparticles and the Fe-coated silica grains. The dashed lines represent K values for various nanoparticle distributions between suspension and adhesion.

3.4. Conclusions

Because nanoparticle aggregation and adhesion processes occur simultaneously, it can be difficult to distinguish between the effects of adhesion and aggregate straining in the results of nanoparticle transport experiments. Batch experiments were used to isolate

some of the parameters that influence nanoparticle adhesion. The results indicate that both pH and nanoparticle size exert strong, but complex, effects on the adhesion behavior of TiO₂ nanoparticles onto uncoated silica grains. Below the expected p*H*_{zpc} of 6, TiO₂ nanoparticle adhesion increased with increasing particle size and pH; at and above pH 6, adhesion was pH independent with increasing pH, and nanoparticle size had a minimal influence on adhesion. The UV/visible light absorbance profiles from the experiments also suggest that preferential adhesion of the larger TiO₂ within a given size fraction occurred onto the silica grains below pH 6, and preferential adhesion of the smaller TiO₂ occurred at and above pH 6. The uncoated and Fe-coated silica grain surfaces exhibited similar affinities to adhere the nanoparticles, despite significant differences in surface charge properties of the sorbents. This similarity in adhesion suggests that factors related to the nanoparticles themselves, rather than to the characteristics of the geosorbents, govern the adhesion of TiO₂ nanoparticles under the conditions of these experiments. Because of the predominance of aggregation and the changes in aggregation that are known to occur with changes in pH, it seems likely that aggregation plays a significant role in controlling adhesion behavior.

CHAPTER 4:
PROTON BINDING OF BACTERIAL EXUDATES DETERMINED THROUGH
POTENTIOMETRIC TITRATIONS

4.1. Introduction

Bacteria play an important role in many environmental processes including adsorption and/or reduction of metals (e.g., Beveridge and Murray, 1976; Lovely, 1993; Brown and Parks, 2001; Newman and Banfield, 2002; Borch et al., 2010); precipitation or dissolution of minerals (e.g., Fortin and Beveridge, 1997; Bennett et al., 2001); and the degradation of natural organic matter and certain anthropogenic contaminants (e.g., Young et al., 2005; Mrozik and Piotrowska-Seget, 2010; Tiquia, 2010). Most of these processes involve the bacterial cell wall and/or bacterial metabolism directly. However, bacteria, through active metabolic processes or through lysis and decay, exude a wide range of organic molecules, and there is growing evidence that these bacterial exudates also can contribute to important geochemical processes. For example, metal reduction can occur in the presence of bacterial exudates, as in the case of Pu(VI) reduction to Pu(V) by *Bacillus subtilis* exudates (Ohnuki et al., 2007) and Au(III) reduction to Au(I) also in the presence of *B. subtilis* exudates (Kenney et al., 2010). In addition, bacterial exudates have been shown to accelerate mineral dissolution rates and to increase the extent of dissolution (Lee and Fein, 2000; Perry et al., 2003; Perry et al., 2005; Pokrovsky et al., 2009). The exudates in these studies are dissolved organic molecules

exuded from whole cells and are not the same as the non-aqueous extracellular polymeric substances which are often produced by bacteria and are an important component of biofilms. The observed effects of the bacterial exudates suggest that they contain proton-active organic acid functional groups as these are the most likely means of interacting with metals and mineral surfaces.

Despite the indications that bacterial exudates can affect geochemical processes, there has been virtually no work conducted to quantify their environmental concentrations or characteristics. The objective of this study is to use FTIR spectrometry to provide an initial qualitative description of the exudate molecules and to use potentiometric titrations to determine if the molecules contain proton binding sites and to characterize the acidity constants and the concentrations of those sites. We studied the exudates from a Gram-positive and a Gram-negative bacterial species to better understand how the differences in cell wall characteristics may influence the properties of bacterial exudates, and we examined the exudates produced at different bacterial concentrations and ionic strengths in order to determine the effects of changing solution chemistry on the production of bacterial exudates and to better constrain our thermodynamic modeling. The results represent a framework for understanding the effects of bacterial exudates on geochemical processes and provide a basis for quantitative modeling of metal interactions with the proton-active sites within the exudates. We use the results to compare the proton binding behavior of bacterial exudates with that of bacterial cells.

4.2. Materials and Methods

4.2.1. Experimental

4.2.1.1. *Bacterial Growth and Exudate Preparation*

The bacterial species used in these experiments were the aerobic, Gram-positive soil bacterium *Bacillus subtilis* and the facultatively anaerobic, Gram-negative bacterium *Shewanella oneidensis* MR-1, originally collected from lake sediment. The cell wall constituents and reactivity of *B. subtilis* (Beveridge and Murray, 1980; Fein et al., 2005) and *S. oneidensis* (Venkateswaran et al., 1999; Ha et al., 2010; Mishra et al., 2010) have been well characterized. *B. subtilis* and *S. oneidensis* were initially grown aerobically in 3 mL of trypticase soy broth (TSB) spiked with 0.5% yeast extract (YE) at 32°C with shaking for 24 hours. Bacteria were then transferred to 2 L of the TSB/YE solution to grow under the same conditions and harvested after 24 hours once reaching the stationary growth phase. The washing procedure consisted of centrifugation at 8500 rpm, followed by resuspension of the cells in a NaClO₄ solution of the desired ionic strength (0.01, 0.1, or 0.3 M), repeated five times. The bacteria were then suspended in NaClO₄ of the same ionic strength with which they were washed at a concentration of approximately 40, 80, or 100 g/L bacteria (wet mass). Each bacterial suspension was adjusted to pH 5.5 using aliquots of 6 M HNO₃ and rotated for 2.5 hours, with pH readjusted every 30 minutes. After rotating for 2.5 hours, the bacterial suspension was centrifuged at 10,000 rpm for 10-20 minutes to remove the bacterial cells. The supernatant or 'exudate' solution was decanted and used to conduct potentiometric titrations. A portion of the exudate solution was also diluted for measurements of the total organic carbon concentration ([TOC])

(Shimadzu TOC-V), and the remaining solution was frozen and then freeze dried for FTIR analysis (Bruker Tensor 27 with Platinum ATR). FTIR spectra were baseline corrected and normalized to the height of the 1090-1062 cm^{-1} peak to account for variations in the strength of the absorbance of each sample.

4.2.1.2. *Potentiometric Titrations*

Potentiometric titrations were conducted on the exudate solutions with a Radiometer Analytical ABU91 titrator. The automated burette assembly added aliquots of 1.041 N HCl or 1.030 N NaOH (Sigma-Aldrich; St. Louis, MO) with a potentiometric stability of 0.01 mV/s required between additions. Each exudate solution was first acidified to pH 2.5. A forward or ‘up-pH’ titration was then conducted by basifying to pH 10, and the pH and volume of base added were recorded at each step. Similarly, a reverse or ‘down-pH’ titration was conducted for each solution by acidifying back to pH 2.5, again recording pH and volume of acid added at each step. Four NIST-standard pH buffer solutions (pH 1.68, 4.01, 7.00, and 10.00) were used to calibrate the change measured by the electrode after each acid or base addition (in mV) to pH units. Prior to each titration, the exudate solution was purged with N_2 gas for at least 30 minutes to remove dissolved CO_2 , and titrations were conducted in a closed polypropylene titration vessel into which N_2 gas was continuously supplied to the headspace to further exclude atmospheric CO_2 . A small, Teflon-coated magnetic stir bar continuously stirred the solutions throughout the titration. Titrations of a given exudate solution were conducted in duplicate, and each set of conditions (ionic strength, bacterial type, and bacterial concentration) was examined in at least duplicate (i.e., from at least two separate bacterial batches).

In order to compare our exudate titration data with that of data previously collected for bacterial cells, the total concentration of acid added to the system minus the total concentration of base added ($C_a - C_b$) in moles per L was normalized by dividing by the concentration of bacteria that was used (in g of bacteria, wet mass, per L solution) to generate the exudate solution in question. The total buffering capacity of each exudate solution (in moles per g bacteria) over the pH range of 3 to 9 was also calculated from the titration data for comparison purposes by subtracting $(C_a - C_b)/g/L$ bacteria at pH 9 from $(C_a - C_b)/g/L$ bacteria at pH 3. The uncertainties associated with the calculated buffering capacities that we report are 1σ errors calculated from forward and reverse replicate titrations collected under the same experimental conditions.

4.2.2. Chemical Equilibrium Modeling

Chemical equilibrium modeling was conducted using FITEQL 2.0 (Westall, 1982) with a discrete site model of the reactivity of the bacterial exudate functional groups. Potentiometric titration experiments are essentially proton adsorption measurements, but they are conducted in systems in which it is impossible to keep track of the total absolute concentration of H as one might do with a bulk metal adsorption experiment (Westall et al., 1995; Fein et al., 2005). Therefore, instead of constraining the calculations using a mass balance on the total absolute H concentration, modeling of potentiometric titration data uses a mass balance on the excess/deficit of protons associated with the titrated molecules relative to an arbitrarily defined zero proton condition. In this study, in parallel with potentiometric titration experiments involving bacterial suspensions (e.g., Fein et al., 2005), we define the zero proton condition as that

at which the binding sites on the bacterial exudates are fully protonated. We model the proton buffering behavior of the exudate molecules as simple organic acid functional group sites, where the deficit of protons is represented as:



where L_i represents a proton-active functional group type, and R represents the exudate molecule to which the functional groups are attached. The equilibrium constant for Reaction (4.1), termed the acidity constant, is expressed as:

$$K_{a(i)} = \frac{a_{\text{R-L}_i^-} a_{\text{H}^+}}{a_{\text{R-L}_i\text{H}^0}} \quad (4.2)$$

where a represents the activity of the subscripted component in solution, and activity coefficients of neutral species are assumed to be 1. Equilibrium constants for the dissociation of water and sodium hydroxide were obtained from Martell and Smith (2001). Activity coefficients for ionic aqueous species were calculated using the Davies equation within FITEQL (Westall, 1982).

The potentiometric titration data were used to solve for the $\text{pK}_{a(i)}$ values, as well as for the concentrations of each site type, i . The calculated site concentrations were normalized to the initial bacterial concentration in g per L used to generate each exudate solution, and for comparison purposes, the total site concentration was calculated for each dataset and averaged for each experimental condition. Models with 1 to 5 discrete proton binding site types were tested for their fits to the model data. The goodness-of-fit of each model for each titration dataset was determined based upon the calculated variance parameter, $V(Y)$, as calculated by the FITEQL program. A $V(Y)$ value of 1 indicates a perfect fit, with values much greater than 1 indicating an inappropriate model and values

much less than 1 indicating a model with too many adjustable parameters; values from 0 to 20 can be considered good fits (Westall, 1982).

4.3. Results and Discussion

4.3.1. Exudate Solutions

After the bacteria were removed from their electrolyte soaking solutions via centrifugation, the remaining supernatant contained bacterial material from the cell surface and/or material from the cell cytoplasm which entered solution as a result of cell lysis or passive excretion. These organic molecules are referred to here collectively as ‘exudates’ with no effort made to differentiate them as all of these types of molecules are likely to be present in natural systems. *B. subtilis* exudate solutions were clear and colorless; *S. oneidensis* exudate solutions were also clear but with a reddish-orange color, which darkened with increasing initial bacteria concentration. During purging with N₂ gas, *B. subtilis* solutions became much frothier than *S. oneidensis* solutions. These differences could result from differences in composition as well as differences in the concentration of material in solution. Changes in the total organic carbon concentration [TOC] of the exudate solutions under the range of experimental conditions are shown in Figure 4.1. Compared to *B. subtilis* exudate solutions, *S. oneidensis* solutions were lower in [TOC] (by at least half) under all conditions, and [TOC] values increased with increasing initial bacterial concentration. There does not appear to be a significant [TOC] dependence on ionic strength. Qualitatively, the FTIR spectra of the freeze-dried exudate solutions (Figure 4.2) were similar for both bacterial types. The same major peaks were

present in samples of exudate solutions from both bacterial species, and although there are some differences as a function of ionic strength, there is no consistent ionic strength dependence and the position of the peaks does not vary significantly as a function of ionic strength or initial bacterial concentration.

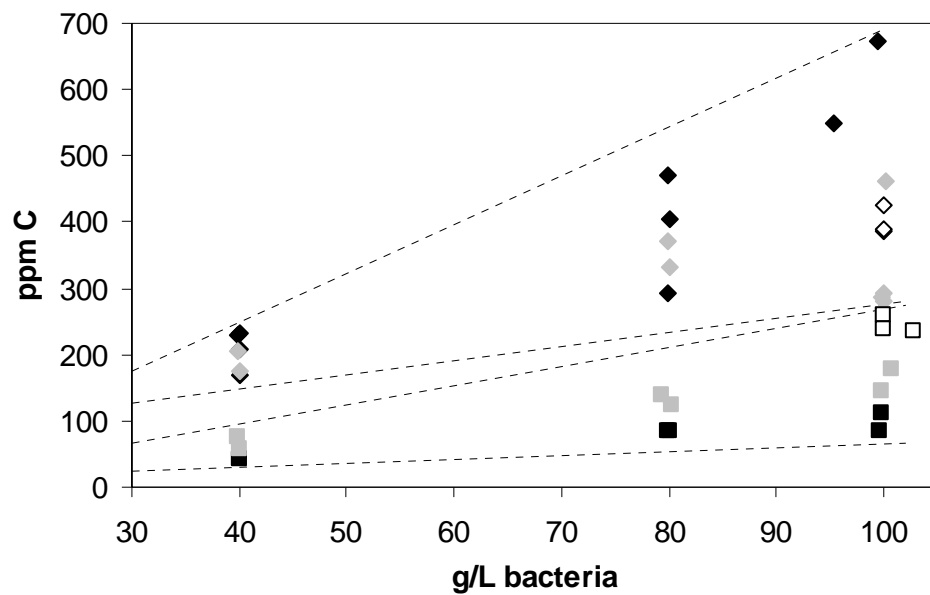


Figure 4.1 Measured [TOC] (ppm C) as a function of the initial *B. subtilis* (diamonds) or *S. oneidensis* (squares) concentration at 0.01 M (black), 0.1 M (gray), or 0.3 M (white) NaClO₄. The dashed lines separate the field for the *B. subtilis* data (top) from the field for the *S. oneidensis* data (bottom).

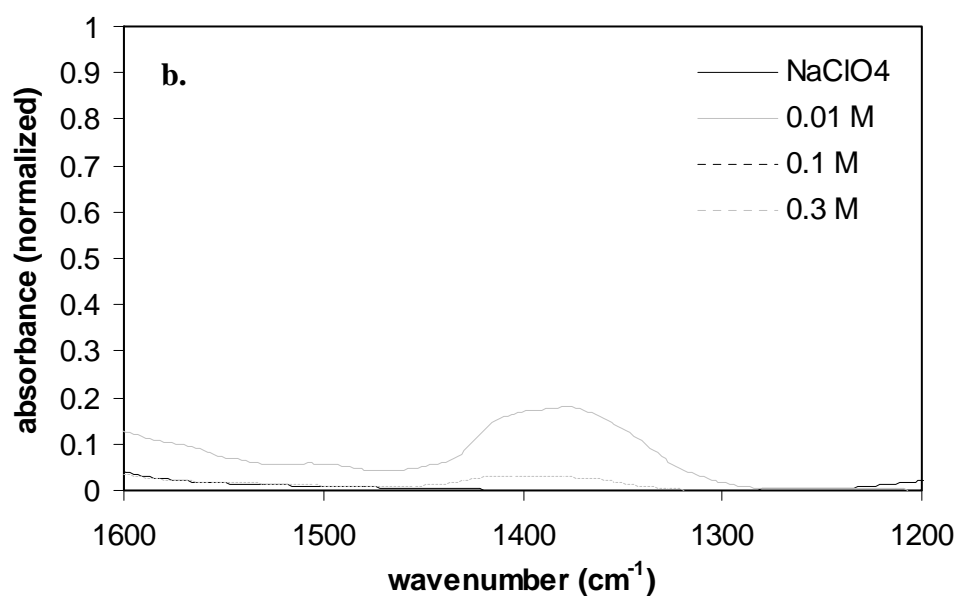
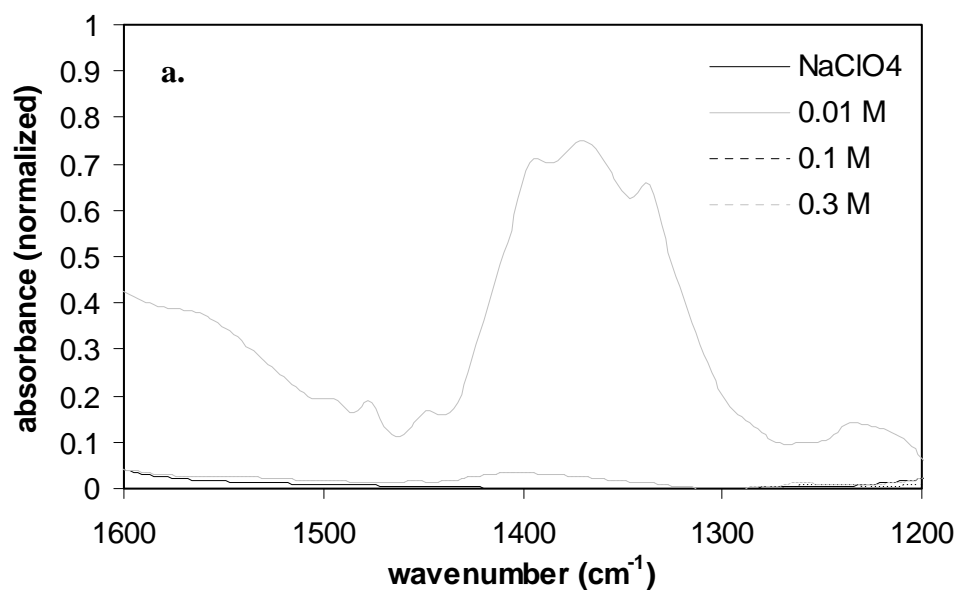


Figure 4.2 FTIR spectra of a) *B. subtilis* and b) *S. oneidensis* 100 g/L exudate solutions. The black line is pure NaClO₄ and the exudates made in 0.01 M, 0.1 M, and 0.3 M NaClO₄ are represented by the gray, black dashed, and gray dashed lines, respectively.

4.3.2. Exudate Titrations

Forward and reverse titrations of both *B. subtilis* and *S. oneidensis* exudate solutions (Figure 4.4 and Figure 4.6) showed full reversibility of the proton binding reactions on the timescale of the experiments. Experimental replicates from the same exudate solution, as well as from exudate solutions made at the same conditions but from a different bacterial batch, also generally showed good agreement (data not shown). The bacterial exudates exhibited a significant buffering capacity over the pH range examined in this study (2.5-10). In order to compare the buffering capacity of bacterial exudates to that typically exhibited by bacterial cells, the total buffering capacity of the exudate solutions from pH 3-9 was averaged for each combination of bacterial type, bacterial concentration, and ionic strength and compared to the total buffering capacity over the same pH range from potentiometric titrations performed previously on *B. subtilis* (Fein et al., 2005) and *S. oneidensis* (Mishra et al., 2010) bacterial cell suspensions (Table 4.1). This comparison is meaningful because the buffering capacity of the exudate solutions was normalized to the mass of bacteria used to generate those solutions, so the comparison relates the buffering capacity of a cell suspension to the buffering capacity of the exudate solution generated by that same concentration of cells.

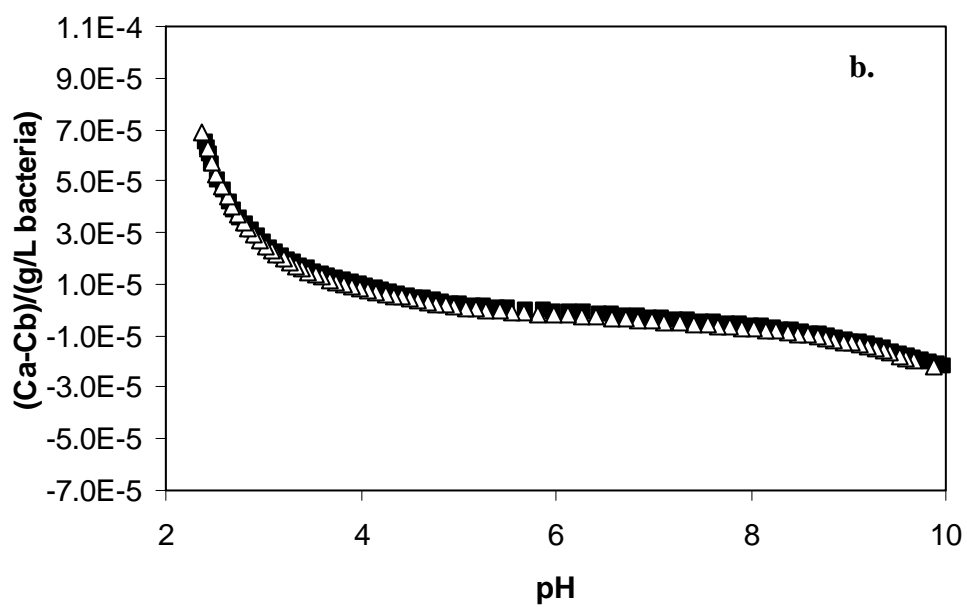
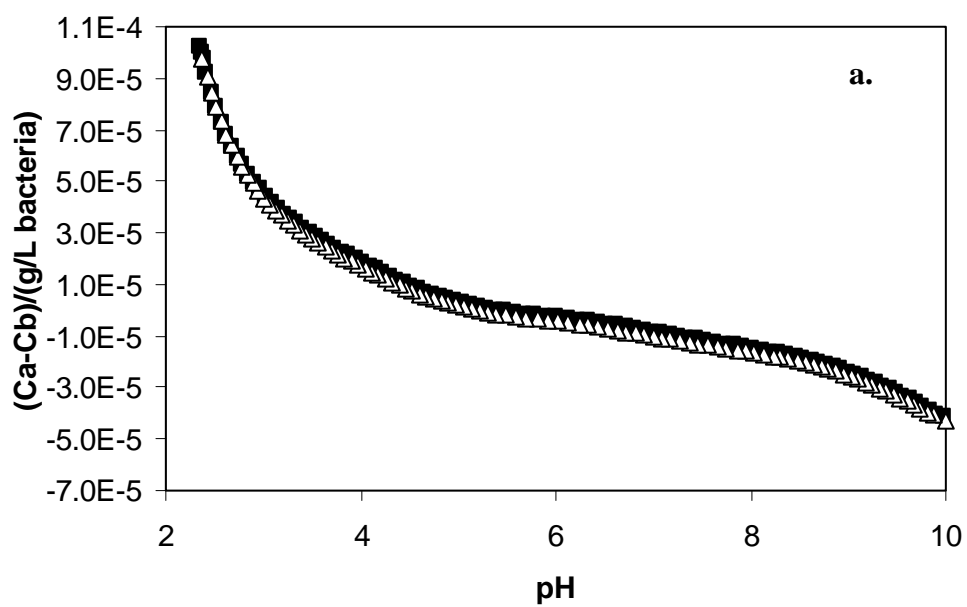


Figure 4.3 Representative examples of forward (black squares) and reverse (white triangles) potentiometric titration data from exudate solutions made using 100 g/L *B. subtilis* (normalized per g/L bacteria) and a) 0.01 M, b) 0.1 M, or c) 0.3 M NaClO₄ (p. 73-p. 74).

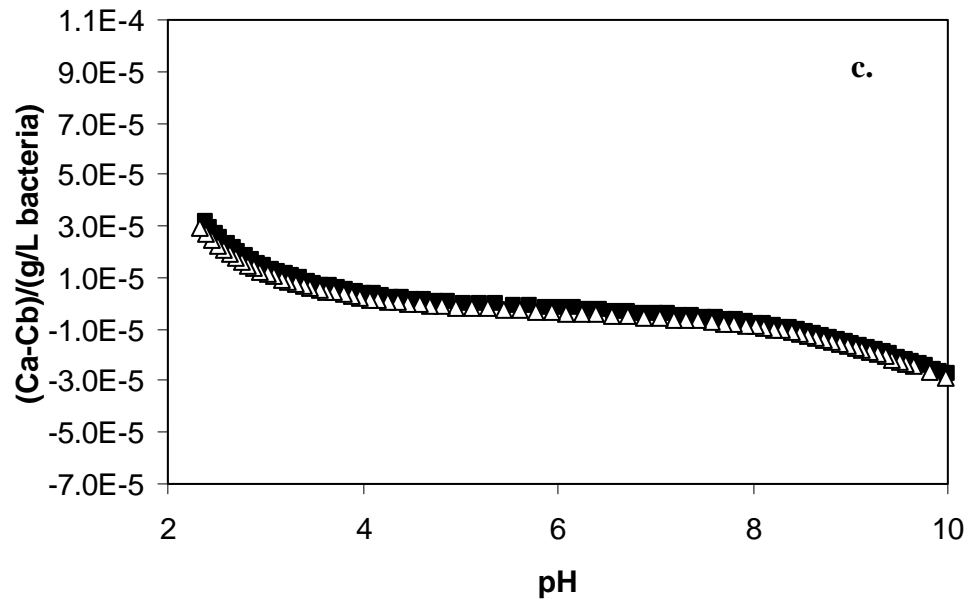


Figure 4.4 Representative examples of forward (black squares) and reverse (white triangles) potentiometric titration data from exudate solutions made using 100 g/L *B. subtilis* (normalized per g/L bacteria) and a) 0.01 M, b) 0.1 M, or c) 0.3 M NaClO₄ (p. 73-p. 74).

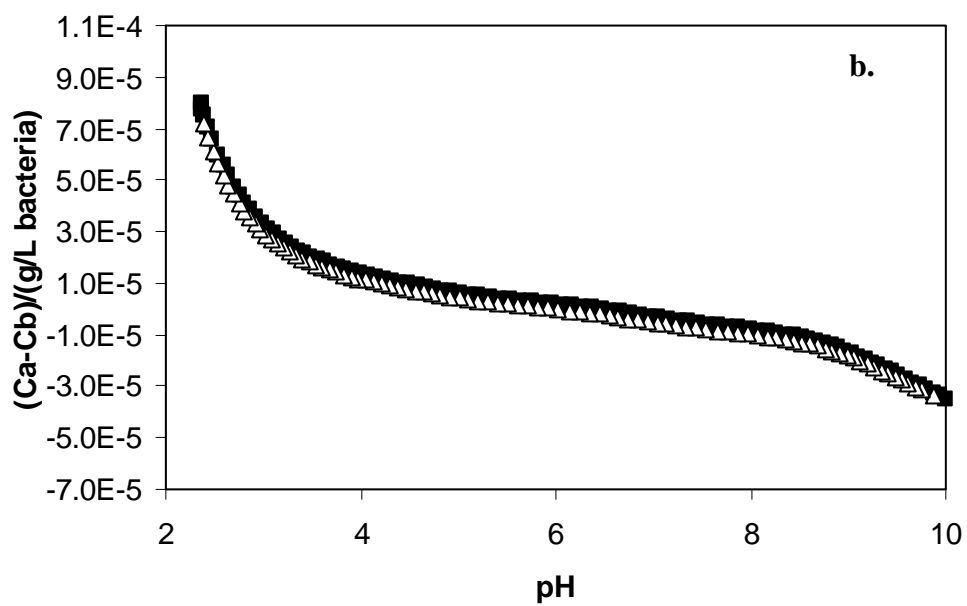
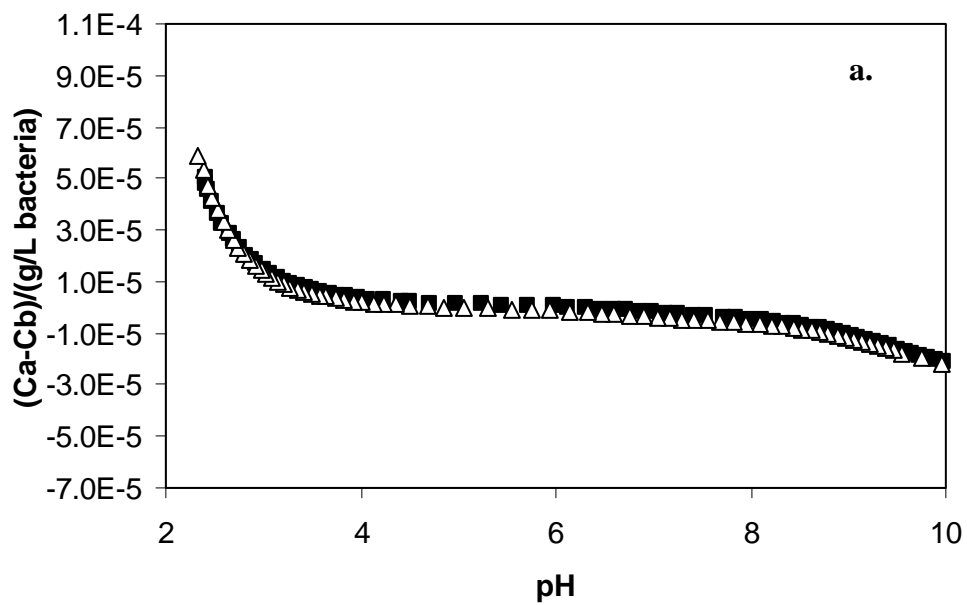


Figure 4.5 Representative examples of forward (black squares) and reverse (white triangles) potentiometric titration data from exudate solutions made using 100 g/L *S. oneidensis* (normalized per g/L bacteria) and a) 0.01 M, b) 0.1 M, or c) 0.3 M $NaClO_4$ (p. 75-p. 76).

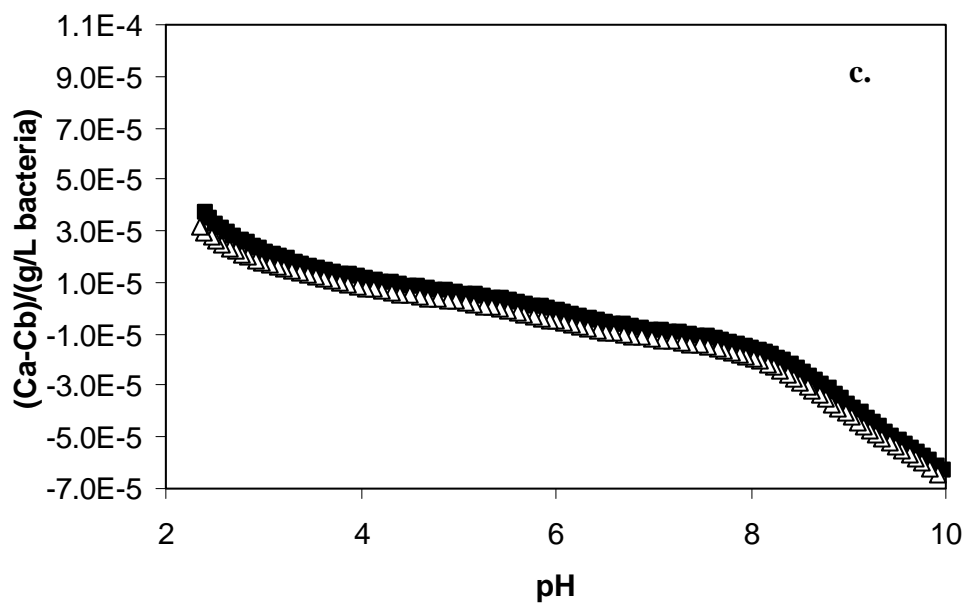


Figure 4.6 Representative examples of forward (black squares) and reverse (white triangles) potentiometric titration data from exudate solutions made using 100 g/L *S. oneidensis* (normalized per g/L bacteria) and a) 0.01 M, b) 0.1 M, or c) 0.3 M NaClO₄ (p. 75-p. 76).

TABLE 4.1

TOTAL BUFFERING CAPACITY (MOL/G) OF BACTERIAL EXUDATES AND BACTERIAL CELLS, CALCULATED FOR THE PH RANGE OF 3 TO 9.

Bacterial exudates^a	
<i>B. subtilis</i>	Total buffering capacity
0.01 M, 40 g/L	$7.8 \times 10^{-5} \pm 4.6 \times 10^{-6}$
0.01 M, 80 g/L	$5.6 \times 10^{-5} \pm 1.1 \times 10^{-5}$
0.01 M, 100 g/L	$7.2 \times 10^{-5} \pm 6.0 \times 10^{-6}$
0.1 M, 40 g/L	$6.0 \times 10^{-5} \pm 3.2 \times 10^{-6}$
0.1 M, 80 g/L	$4.4 \times 10^{-5} \pm 2.6 \times 10^{-6}$
0.1 M, 100 g/L	$3.9 \times 10^{-5} \pm 4.2 \times 10^{-6}$
0.3 M, 100 g/L	$2.8 \times 10^{-5} \pm 2.4 \times 10^{-6}$
<i>S. oneidensis</i>	
0.01 M, 40 g/L	$4.6 \times 10^{-5} \pm 1.6 \times 10^{-6}$
0.01 M, 80 g/L	$3.2 \times 10^{-5} \pm 1.9 \times 10^{-6}$
0.01 M, 100 g/L	$3.0 \times 10^{-5} \pm 4.6 \times 10^{-6}$
0.1 M, 40 g/L	$6.0 \times 10^{-5} \pm 3.9 \times 10^{-6}$
0.1 M, 80 g/L	$4.8 \times 10^{-5} \pm 3.5 \times 10^{-6}$
0.1 M, 100 g/L	$4.4 \times 10^{-5} \pm 5.0 \times 10^{-6}$
0.3 M, 100 g/L	$6.0 \times 10^{-5} \pm 4.5 \times 10^{-6}$
Bacterial cells	
<i>B. subtilis</i>^b	Total buffering capacity
0.01 M, 75-150 g/L	1.6×10^{-4}
0.1 M, 75-150 g/L	2.8×10^{-4}
0.3 M, 75-150 g/L	2.3×10^{-4}
<i>S. oneidensis</i>^c	
0.1 M, 50 g/L	3.1×10^{-4}

Note: ^aThis paper; ^bFein et al., 2005; ^cMishra et al., 2010

The mass normalized buffering capacities of the exudate solutions in this study were fairly close to one another, ranging from $2.8\text{-}7.8 \times 10^{-5}$ mol/g (Table 4.1). The exudate buffering capacities were approximately an order of magnitude lower than those exhibited by *B. subtilis* ($1.6\text{-}2.8 \times 10^{-4}$ mol/g) and *S. oneidensis* (3.1×10^{-4} mol/g), as well as the wide range of bacteria compared by Borrok et al. (2005). The buffering capacities of the exudate solutions made from different bacterial concentrations at a given ionic strength showed a slight decrease with increasing bacterial concentration in most cases (e.g., the total buffering capacity of the *B. subtilis* exudate decreased from $6.0 \times 10^{-5} \pm 3.2 \times 10^{-6}$ mol/g at 40 g/L to $3.9 \times 10^{-5} \pm 4.2 \times 10^{-6}$ mol/g at 100 g/L, and the *S. oneidensis* exudate capacity decreased from $6.0 \times 10^{-5} \pm 3.9 \times 10^{-6}$ mol/g at 40 g/L to $4.4 \times 10^{-5} \pm 5.0 \times 10^{-6}$ mol/g at 100 g/L).

There were also significant changes in buffering capacity with increasing ionic strength, although the effects varied from one species to the other. The total buffering capacity of the *B. subtilis* exudates decreased with increasing ionic strength (e.g., from $7.2 \times 10^{-5} \pm 6.0 \times 10^{-6}$ mol/g at 0.01 M to $3.9 \times 10^{-5} \pm 4.2 \times 10^{-6}$ mol/g at 0.1 M to $2.8 \times 10^{-5} \pm 2.4 \times 10^{-6}$ mol/g at 0.3 M in the 100 g/L exudate solutions). The reverse was true for the *S. oneidensis* exudates with total buffering capacity increasing significantly with increasing ionic strength (e.g., from $3.0 \times 10^{-5} \pm 4.6 \times 10^{-6}$ mol/g at 0.01 M to $4.4 \times 10^{-5} \pm 5.0 \times 10^{-6}$ mol/g at 0.1 M to $6.0 \times 10^{-5} \pm 4.5 \times 10^{-6}$ mol/g at 0.3 M in the 100 g/L exudate solutions). However, the buffering capacities for *B. subtilis* and *S. oneidensis* exudates covered essentially the same range, and total buffering capacity at 0.1 M was similar for the exudates from both bacterial species. In titrations conducted with whole but non-metabolizing *B. subtilis* bacterial cells (Fein et al., 2005), the effect of changing ionic

strength on total buffering capacity was small relative to the experimental uncertainties. Titrations conducted on cells of the algal species *Pseudokirchneriella subcapitata* in 0.1 M NaClO₄ (Kaulbach et al., 2005) showed a total buffering capacity ($\sim 3.7 \times 10^{-5}$ mol/g) that was within the range calculated for our bacterial exudates.

4.3.3. Titration Modeling

Based upon the calculated $V(Y)$ values, the 1- and 2-site models were deemed inappropriate with average $V(Y)$ values of 590 and 73, respectively. Similarly, the 4-site model showed no significant improvement in fit over the 3-site model and would not converge under some experimental conditions, and the 5-site model failed to converge in all cases. Thus, the 3-site model (average $V(Y)$ of 6.5) was determined to be the most appropriate under all experimental conditions (e.g., Figure 4.7). The calculated $pK_{a(i)}$ values (negative $\log K_{a(i)}$ values for Reaction 4.2) and site concentrations for the forward titrations do not vary significantly from the corresponding values calculated for the reverse titrations within 1σ error. Table 4.2 shows a representative example of the relationship between the calculated values from the forward and reverse titrations for all replicates of a single experimental condition (100 g/L *B. subtilis* exudate in 0.1 M NaClO₄), and Tables C1 and C2 provide full comparisons of forward and reverse averages. Thus, the protonation reactions are fully reversible on the timescale of these experiments, and both the forward and reverse titrations reflect equilibrium conditions. Because of the lack of systematic difference between the forward and reverse titrations, we combine the results of both forward and reverse titrations from all replicates of each

experimental condition to calculate average modeling parameters and their corresponding 1σ errors (Figure 4.8, Figure 4.10, and Figure 4.12; Tables C1 and C2).

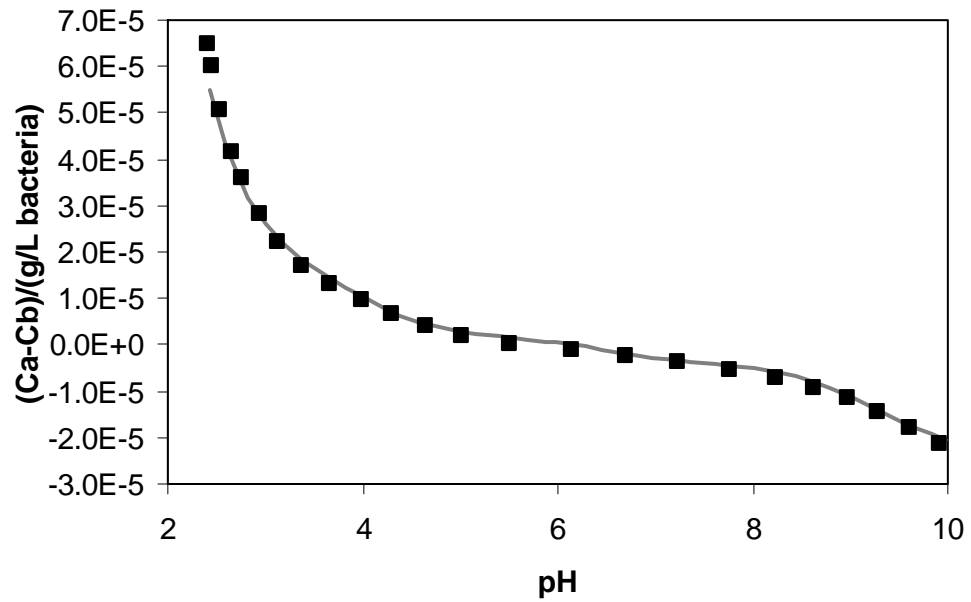


Figure 4.7 Representative fit of a 3-site model (gray curve) to the potentiometric titration data (squares) for the exudate solution made using 100 g/L *B. subtilis* in 0.1 M NaClO₄. Some titration data points have been removed for visualization purposes.

TABLE 4.2

CALCULATED $pK_{a(i)}$ VALUES AND SITE CONCENTRATIONS (MOL/G) FROM
 THE 3-SITE MODEL USING FORWARD AND REVERSE DATA FROM
 POTENTIOMETRIC TITRATIONS ON EXUDATE SOLUTIONS MADE WITH 100
 G/L *B. SUBTILIS* IN 0.1 M NaClO_4 .

Exudate titration	$pK_{a(1)}$	[site 1]	$pK_{a(2)}$	[site 2]	$pK_{a(3)}$	[site 3]	V(Y)
Forward 1a	4.01	1.42×10^{-5}	6.53	4.57×10^{-6}	9.18	1.54×10^{-5}	6.81
Forward 1b	4.04	1.38×10^{-5}	6.69	4.80×10^{-6}	9.23	1.51×10^{-5}	5.97
Forward 2a	3.97	1.61×10^{-5}	6.49	5.11×10^{-6}	9.23	1.62×10^{-5}	8.40
Forward 2b	4.01	1.57×10^{-5}	6.59	5.15×10^{-6}	9.28	1.60×10^{-5}	7.78
Forward 3a	4.05	1.59×10^{-5}	6.63	5.75×10^{-6}	9.27	1.74×10^{-5}	8.06
Forward 3b	4.08	1.54×10^{-5}	6.58	5.78×10^{-6}	9.27	1.78×10^{-5}	7.70
Forward 4a	3.80	2.14×10^{-5}	6.31	6.87×10^{-6}	9.07	2.02×10^{-5}	9.98
Forward 4b	3.86	2.10×10^{-5}	6.49	6.81×10^{-6}	9.13	2.04×10^{-5}	8.08
Forward average	3.98 \pm 0.10	1.67×10^{-5} \pm 2.91×10^{-6}	6.54 \pm 0.12	5.61×10^{-6} \pm 8.66×10^{-7}	9.21 \pm 0.08	1.73×10^{-5} \pm 2.06×10^{-6}	
Reverse 1a	4.01	1.41×10^{-5}	6.56	4.98×10^{-6}	9.25	1.53×10^{-5}	6.02
Reverse 1b	4.02	1.37×10^{-5}	6.53	4.86×10^{-6}	9.24	1.53×10^{-5}	5.60
Reverse 2a	3.97	1.61×10^{-5}	6.51	5.42×10^{-6}	9.27	1.59×10^{-5}	7.39
Reverse 2b	4.00	1.53×10^{-5}	6.47	5.29×10^{-6}	9.26	1.57×10^{-5}	7.01
Reverse 3a	3.99	1.63×10^{-5}	6.47	6.24×10^{-6}	9.30	1.75×10^{-5}	8.68
Reverse 3b	4.07	1.55×10^{-5}	6.57	6.14×10^{-6}	9.29	1.77×10^{-5}	7.20
Reverse 4a	3.78	2.24×10^{-5}	6.33	7.16×10^{-6}	9.13	2.00×10^{-5}	8.78
Reverse 4b	3.75	2.27×10^{-5}	6.28	7.22×10^{-6}	9.12	2.03×10^{-5}	9.34
Reverse average	3.95 \pm 0.12	1.70×10^{-5} \pm 3.54×10^{-6}	6.46 \pm 0.11	5.91×10^{-6} \pm 9.31×10^{-7}	9.23 \pm 0.07	1.72×10^{-5} \pm 2.04×10^{-6}	
Combined average	3.96 \pm 0.11	1.68×10^{-5} \pm 3.13×10^{-6}	6.50 \pm 0.11	5.76×10^{-6} \pm 8.83×10^{-7}	9.22 \pm 0.07	1.73×10^{-5} \pm 1.98×10^{-6}	

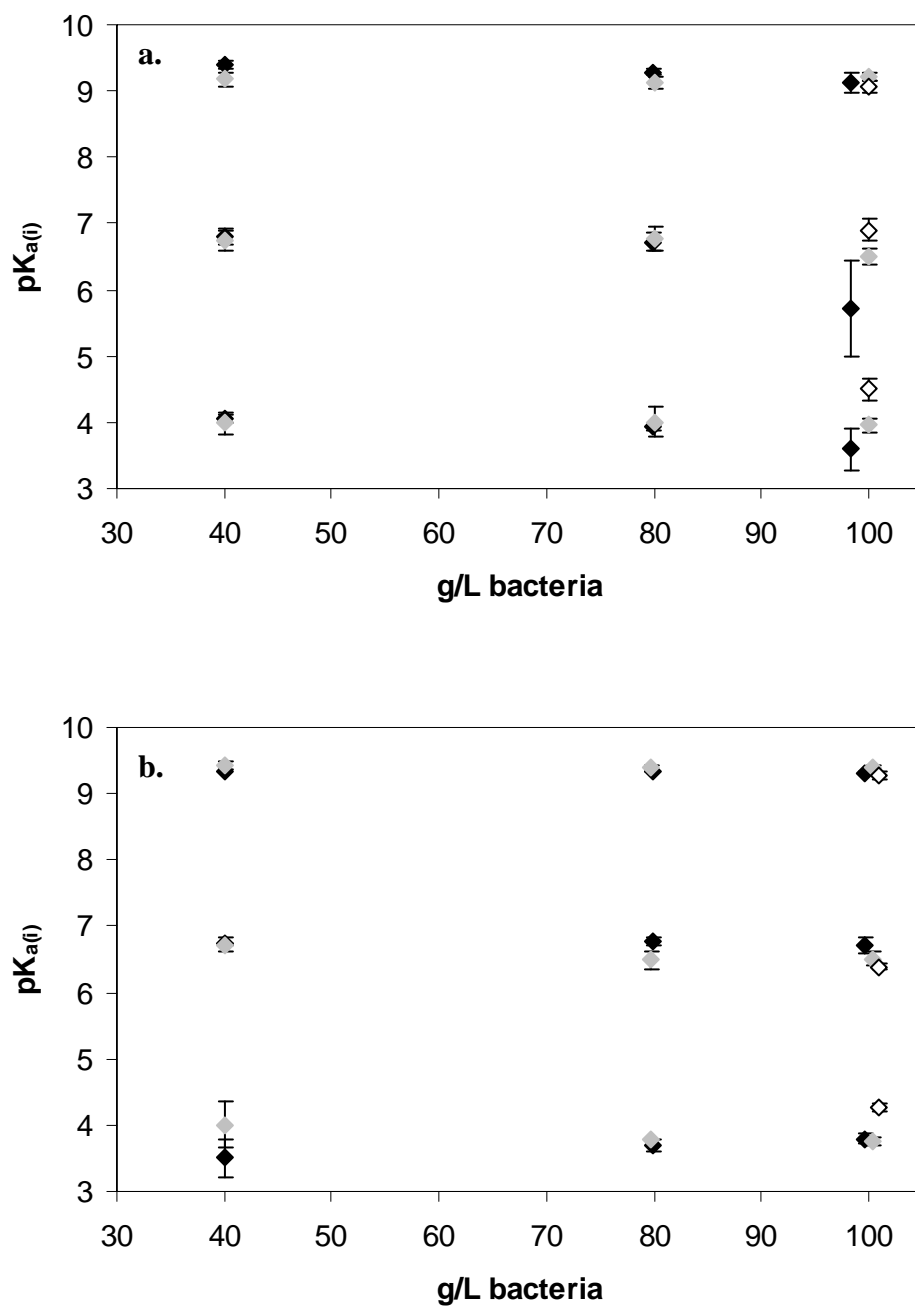


Figure 4.8 Comparison of the calculated $pK_{a(i)}$ values for a) *B. subtilis* and b) *S. oneidensis* exudate solutions made using 40, 80, and 100 g/L bacterial concentrations and 0.01 (black), 0.1 (gray), or 0.3 (white) M NaClO_4 .

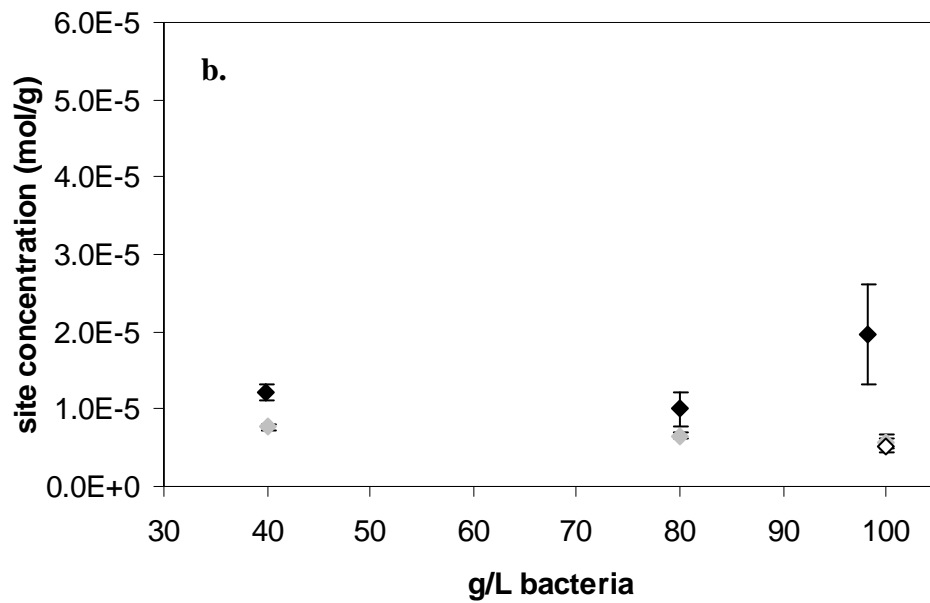
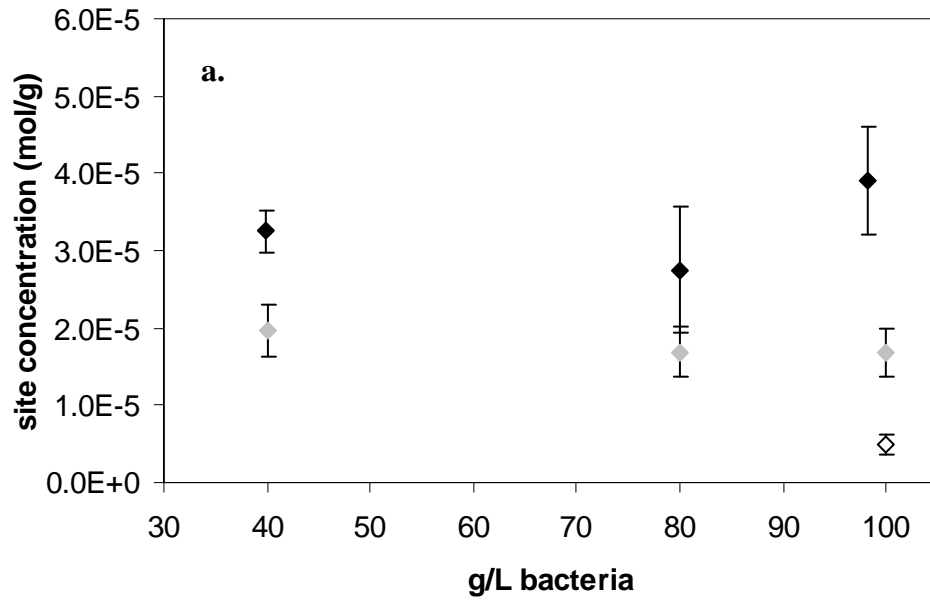


Figure 4.9 Comparison of the calculated site concentrations (moles of site per g bacteria) for *B. subtilis* exudates at a) site 1, b) site 2, c) site 3, and d) total sites from solutions with 40, 80, and 100 g/L initial bacterial concentrations and 0.01 M (black), 0.1 M (gray), or 0.3 M (white) NaClO₄ (p. 83-p. 84).

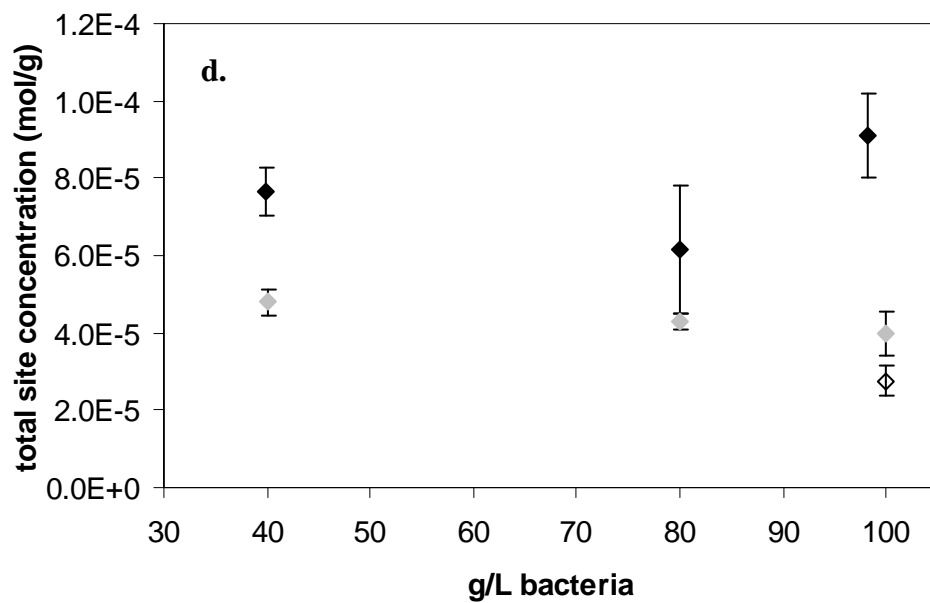
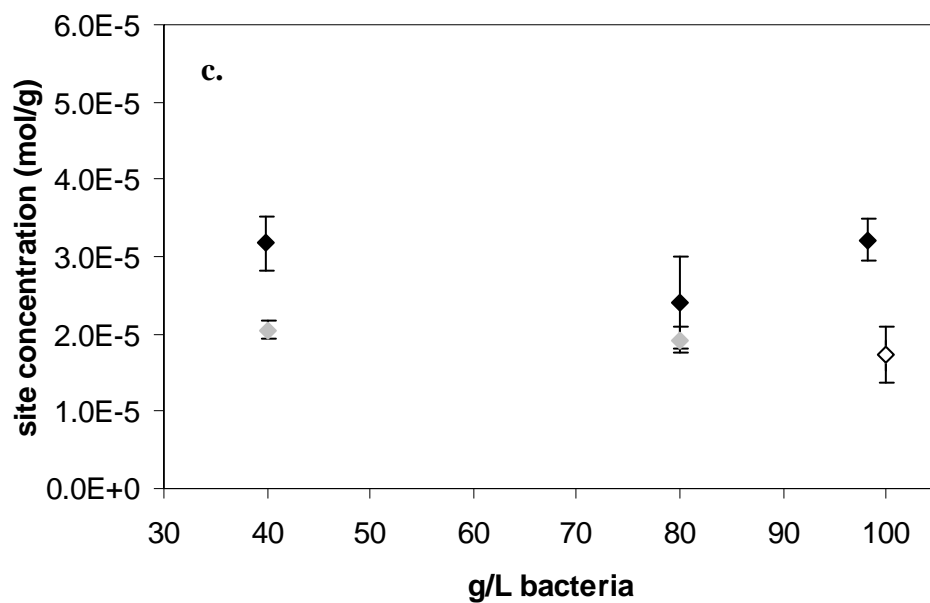


Figure 4.10 Comparison of the calculated site concentrations (moles of site per g bacteria) for *B. subtilis* exudates at a) site 1, b) site 2, c) site 3, and d) total sites from solutions with 40, 80, and 100 g/L initial bacterial concentrations and 0.01 M (black), 0.1 M (gray), or 0.3 M (white) NaClO₄ (p. 83-p. 84).

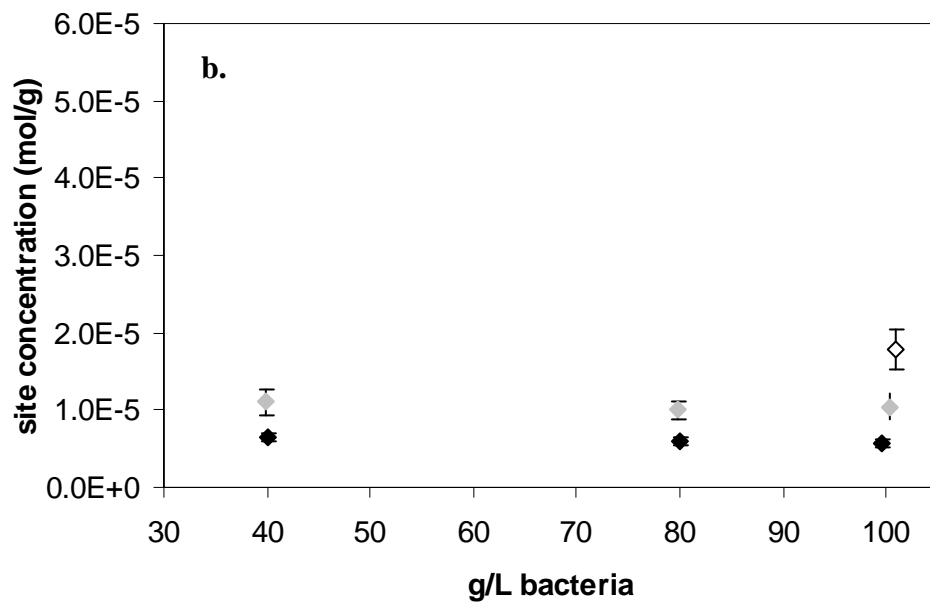
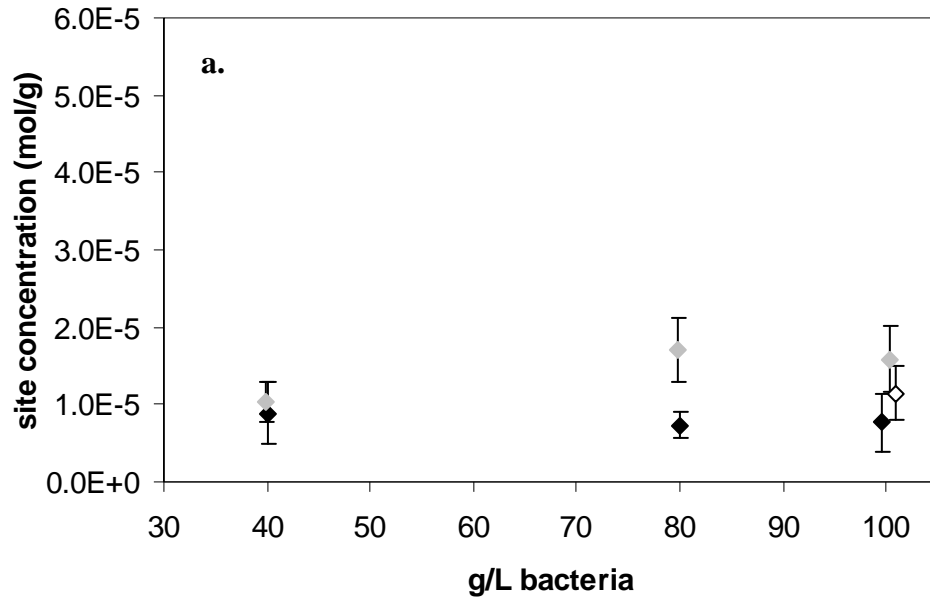


Figure 4.11 Comparison of the calculated site concentrations (moles of site per g bacteria) for *S. oneidensis* exudates at a) site 1, b) site 2, c) site 3, and d) total sites from solutions with 40, 80, and 100 g/L initial bacterial concentrations and 0.01 M (black), 0.1 M (gray), or 0.3 M (white) NaClO₄ (p. 85-p. 86).

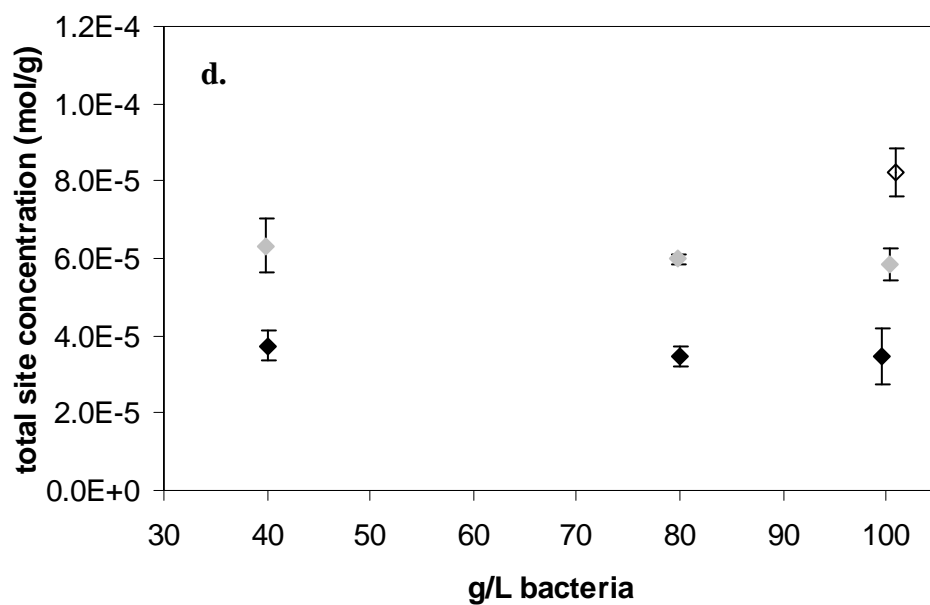
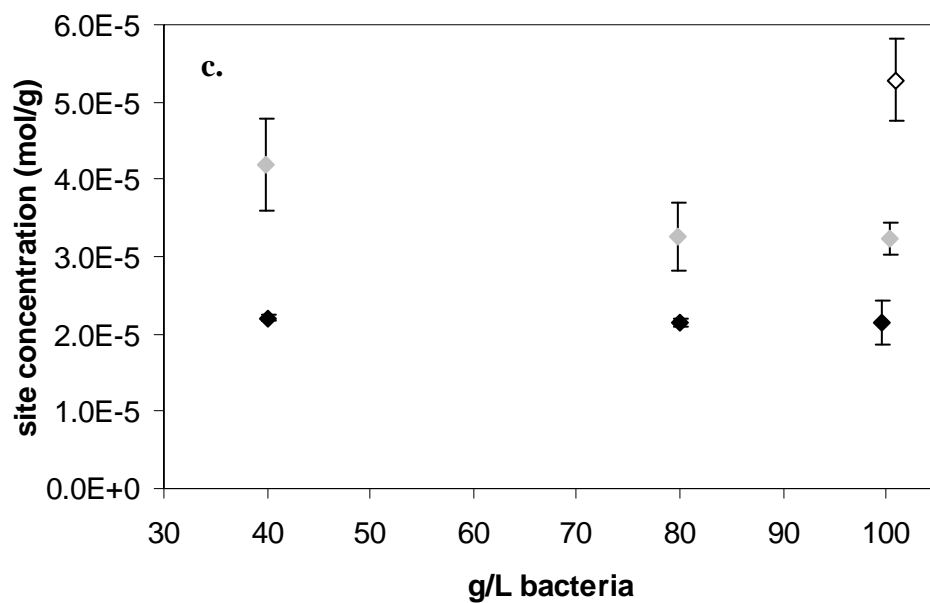


Figure 4.12 Comparison of the calculated site concentrations (moles of site per g bacteria) for *S. oneidensis* exudates at a) site 1, b) site 2, c) site 3, and d) total sites from solutions with 40, 80, and 100 g/L initial bacterial concentrations and 0.01 M (black), 0.1 M (gray), or 0.3 M (white) NaClO₄ (p. 85-p. 86).

The average $pK_{a(i)}$ values and site concentrations for the *B. subtilis* and *S. oneidensis* exudates are all within 1 σ error when compared as a function of the initial bacterial concentration. Increasing the initial bacterial concentration should increase the concentration of exudate in solution without changing its composition; thus, normalizing the site concentrations to the initial bacterial concentration, as was done here, should remove any variability due to the initial bacterial concentration, which does appear to be the case (Figure 4.10 and Figure 4.12).

The average $pK_{a(i)}$ values calculated for the *B. subtilis* and *S. oneidensis* exudate solutions of varying ionic strength (Figure 4.8; Tables C1 and C2) are all within 1 σ error at the three $pK_{a(i)}$ values, except for the 0.3 M solutions at 100 g/L which exhibit slightly, but significantly, different $pK_{a(1)}$ values from those calculated for the 0.01 and 0.1 M exudate solutions (e.g., for *B. subtilis*, $pK_{a(1)}$ is 4.50 ± 0.16 in 0.3 M but 3.88 ± 0.26 and 3.98 ± 0.16 in 0.01 and 0.1 M, respectively; for *S. oneidensis* $pK_{a(1)}$ is 4.27 ± 0.23 in 0.3 M but 3.66 ± 0.21 and 3.85 ± 0.23 in 0.01 and 0.1 M, respectively). However, these differences are only slightly outside the 1 σ error and, as they are still within the 2 σ error, combined averages from the three ionic strengths are still calculated and compared below.

Ionic strength exhibits a greater influence on the calculated site concentrations for the individual and total exudate sites than on the $pK_{a(i)}$ values (Figure 4.10 and Figure 4.12). For the *B. subtilis* exudate solutions, there is a decrease in the calculated site 1 concentrations with increasing ionic strength and only a very slight decrease with increasing ionic strength in the site 2 and 3 concentrations (Figure 4.10a-c). The total site concentrations for the *B. subtilis* exudates decrease with increasing ionic strength from

$7.7 \times 10^{-5} \pm 1.7 \times 10^{-5}$ to $4.3 \times 10^{-5} \pm 5.7 \times 10^{-6}$ to $2.8 \times 10^{-5} \pm 4.0 \times 10^{-6}$ mol/g bacteria (wet weight) at 0.01, 0.1, and 0.3 M NaClO₄, respectively (Figure 4.10d). Conversely, for *S. oneidensis*, the concentrations for sites 2 and 3 increase significantly with increasing ionic strength, with only a very slight increase in the site 1 concentrations (Figure 4.12a-c). The total site concentrations in the *S. oneidensis* exudates increase with increasing ionic strength from $3.6 \times 10^{-5} \pm 4.9 \times 10^{-6}$ to $6.1 \times 10^{-5} \pm 5.0 \times 10^{-6}$ to $8.2 \times 10^{-5} \pm 6.3 \times 10^{-6}$ mol/g bacteria (wet weight) at 0.01, 0.1, and 0.3 M NaClO₄, respectively (Figure 4.12d).

Although, as we summarized above, some significant differences in site concentration exist as a function of ionic strength, the ionic strength dependence is not large for the exudates from either species, and reasonable estimates of proton binding can be attained over the ionic strength conditions, and initial bacterial concentrations, from a single averaged set of pK_{a(i)} and site concentration values for both bacterial species. Table 4.3 lists these overall average values. The *B. subtilis* exudate has average pK_{a(i)} values of 3.98 ± 0.28 , 6.57 ± 0.48 , and 9.22 ± 0.14 , and the *S. oneidensis* exudate has average pK_{a(i)} values of 3.86 ± 0.32 , 6.60 ± 0.19 , and 9.35 ± 0.11 (Table 4.3). Thus, the pK_{a(i)} values for the exudates from the two bacterial species are not significantly different and can be averaged to yield combined pK_{a(i)} values of 3.93 ± 0.30 , 6.58 ± 0.38 , and 9.28 ± 0.14 . As mentioned previously, the exudates from the two bacterial species show opposite trends in their site concentrations with increasing ionic strength; however, their total site concentrations cover a similar range (roughly 2.8 - 8.2×10^{-5} mol/g). Combined average site concentrations for the two bacterial species are $1.85 \times 10^{-5} \pm 1.10 \times 10^{-5}$, $1.01 \times 10^{-5} \pm 5.10 \times 10^{-6}$, and $2.82 \times 10^{-5} \pm 1.10 \times 10^{-5}$ mol/g for sites 1, 2, and 3, respectively.

The usefulness of the overall averaged model depends upon the specific purpose of the modeling: a laboratory-scale study with exudates from a single bacterial species may exhibit proton binding behavior significantly different from the averaged model; however, for modeling the behavior of exudates in an environmental system in which a range of bacterial species exist, the averaged calculated model parameters are likely to yield a reasonable estimation, in the absence of data specifically for the species present in the system.

TABLE 4.3

CALCULATED $\text{pK}_{\text{A(l)}}$ VALUES AND SITE CONCENTRATIONS (MOL/G)
 AVERAGED FOR ALL INITIAL BACTERIAL CONCENTRATIONS AND IONIC
 STRENGTHS FOR *B. SUBTILIS* EXUDATES, *S. ONEIDENSIS* EXUDATES, AND
 THE TWO TYPES OF EXUDATES COMBINED.

	$\text{pK}_{\text{a(1)}}$	[site 1]	$\text{pK}_{\text{a(2)}}$	[site 2]	$\text{pK}_{\text{a(3)}}$	[site 3]	Total sites
<i>B. subtilis</i> exudate	3.98	2.40×10^{-5}	6.57	9.96×10^{-6}	9.22	2.39×10^{-5}	5.79×10^{-5}
	±	±	±	±	±	±	±
<i>S. oneidensis</i> exudate	0.28	1.12×10^{-5}	0.48	5.44×10^{-6}	0.14	7.06×10^{-6}	2.23×10^{-5}
	±	±	±	±	±	±	±
Exudates combined	3.86	1.13×10^{-5}	6.60	1.03×10^{-5}	9.35	3.38×10^{-5}	5.53×10^{-5}
	±	±	±	±	±	±	±
	0.32	4.81×10^{-6}	0.19	4.65×10^{-6}	0.11	1.27×10^{-5}	1.86×10^{-5}
	±	±	±	±	±	±	±
	3.93	1.85×10^{-5}	6.58	1.01×10^{-5}	9.28	2.82×10^{-5}	5.68×10^{-5}
	±	±	±	±	±	±	±
	0.30	1.10×10^{-5}	0.38	5.10×10^{-6}	0.14	1.10×10^{-5}	2.08×10^{-5}
	±	±	±	±	±	±	±

The similarities in calculated $pK_{a(i)}$ values and site concentrations for the exudates of these two bacterial species are interesting given the differences in the cell wall structures of the bacteria that generated the exudates. Gram-positive bacteria, such as *B. subtilis*, have a framework of peptidoglycan shaping the cell wall with teichoic and/or teichuronic acid components joined to the peptidoglycan, whereas Gram-negative bacteria, such as *S. oneidensis*, have a peptidoglycan layer in their periplasm, which is covered by a lipopolysaccharide-phospholipid outer layer (e.g., Beveridge, 1989). However, in spite of these differences in cell wall structure, both the modeling and the FTIR data showed little difference in the exudates from the two bacterial species. It may be that the soluble organics, which likely include polysaccharides and DNA, are similar for exudates from a range of bacterial species, leading to a ‘universal’ soluble fraction. This finding is similar to that of Borrok et al. (2005) which shows that a single set of ‘universal’ pK_a and site concentration values can be used to characterize the proton binding of a range of Gram-positive and Gram-negative bacteria, as well as a range of bacterial consortia (Borrok et al., 2005).

However, the bacterial exudates exhibit lower total site concentrations ($2.8\text{--}8.2 \times 10^{-5}$ mol/g with an average of $5.68 \times 10^{-5} \pm 2.08 \times 10^{-5}$ mol/g) compared to the bacterial cells that produced them. For example, *B. subtilis* cells have total site concentrations of $1.75 \times 10^{-4} \pm 2.4 \times 10^{-5}$, $3.19 \times 10^{-4} \pm 1.6 \times 10^{-5}$, and $3.44 \times 10^{-4} \pm 1.6 \times 10^{-5}$ mol/g in solutions of 0.01, 0.1, and 0.3 M NaClO₄, respectively (Borrok et al., 2005), which also show a trend of increasing values with increasing ionic strength as do the exudates studied here. The total site concentration for *S. oneidensis* cells in 0.1 M NaClO₄ is $3.9 \times$

10^{-4} mol/g (Mishra et al., 2010). Furthermore, the average total site concentration calculated from 36 sets of potentiometric titration data involving either bacterial species or bacterial consortia is $3.2 \pm 1.0 \times 10^{-4}$ mol/g (Borrok et al., 2005). Thus, the total site concentration for bacterial cells varies over a relatively small range, which is significantly higher than the range observed in this study for bacterial exudates. The total site concentrations for the exudates are closer to the total site concentrations calculated by Kaulbach et al. (2005) from the algal species *P. subcapitata* ($2.77 \times 10^{-5} \pm 2.9 \times 10^{-6}$ mol/g).

4.4. Conclusions

Potentiometric titrations and chemical equilibrium modeling were used to characterize the proton binding of bacterial exudates from *B. subtilis* and *S. oneidensis* bacterial cells. The calculated total buffering capacity of the bacterial exudates decreases with increasing ionic strength for the *B. subtilis* exudates but increases for the *S. oneidensis* exudates. Total site concentrations, which are likely related to buffering capacity, also change with ionic strength following the same trends as the buffering capacities. Calculated $pK_{a(i)}$ values and FTIR spectra, however, do not vary significantly as a function of ionic strength or bacterial type and concentration. This is somewhat remarkable as the two bacterial species have very different cell surfaces.

The total site concentrations calculated for the bacterial exudate solutions are approximately an order of magnitude lower per gram of bacteria than those calculated previously for a range of bacterial species. These differences suggest that exudates, with their lower site concentrations, are less efficient at binding protons and metals than

bacterial surfaces. However, the concentration and distribution of bacterial exudates in the environment are not well established, and they may constitute a significant portion of the proton and metal binding capacity of the aqueous phase, especially in bacteria-rich systems such as soils. The study of the effects and characteristics of bacterial exudates is in its infancy. These molecules can affect metal reduction, metal binding, and mineral dissolution rates, and the binding properties determined in this study provide a framework for understanding the mechanisms of how bacterial exudates interact with other components in geologic and engineered systems.

CHAPTER 5: CONCLUSIONS

A better understanding of the transport of mass, both organic and inorganic, in the environment is necessary in order to predict the fate of groundwater contaminants. The interactions of nanoparticles, as both grain coatings and suspended particles, were examined to better understand their potential behavior in the environment and the influence they might have on the transport of other components. In Chapter 2, a reverse osmosis surface water NOM isolate was used to examine the effects of pH and ionic strength on NOM retention in columns packed with naturally nanoparticle-coated quartz sands, as well as hematite and corundum sands. NOM retention, hence adsorption, increased with increasing ionic strength and decreasing pH. Analysis of column effluent showed that higher MW NOM preferentially adsorbed at pH 5-8 at 0.001 and 0.01 M ionic strengths. In the absence of NOM, Cd adsorption increased with increasing pH. In the presence of NOM, Cd adsorption slightly increased at pH 5 but increased more substantially at pH 8. At pH 8 but not pH 5, a slight decrease in NOM adsorption was observed in the presence of Cd, and preferential adsorption of the higher MW components was slightly enhanced by Cd at both pH values. Preferential adsorption of the higher MW NOM would decrease their mobility, and the greater binding ability of the higher MW NOM would also be likely to contribute to the reduced transport of metals and other contaminants, as was observed in the experiments with Cd. Preferential

adsorption of higher MW NOM would lead to enhanced relative mobility of the lower MW components, which are less aromatic and less likely to bind metals and hydrophobic organic compounds. This MW effect could thus act to limit the transport of metals and other contaminants. Therefore, NOM has the potential to affect contaminant mobility through sandy aquifers, with the effects likely dependent upon the properties of the NOM, solution conditions, and the presence of nanoparticle coatings or mobile nanoparticles.

Engineered nanoparticles, such as TiO_2 , also have the potential to be present as contaminants in the environment and can adsorb metals or adhere to other geosorbent surfaces. The adhesion of TiO_2 nanoparticles onto silica and Fe(III) oxide-coated silica surfaces was measured in Chapter 3 as a function of pH, nanoparticle concentration, and nanoparticle size. The extent of TiO_2 nanoparticle adhesion increased with increasing nanoparticle concentration, and both pH and nanoparticle size exerted strong effects on the adhesion behavior of the nanoparticles onto the uncoated silica particles. Below pH 6, the expected nanoparticle pH_{zpc} , TiO_2 nanoparticle adhesion increased with increasing particle size and pH; at pH 6 and above, adhesion occurred independently of pH and particle size. Within a given size fraction, preferential adhesion of the larger TiO_2 particles was observed below pH 6, and preferential adhesion of the smaller TiO_2 particles occurred at and above pH 6. Experiments with the Fe-coated silica grains were conducted only with the 26 nm TiO_2 nanoparticles, and, except at pH 6 where we observed significantly enhanced adhesion onto the Fe-coated silica relative to the uncoated silica, the extents of nanoparticle adhesion to the two geosorbents were the same within experimental uncertainty. The similarity in adhesion behaviors onto solids

with such different surface chemistries suggests that the properties of the TiO₂ nanoparticles, such as aggregation, and not of the mineral surfaces, are primarily responsible for governing adhesion.

Similar to NOM, other organic environmental components, such as bacterial exudates, also have the potential to influence contaminant transport and geochemical processes. In Chapter 4, exudates were collected from non-metabolizing Gram-positive (*Bacillus subtilis*) and Gram-negative (*Shewanella oneidensis*) bacterial species in a range of initial bacterial concentrations and ionic strengths. Exudate solutions were analyzed for total organic carbon concentrations, which varied as a function of bacterial type and concentration. However, FTIR spectra of all exudate samples were essentially identical under the range of experimental conditions. Potentiometric titrations of the exudate solutions were conducted for each of the bacterial concentrations and ionic strengths examined for both of the bacterial species. Both ‘up-pH’ and ‘down-pH’ titrations were conducted, and titration data were modeled using a discrete-site modeling approach. A 3-site model fit the titration data the best, and the calculated acidity constant values did not vary significantly as a function of bacterial species studied, ionic strength, or quantity of biomass used to generate the exudate solution. The calculated total buffering capacity and site concentrations varied with ionic strength and bacterial species. *B. subtilis* exudates showed a decrease in both total buffering capacity and site concentrations with increasing ionic strength, while *S. oneidensis* showed the reverse; however, the ranges of each were similar for both species. The total buffering capacity and site concentrations calculated for the bacterial exudate solutions are approximately an order of magnitude lower per gram of bacteria than those calculated previously for a

range of bacterial species. These differences suggest that exudates are less efficient at binding protons and metals than bacterial surfaces. However, the concentration and distribution of bacterial exudates in the environment is unknown and could constitute a significant portion of the proton and metal binding capacity of the aqueous phase. These molecules can affect a range of geochemical processes, and the binding properties determined in this study provide a framework for understanding how bacterial exudates interact with other components in geologic and engineered systems.

Overall, we observed that the interactions between engineered and environmental nanoparticles, as both grain coatings and in suspension, mineral surfaces, organic molecules, and metals are complex and capable of influencing one another's transport in aqueous systems. In the future, it would be beneficial to study the interactions of suspended nanoparticles with NOM, bacterial surfaces, and bacterial exudates, to determine what influences these ubiquitous organic environmental components have on nanoparticle aggregation and transport. A characterization of the proton binding of exudates from additional bacterial species is also crucial in order to determine if the similarities observed herein can be generalized to exudates of a broad range of bacterial species. In addition, studying the effects of bacterial exudates on the partitioning of metals in water-rock systems would be valuable for understanding the role of exudates in contaminant fate and transport. The behavior of engineered nanoparticles and exudates in environmental systems has not been well characterized thus far, and it is vital to determine their place in an already complex environmental framework that includes NOM, mineral and bacterial surfaces, and metals and other contaminants.

APPENDIX A:
BREAKTHROUGH CURVES, ABSORBANCE RATIOS, AND MOLECULAR
WEIGHT DISTRIBUTIONS

A.1 Comparison of 254, 280, and 350 nm NOM Breakthrough Curves in Oyster Sand

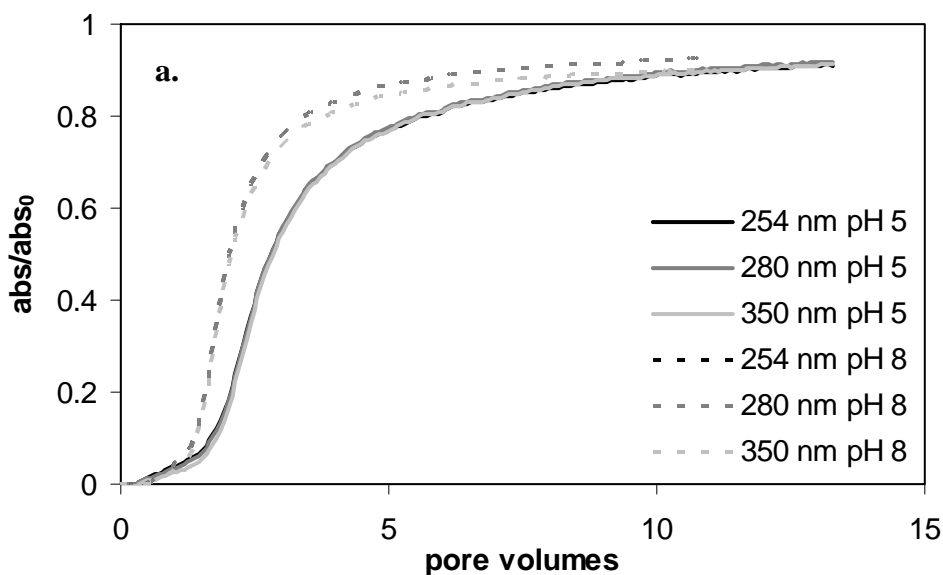


Figure A.1 Comparison of normalized breakthrough curves of NOM in the Oyster sand at pH 5 and 8 made using UV/vis absorbance at 254, 280, and 350 nm. At 0.001 M (a and b—zoom in), there was no difference between the 254 and 280 nm breakthrough curves; the 350 nm breakthrough curve was slightly lower. At 0.01 M (c and d—zoom in), there were slight differences between the 280 and 350 nm breakthrough curves and the 254 nm breakthrough curves. At 0.1 M (e and f—zoom in), there were slight differences between the 280 and 350 nm breakthrough curves and the 254 nm breakthrough curves. In the Cd, 5 ppm NOM experiment at 0.01 M (g and h—zoom in), the 350 nm breakthrough curves were lower than the 254 and 280 nm breakthrough curves (p. 97-p. 101).

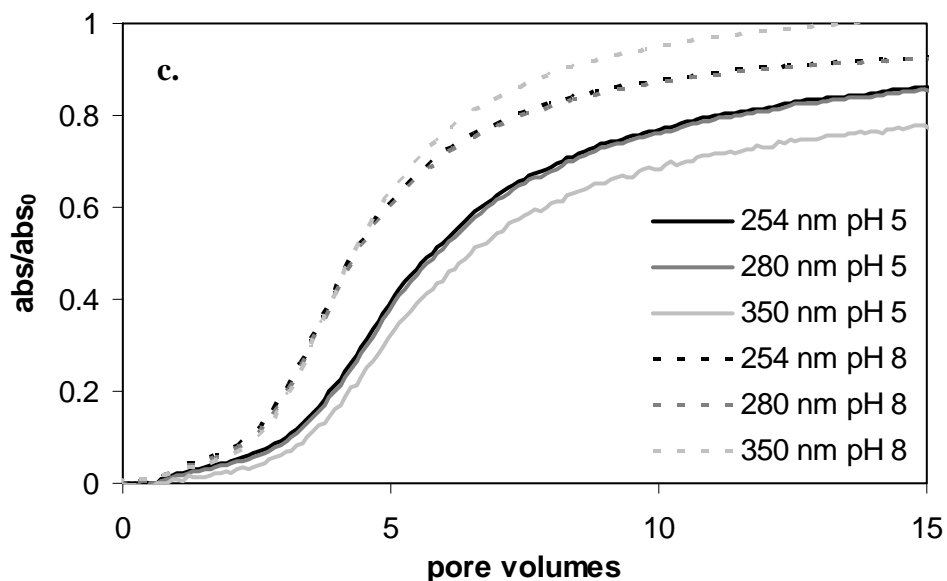
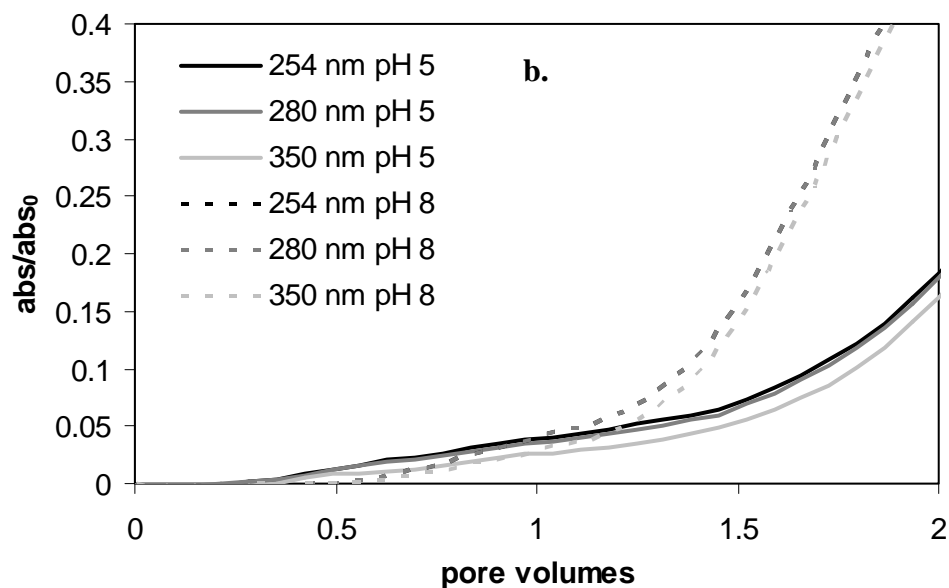


Figure A.1 Comparison of normalized breakthrough curves of NOM in the Oyster sand at pH 5 and 8 made using UV/vis absorbance at 254, 280, and 350 nm. At 0.001 M (a and b—zoom in), there was no difference between the 254 and 280 nm breakthrough curves; the 350 nm breakthrough curve was slightly lower. At 0.01 M (c and d—zoom in), there were slight differences between the 280 and 350 nm breakthrough curves and the 254 nm breakthrough curves. At 0.1 M (e and f—zoom in), there were slight differences between the 280 and 350 nm breakthrough curves and the 254 nm breakthrough curves. In the Cd, 5 ppm NOM experiment at 0.01 M (g and h—zoom in), the 350 nm breakthrough curves were lower than the 254 and 280 nm breakthrough curves (p. 97-p. 101).

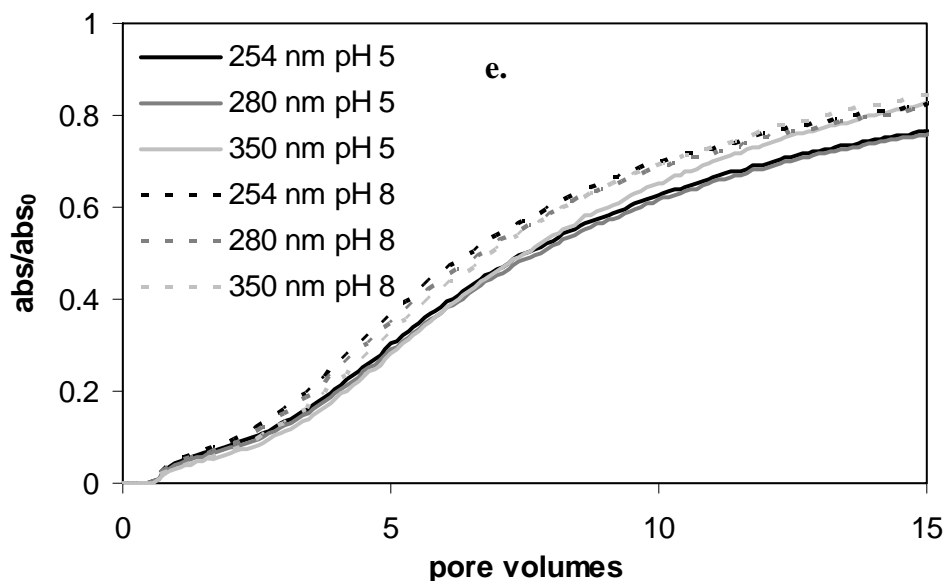
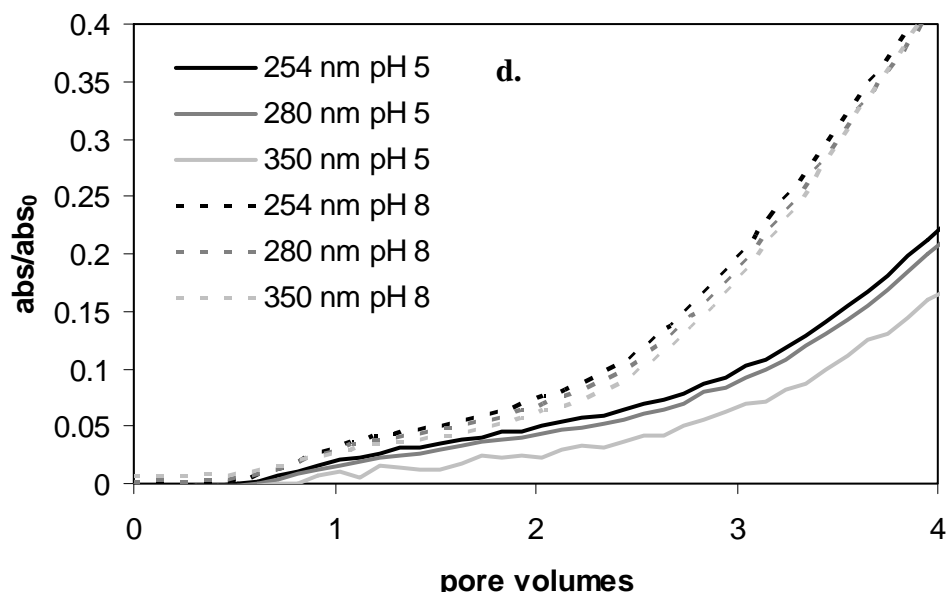


Figure A.1 Comparison of normalized breakthrough curves of NOM in the Oyster sand at pH 5 and 8 made using UV/vis absorbance at 254, 280, and 350 nm. At 0.001 M (a and b—zoom in), there was no difference between the 254 and 280 nm breakthrough curves; the 350 nm breakthrough curve was slightly lower. At 0.01 M (c and d—zoom in), there were slight differences between the 280 and 350 nm breakthrough curves and the 254 nm breakthrough curves. At 0.1 M (e and f—zoom in), there were slight differences between the 280 and 350 nm breakthrough curves and the 254 nm breakthrough curves. In the Cd, 5 ppm NOM experiment at 0.01 M (g and h—zoom in), the 350 nm breakthrough curves were lower than the 254 and 280 nm breakthrough curves (p. 97-p. 101).

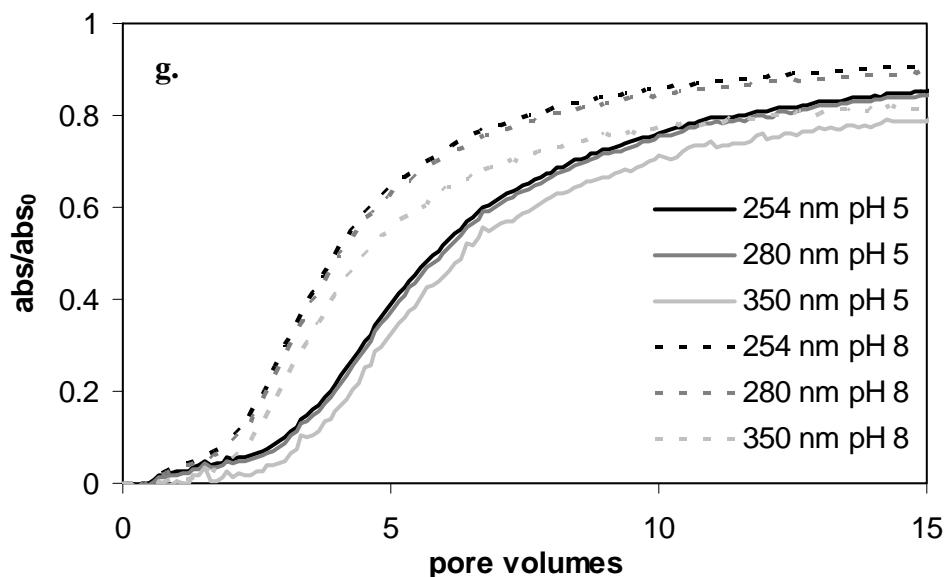
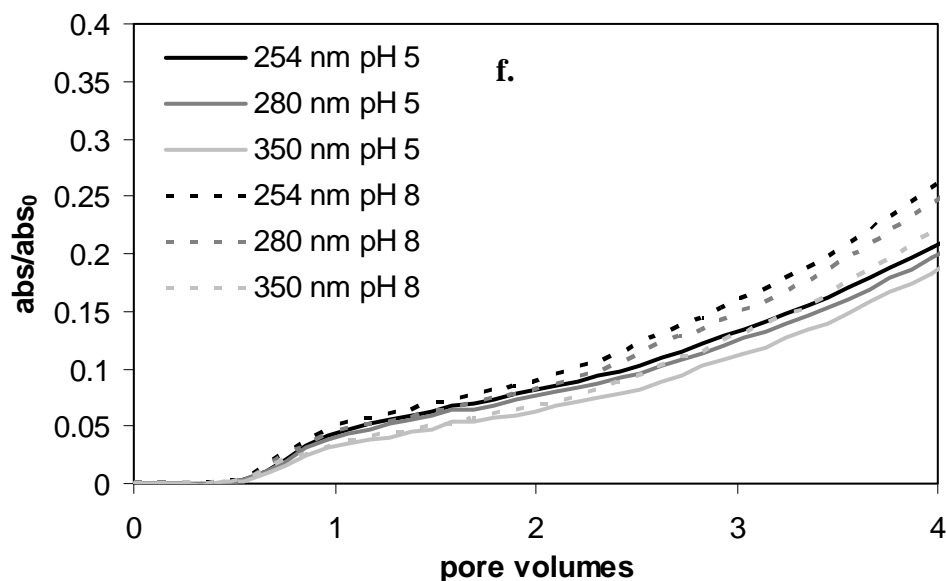


Figure A.1 Comparison of normalized breakthrough curves of NOM in the Oyster sand at pH 5 and 8 made using UV/vis absorbance at 254, 280, and 350 nm. At 0.001 M (a and b—zoom in), there was no difference between the 254 and 280 nm breakthrough curves; the 350 nm breakthrough curve was slightly lower. At 0.01 M (c and d—zoom in), there were slight differences between the 280 and 350 nm breakthrough curves and the 254 nm breakthrough curves. At 0.1 M (e and f—zoom in), there were slight differences between the 280 and 350 nm breakthrough curves and the 254 nm breakthrough curves. In the Cd, 5 ppm NOM experiment at 0.01 M (g and h—zoom in), the 350 nm breakthrough curves were lower than the 254 and 280 nm breakthrough curves (p. 97-p. 101).

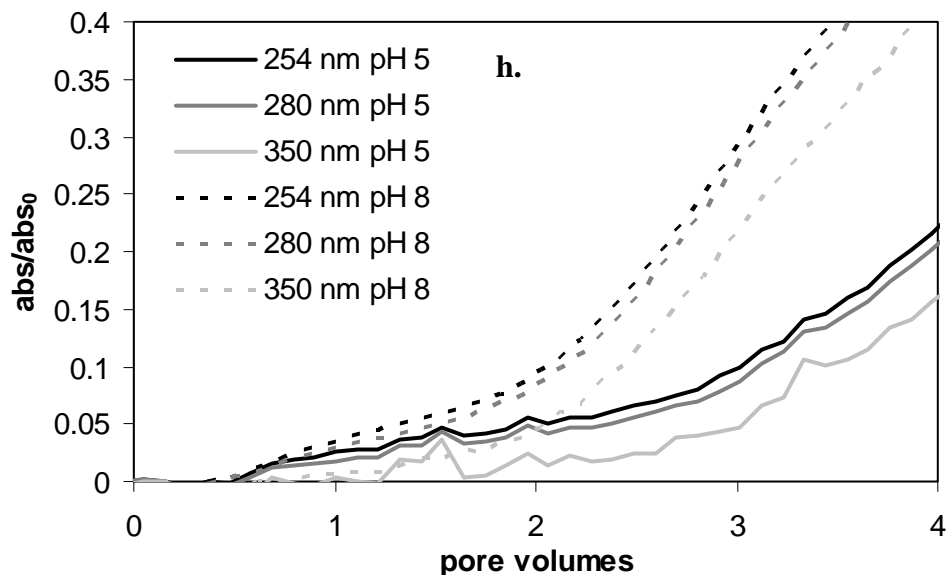


Figure A.1 Comparison of normalized breakthrough curves of NOM in the Oyster sand at pH 5 and 8 made using UV/vis absorbance at 254, 280, and 350 nm. At 0.001 M (a and b—zoom in), there was no difference between the 254 and 280 nm breakthrough curves; the 350 nm breakthrough curve was slightly lower. At 0.01 M (c and d—zoom in), there were slight differences between the 280 and 350 nm breakthrough curves and the 254 nm breakthrough curves. At 0.1 M (e and f—zoom in), there were slight differences between the 280 and 350 nm breakthrough curves and the 254 nm breakthrough curves. In the Cd, 5 ppm NOM experiment at 0.01 M (g and h—zoom in), the 350 nm breakthrough curves were lower than the 254 and 280 nm breakthrough curves (p. 97-p. 101).

A.2 Hematite and Corundum Breakthrough Curves

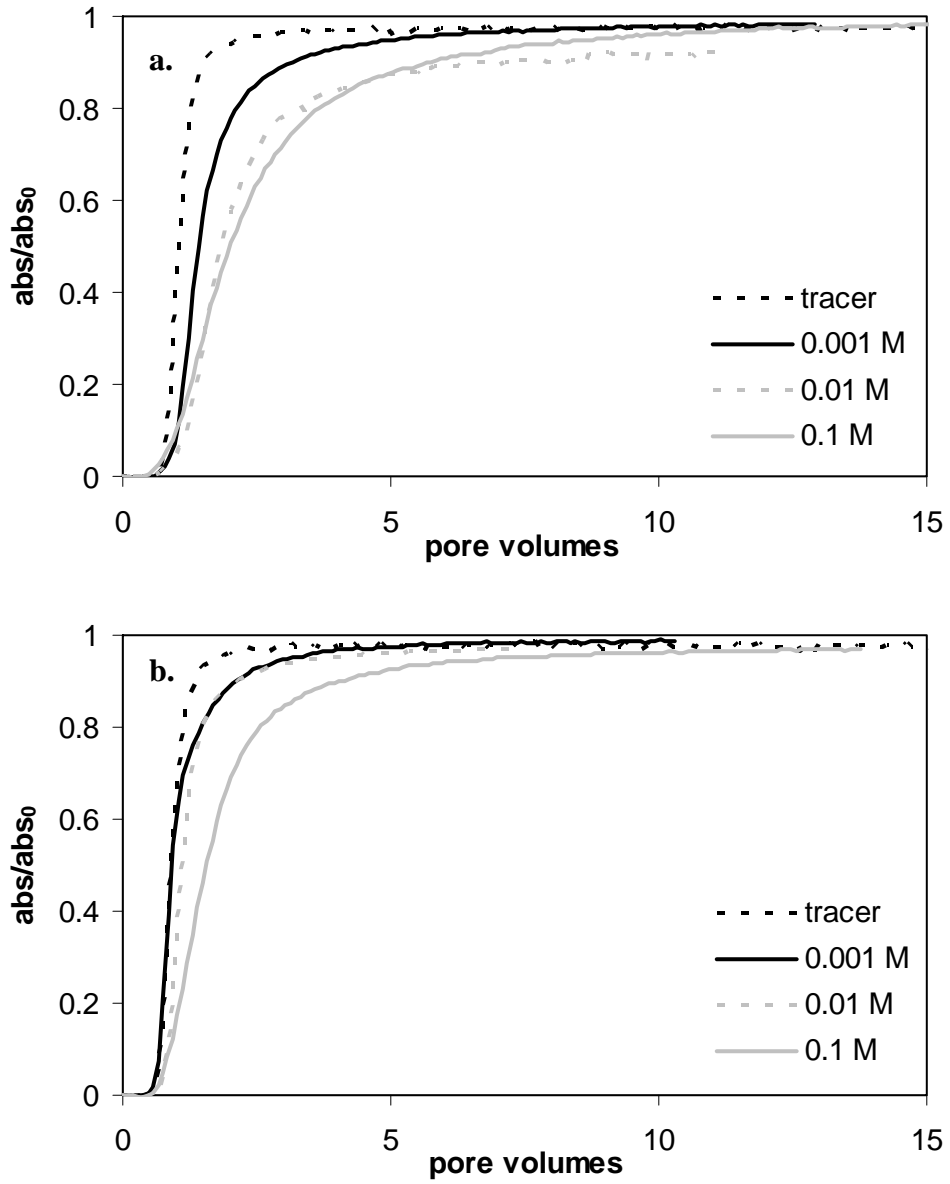


Figure A.2 NOM retention increased as a function of ionic strength on hematite sand at a) pH 5 and b) pH 8 and on corundum sand at c) pH 5 and d) pH 8 (p. 102-p. 103).

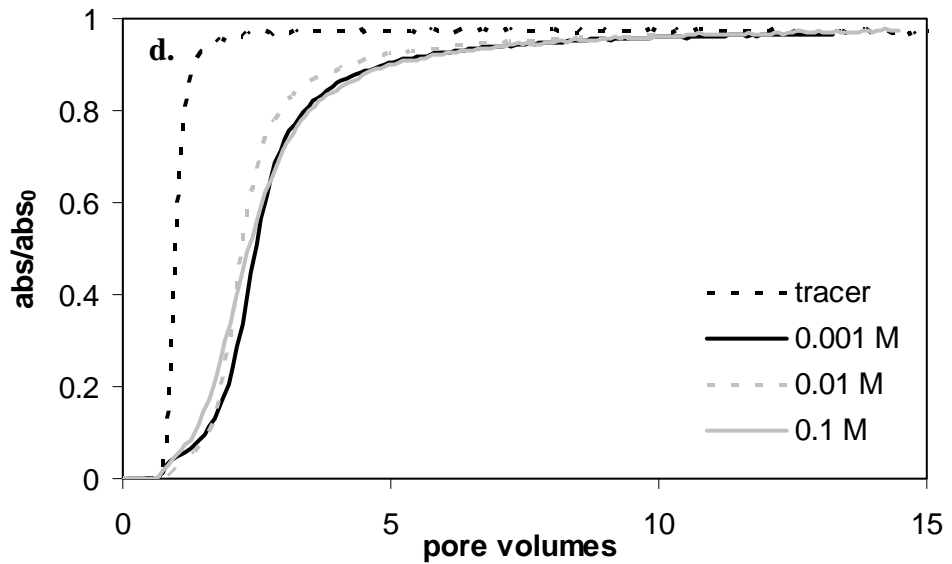
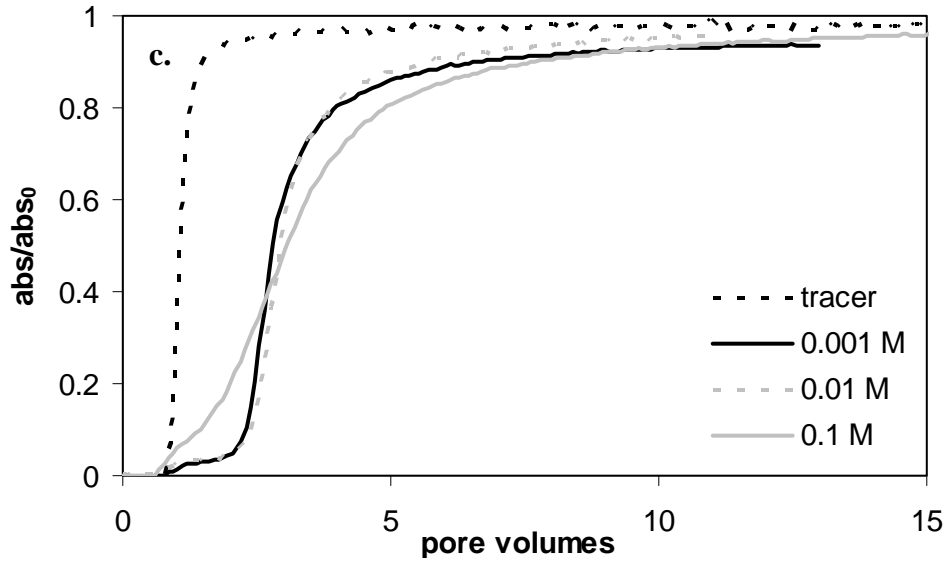


Figure A.2 NOM retention increased as a function of ionic strength on hematite sand at a) pH 5 and b) pH 8 and on corundum sand at c) pH 5 and d) pH 8 (p. 102-p. 103).

A.3 Comparison Breakthrough Curves

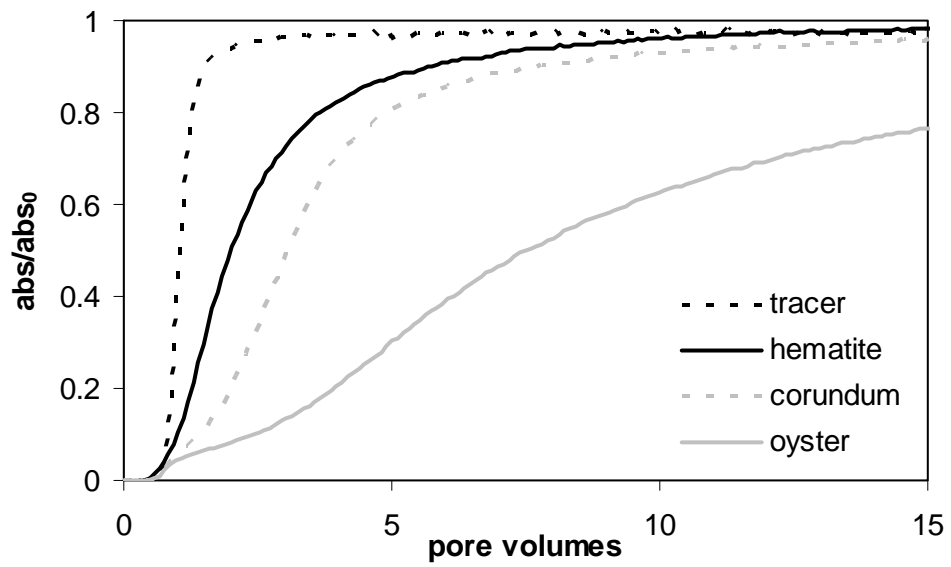


Figure A.3 At pH 5 in 0.1 M NaClO₄, NOM in the Oyster sand adsorbed more than in either the hematite or corundum sands.

A.4 280 nm/254 nm Absorbance Ratios

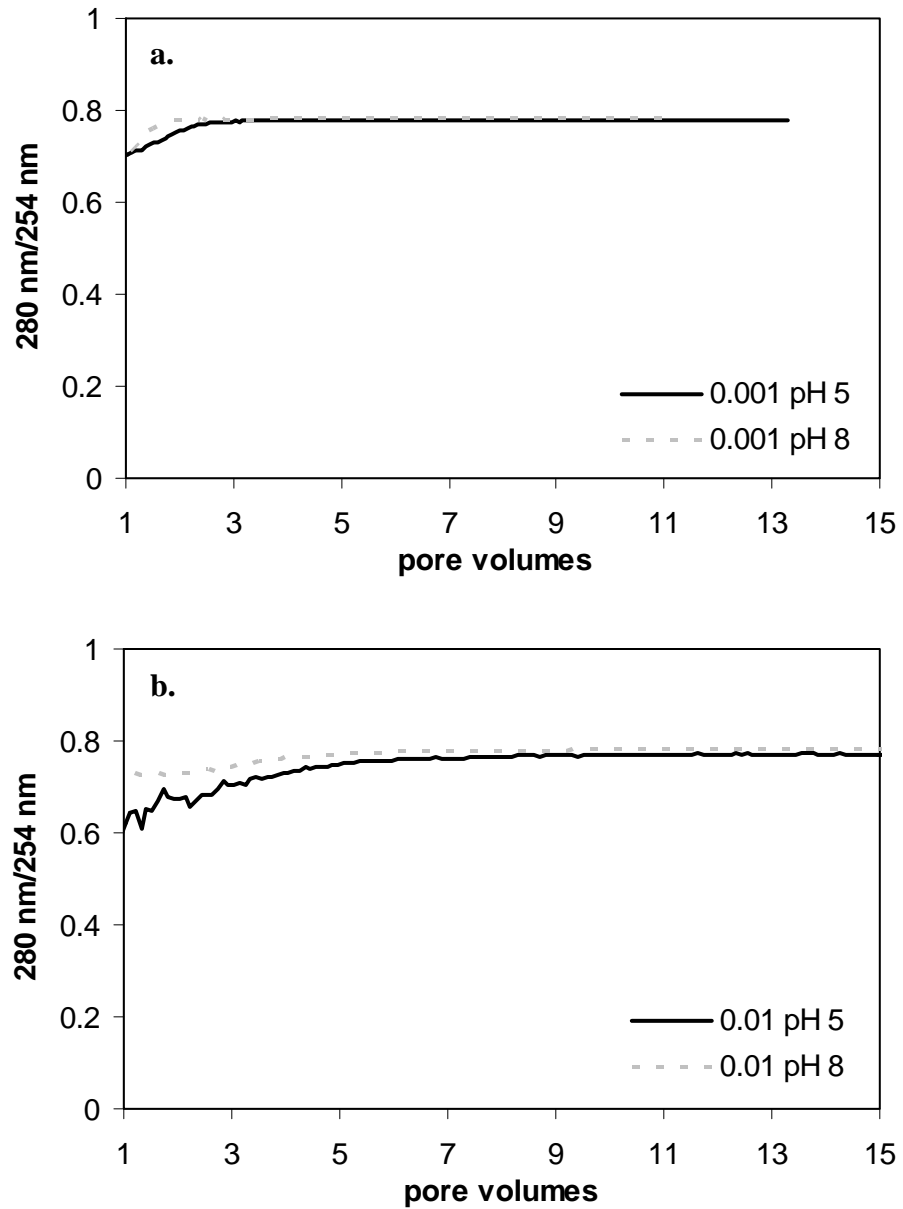


Figure A.4 Effluent NOM absorbance ratio (280 nm/254 nm) increased during Oyster sand column experiments at a) 0.001 M, b) 0.01 M, and c) 0.1 M, indicating initial preferential retention of aromatic NOM. Black solid lines are pH 5, and gray dashed lines are pH 8 (p. 105-p. 106).

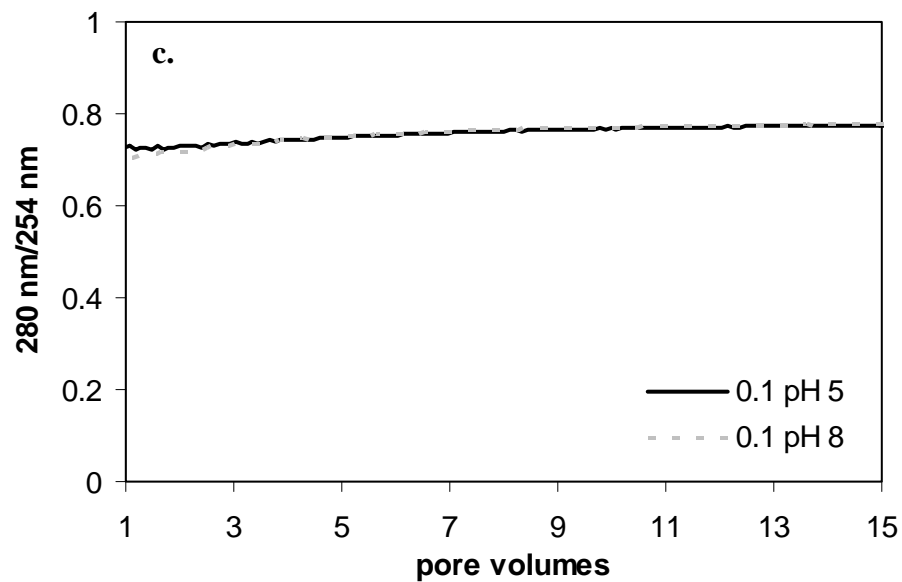


Figure A.4 Effluent NOM absorbance ratio (280 nm/254 nm) increased during Oyster sand column experiments at a) 0.001 M, b) 0.01 M, and c) 0.1 M, indicating initial preferential retention of aromatic NOM. Black solid lines are pH 5, and gray dashed lines are pH 8 (p. 105-p. 106).

A.5 350 nm/254 nm Absorbance Ratios

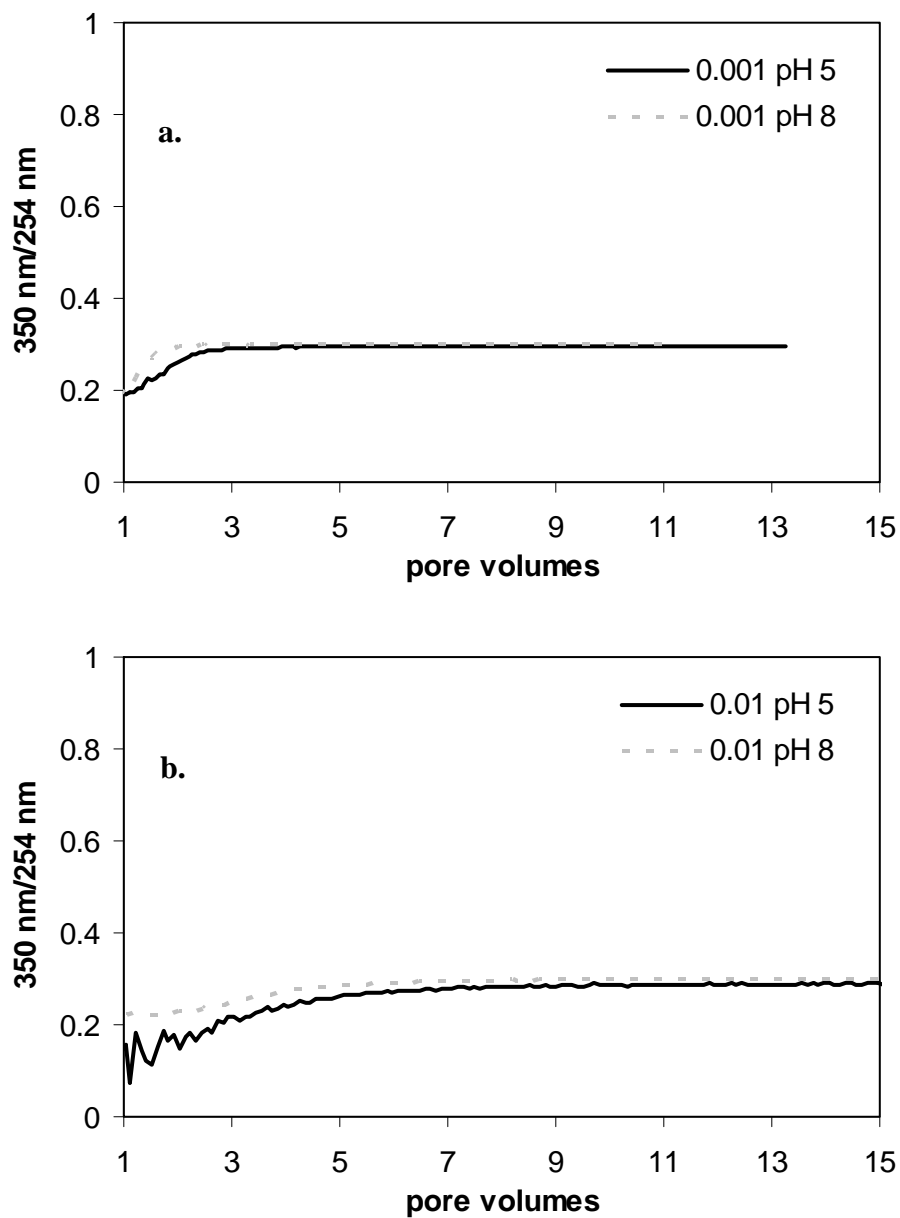


Figure A.5 Effluent NOM absorbance ratio (350 nm/254 nm) increased during column experiments at a) 0.001 M, b) 0.01 M, and c) 0.1 M, indicating initial preferential retention of lignin-derived NOM. Black solid lines are pH 5, and gray dashed lines are pH 8 (p. 107-p. 108).

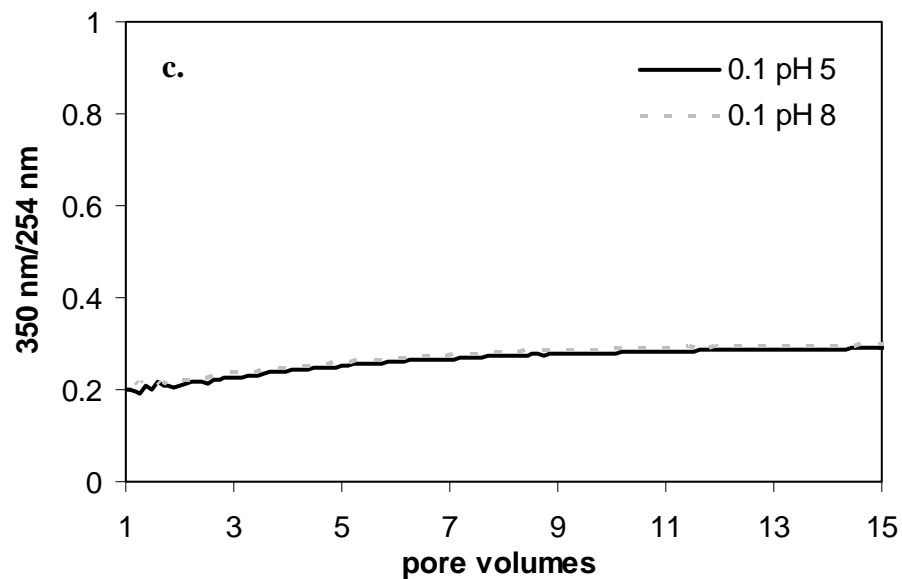


Figure A.5 Effluent NOM absorbance ratio (350 nm/254 nm) increased during column experiments at a) 0.001 M, b) 0.01 M, and c) 0.1 M, indicating initial preferential retention of lignin-derived NOM. Black solid lines are pH 5, and gray dashed lines are pH 8 (p. 107-p. 108).

A.6 Influent Molecular Weight Distributions as a Function of pH

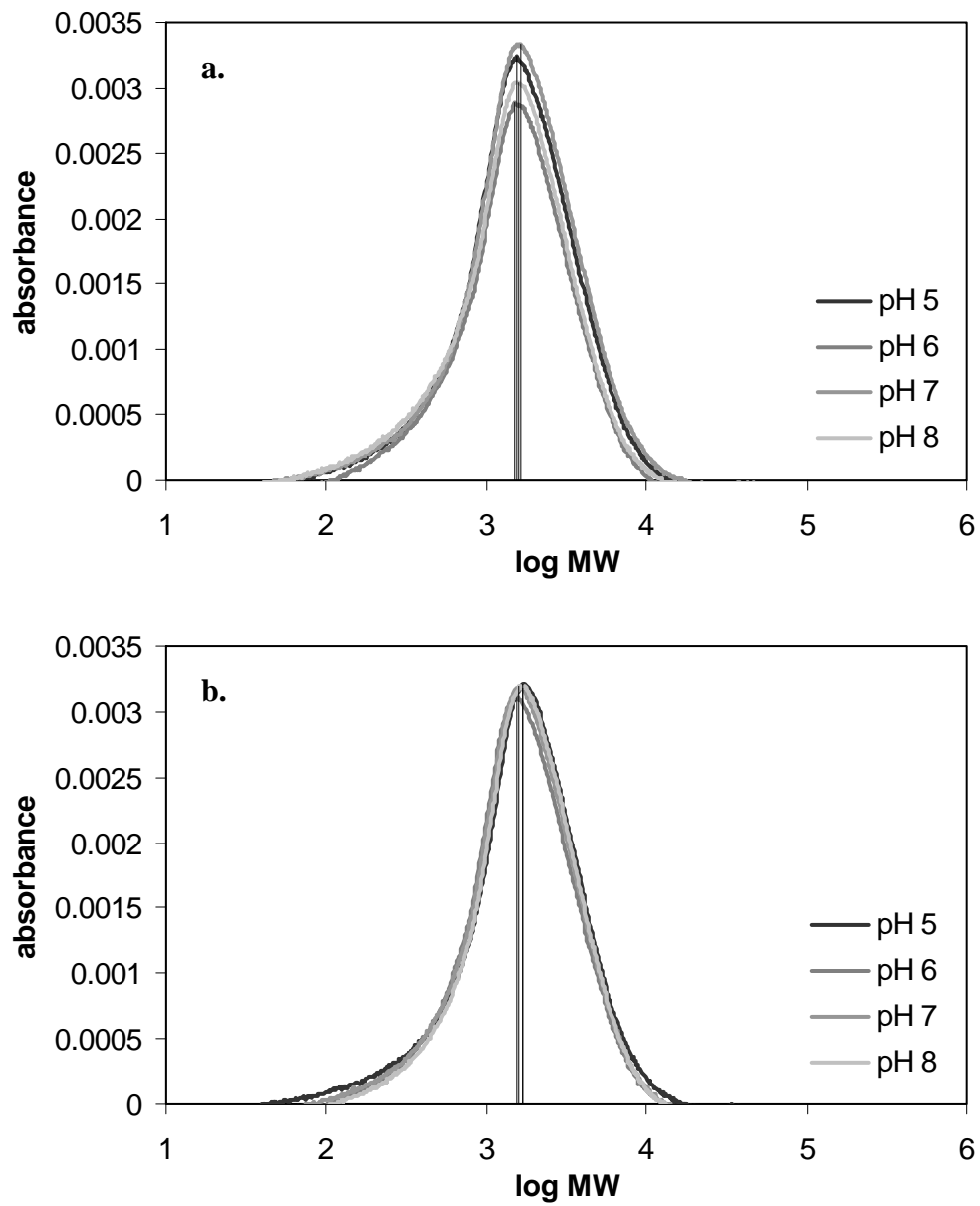


Figure A.6 Influent NOM molecular weight distributions in a) 0.001 M or b) 0.01 M NaClO_4 did not change at pH 5, 6, 7, and 8.

A.7 Retained NOM Molecular Weight Distributions

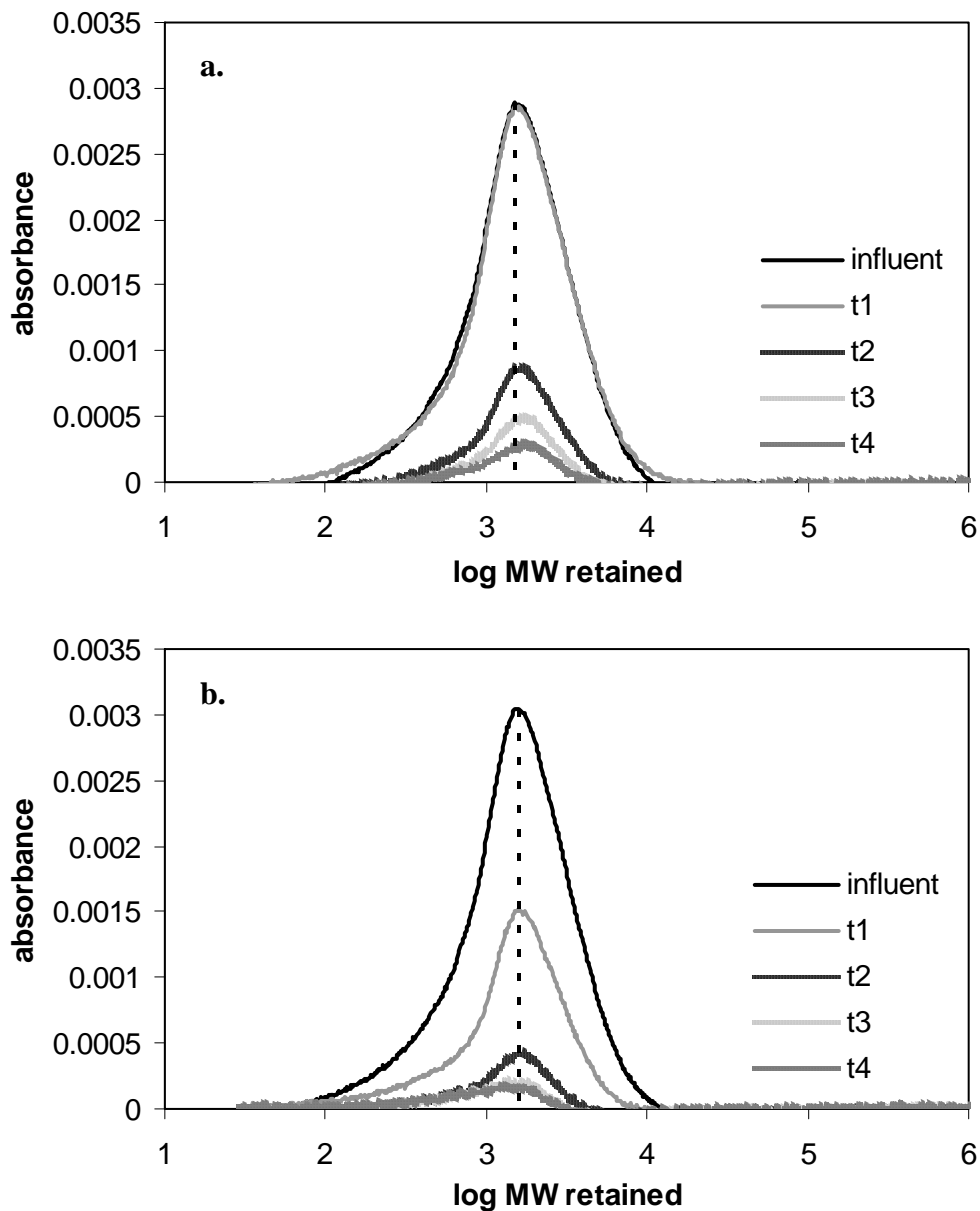


Figure A.7 MW distributions of NOM retained in the column at each sampling period compared to the influent MW distribution. Experiments conducted with 5 ppm C at a) pH 6 in 0.001 M and at pH 8 in b) 0.001 M and c) 0.01 M. Dashed vertical line represents the MW peak of the influent solution. Peaks shifted toward higher MW NOM retained as experiments progressed (p. 110-p. 111).

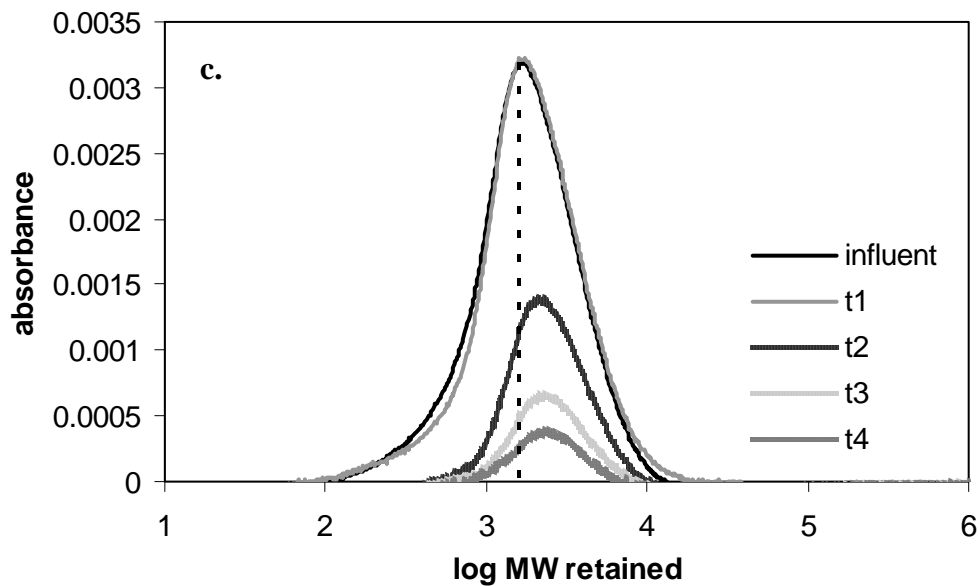


Figure A.7 MW distributions of NOM retained in the column at each sampling period compared to the influent MW distribution. Experiments conducted with 5 ppm C at a) pH 6 in 0.001 M and at pH 8 in b) 0.001 M and c) 0.01 M. Dashed vertical line represents the MW peak of the influent solution. Peaks shifted toward higher MW NOM retained as experiments progressed (p. 110-p. 111).

A.8 Cd(II) Breakthrough Curves

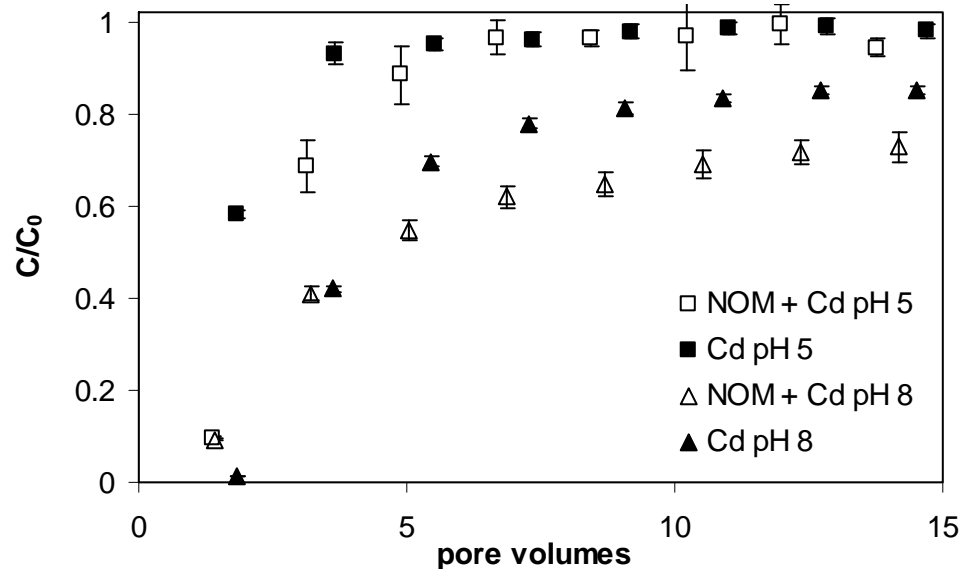


Figure A.8 20 ppm C NOM increased Cd adsorption onto Oyster sand in 0.01 M NaClO₄ at pH 8 (triangles) but only slightly at pH 5 (squares). Solid symbols are Cd-only and open symbols are Cd plus NOM. The increase with 20 ppm C was less than that with 5 ppm C (Figure 2.5).

A.9 280 nm/254 nm Absorbance Ratios with Cd

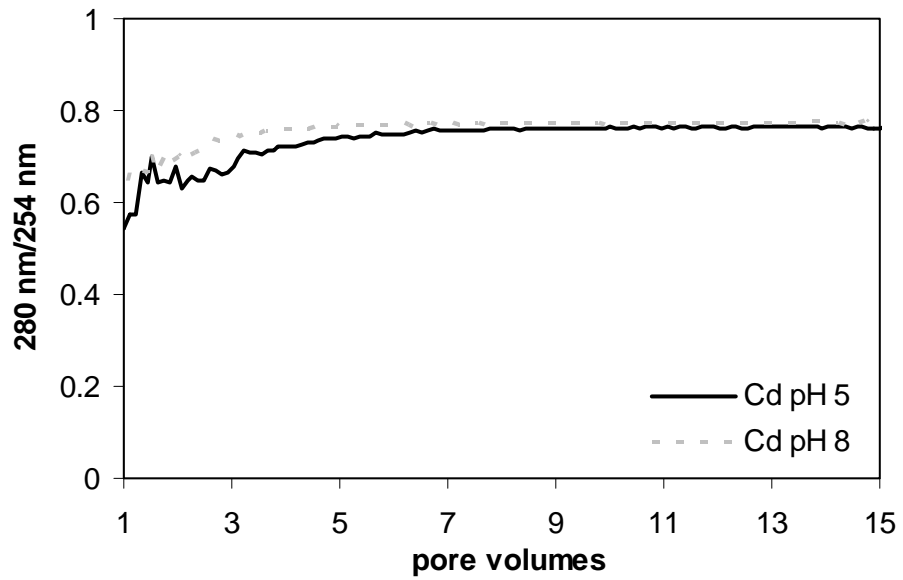


Figure A.9 Effluent NOM absorbance ratio (280 nm/254 nm) increased during column experiments at 0.01 M plus Cd. Black solid lines are pH 5, and gray dashed lines are pH 8.

A.10 350 nm/254 nm Absorbance Ratios with Cd

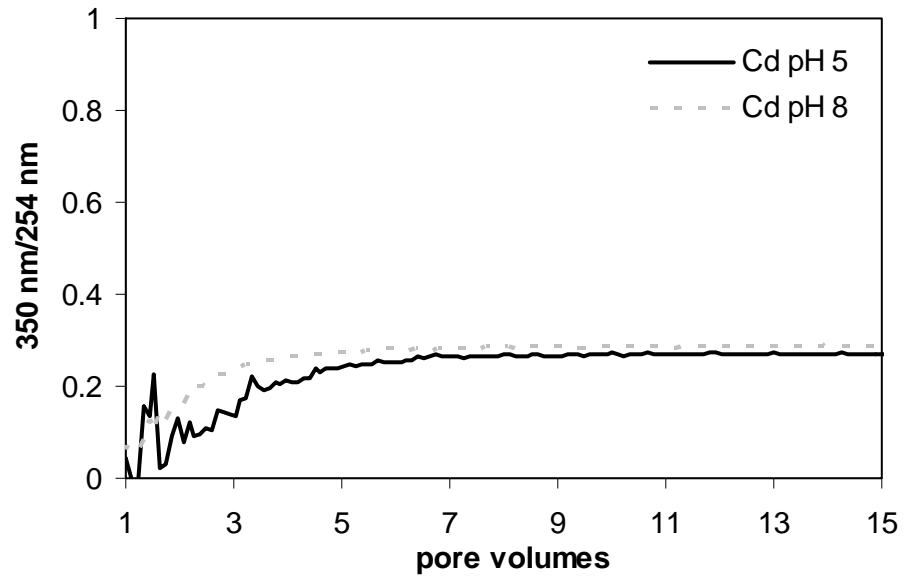


Figure A.10 Effluent NOM absorbance ratio (350 nm/254 nm) increased during column experiments at 0.01 M plus Cd. Black solid lines are pH 5, and gray dashed lines are pH 8.

A.11 Retained NOM Molecular Weight Distributions with Cd

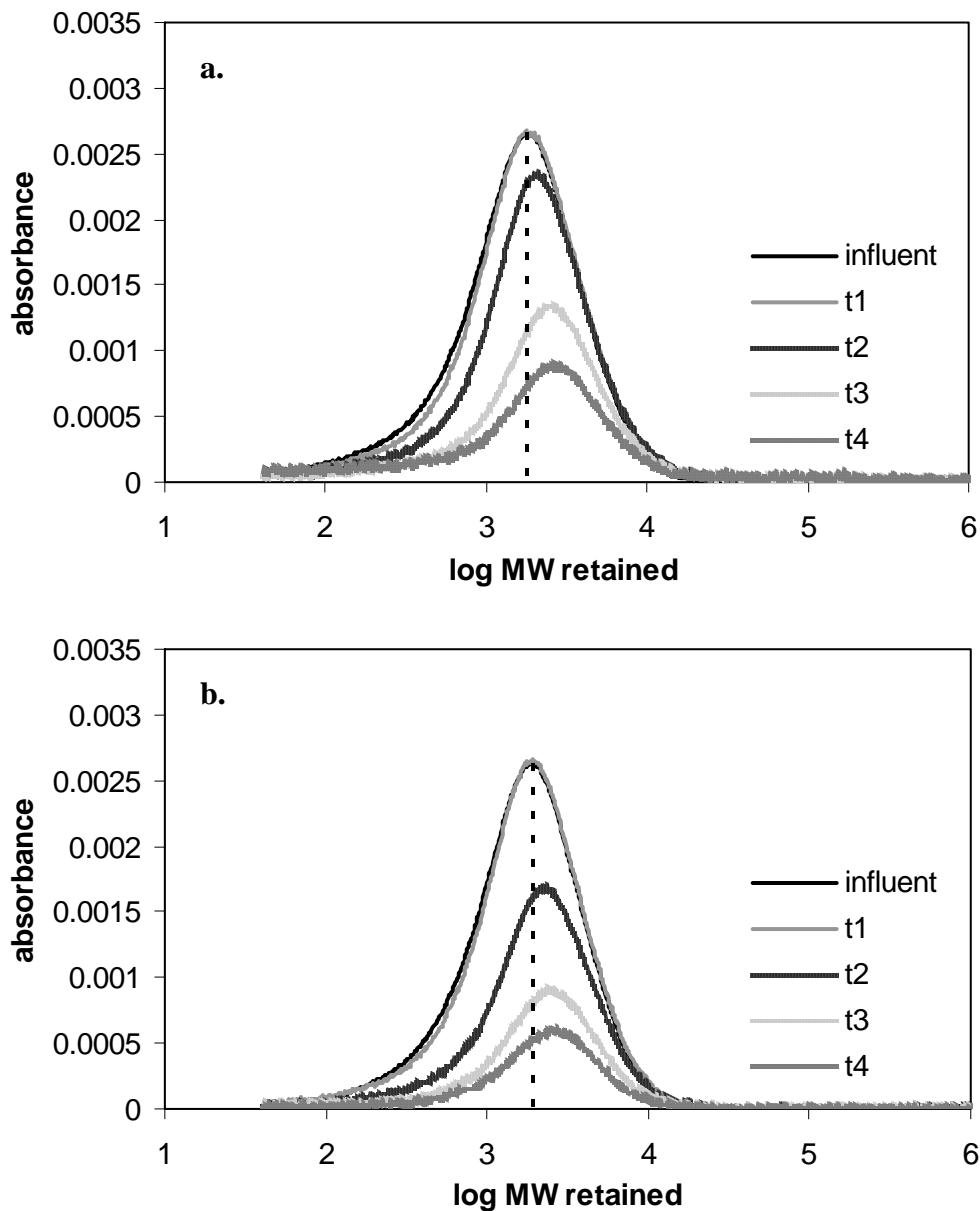


Figure A.11 In the presence of 2.5 ppm Cd, MW distributions of NOM retained in the column at each sampling period compared to the influent MW distribution. Experiments conducted with 5 ppm C initial NOM and 0.01 M at a) pH 6 and b) pH 8 or with 20 ppm C initial NOM and 0.01 M at c) pH 6 and d) pH 8. Dashed vertical line represents the MW peak of the influent solution. Peaks shifted toward higher MW NOM retained as experiments progressed, and this shift occurred more quickly with 20 ppm C than with 5 ppm C and at pH 8 than at pH 6 (p. 115-p. 116).

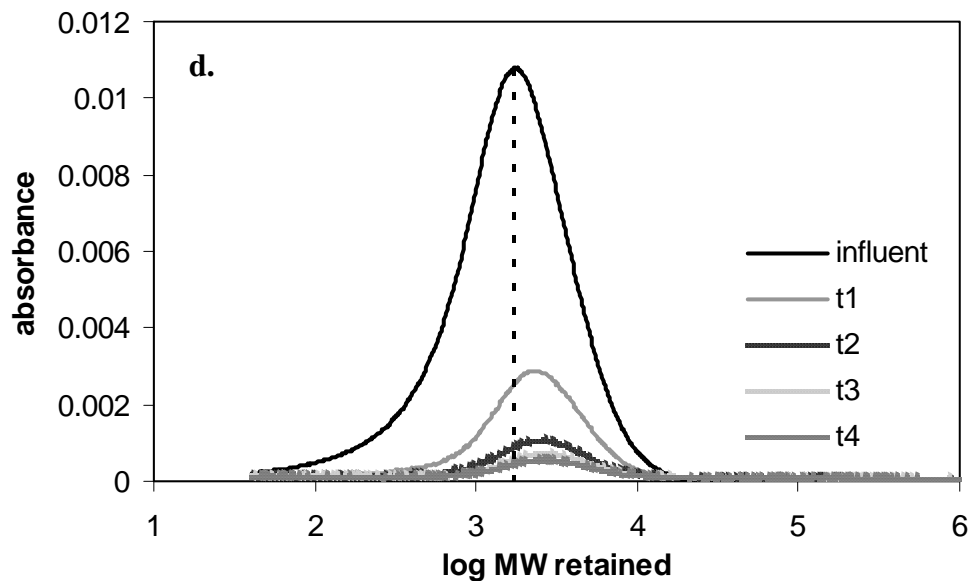
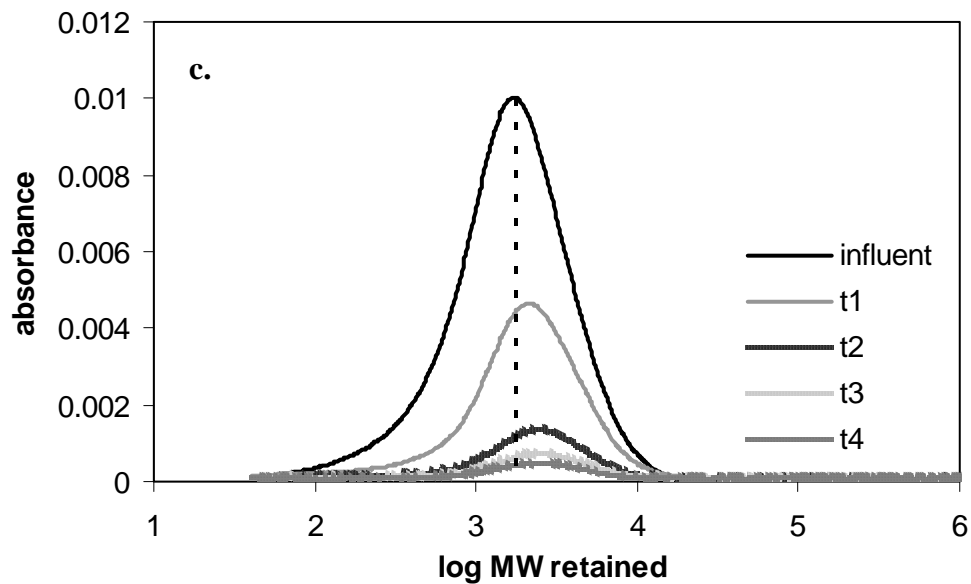


Figure A.11 In the presence of 2.5 ppm Cd, MW distributions of NOM retained in the column at each sampling period compared to the influent MW distribution. Experiments conducted with 5 ppm C initial NOM and 0.01 M at a) pH 6 and b) pH 8 or with 20 ppm C initial NOM and 0.01 M at c) pH 6 and d) pH 8. Dashed vertical line represents the MW peak of the influent solution. Peaks shifted toward higher MW NOM retained as experiments progressed, and this shift occurred more quickly with 20 ppm C than with 5 ppm C and at pH 8 than at pH 6 (p. 115-p. 116).

APPENDIX B:
ABSORBANCE AND ADHESION DATA

B.1 Control Experiments

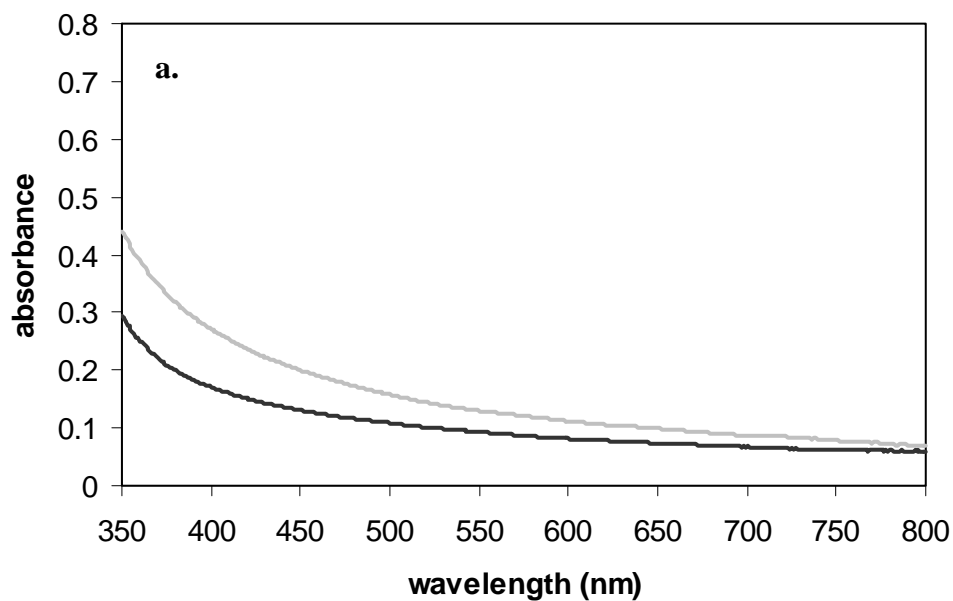


Figure B.1 Control experiments with 50 mg/L 26 nm TiO₂ in 0.01 M NaClO₄ (black line) and in 0.01 M NaClO₄ that was exposed to Fe-coated silica for 3 hours (gray line) at a) pH 4, b) pH 5, and c) pH 8, where the lines are virtually indistinguishable (p. 117-p. 118).

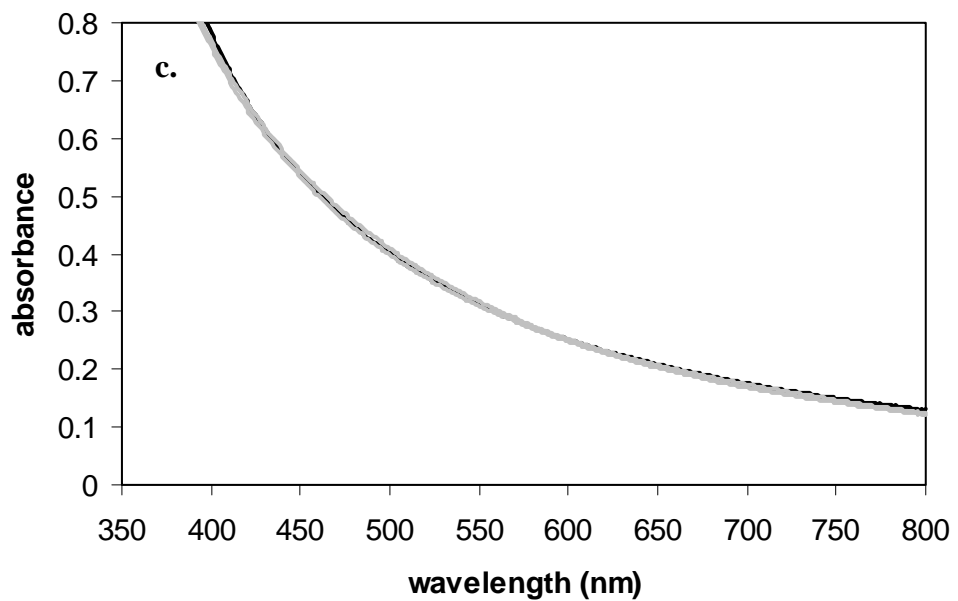
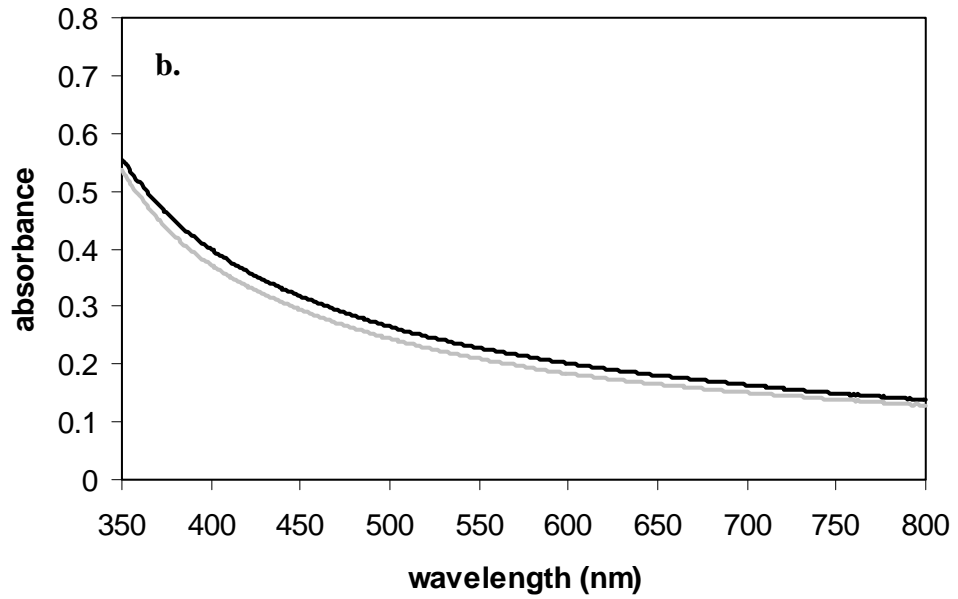


Figure B.1 Control experiments with 50 mg/L 26 nm TiO₂ in 0.01 M NaClO₄ (black line) and in 0.01 M NaClO₄ that was exposed to Fe-coated silica for 3 hours (gray line) at a) pH 4, b) pH 5, and c) pH 8, where the lines are virtually indistinguishable (p. 117-p. 118).

B.2 TiO₂ Adhesion onto Uncoated and Fe-Coated Silica

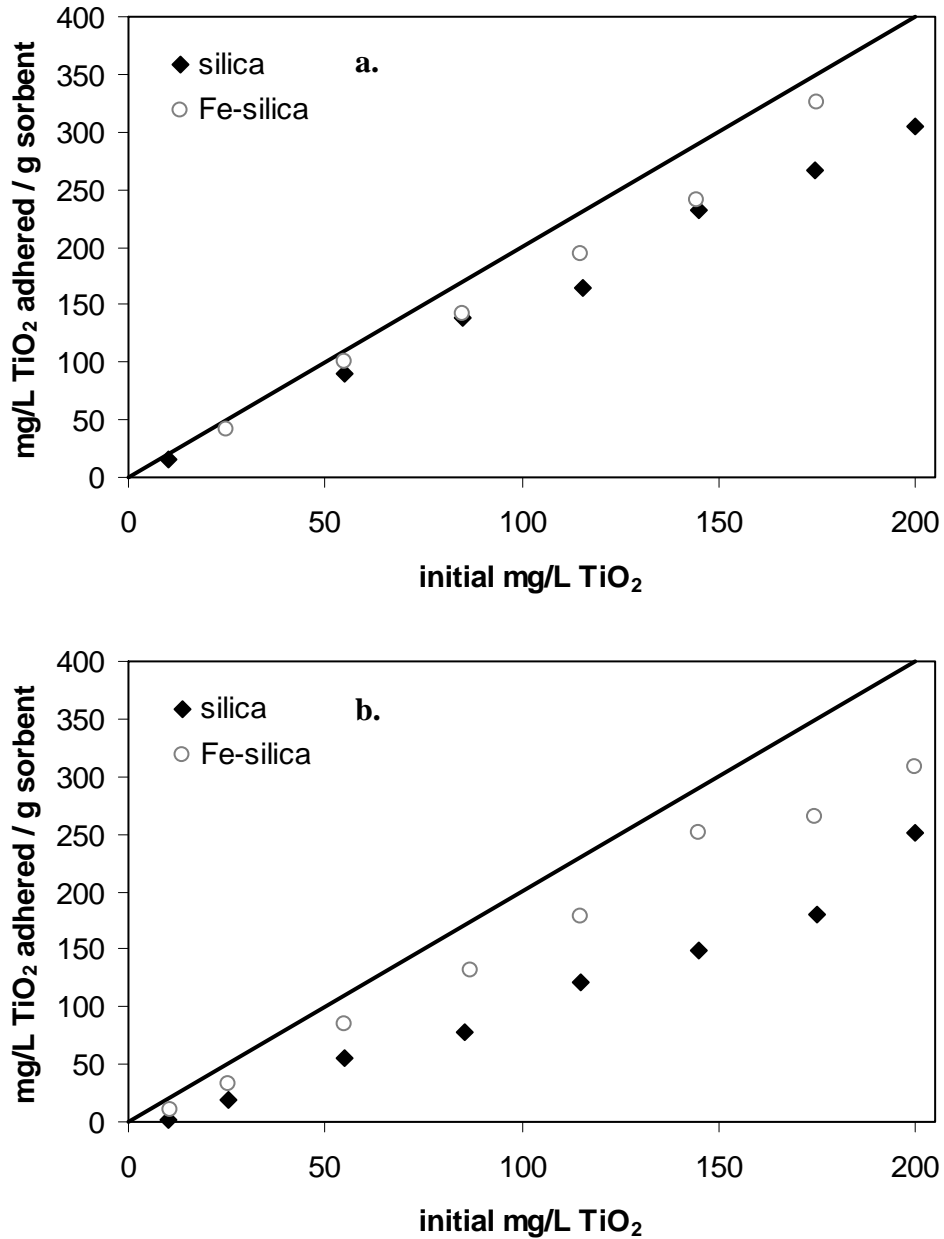


Figure B.2 26 nm TiO₂ nanoparticle adhesion to uncoated and Fe-coated silica grains at pH 5-8 (a-d). Black diamonds represent the uncoated silica and open circles the coated silica. The black line represents 100% adhesion. In cases where adhesion was too close to the detection limits, the data are not presented (p. 119-p. 120).

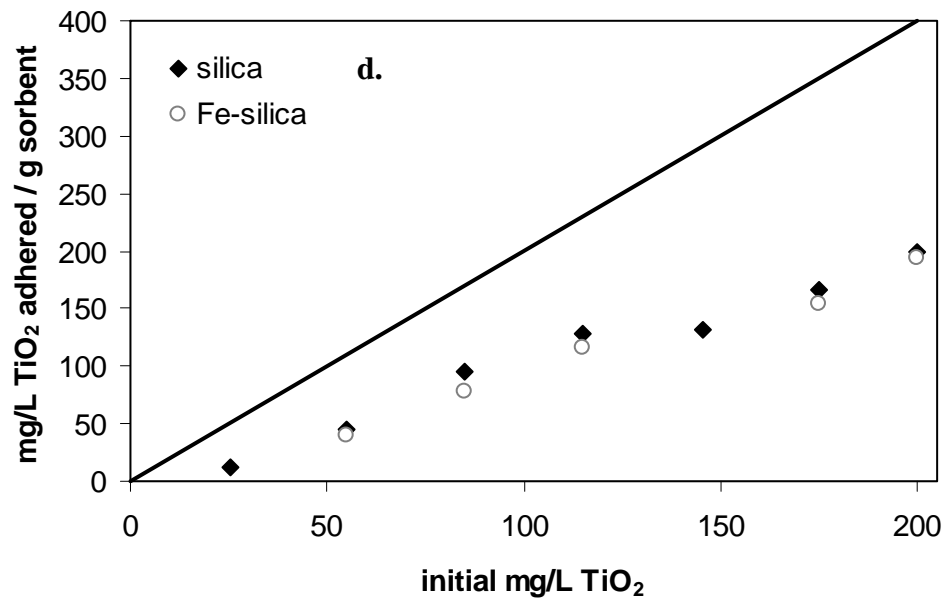
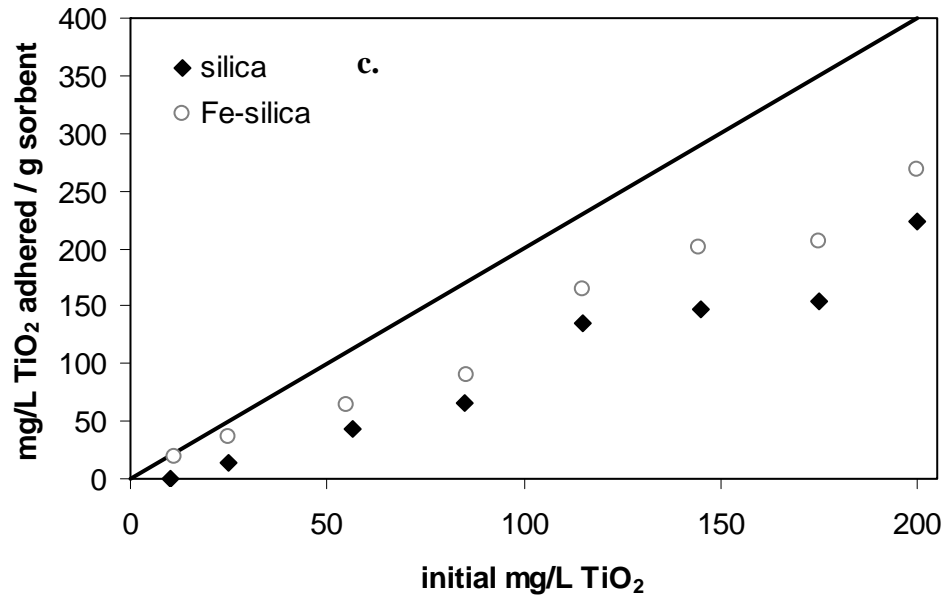


Figure B.2 26 nm TiO₂ nanoparticle adhesion to uncoated and Fe-coated silica grains at pH 5-8 (a-d). Black diamonds represent the uncoated silica and open circles the coated silica. The black line represents 100% adhesion. In cases where adhesion was too close to the detection limits, the data are not presented (p. 119-p. 120).

APPENDIX C:

CALCULATED VALUES FROM EXUDATE TITRATIONS

TABLE C.1

CALCULATED $\text{pK}_{\text{A}(i)}$ VALUES AND SITE CONCENTRATIONS (MOL/G) FROM THE 3-SITE MODEL OF *B. SUBTILIS* EXUDATE TITRATIONS.

40 g/L, 0.01 M	$\text{pK}_{\text{a}(1)}$	[site 1]	$\text{pK}_{\text{a}(2)}$	[site 2]	$\text{pK}_{\text{a}(3)}$	[site 3]	Total sites
forward average	4.08 ± 0.06	3.19 × 10 ⁻⁵ ± 2.84 × 10 ⁻⁶	6.86 ± 0.12	1.22 × 10 ⁻⁵ ± 1.34 × 10 ⁻⁶	9.41 ± 0.06	3.18 × 10 ⁻⁵ ± 3.87 × 10 ⁻⁶	7.58 × 10 ⁻⁵ ± 6.90 × 10 ⁻⁶
reverse average	4.02 ± 0.05	3.31 × 10 ⁻⁵ ± 2.38 × 10 ⁻⁶	6.73 ± 0.10	1.20 × 10 ⁻⁵ ± 8.81 × 10 ⁻⁷	9.39 ± 0.04	3.17 × 10 ⁻⁵ ± 3.20 × 10 ⁻⁶	7.68 × 10 ⁻⁵ ± 5.84 × 10 ⁻⁶
combined average	4.05 ± 0.06	3.25 × 10 ⁻⁵ ± 2.61 × 10 ⁻⁶	6.79 ± 0.12	1.21 × 10 ⁻⁵ ± 1.10 × 10 ⁻⁶	9.40 ± 0.05	3.17 × 10 ⁻⁵ ± 3.43 × 10 ⁻⁶	7.63 × 10 ⁻⁵ ± 6.20 × 10 ⁻⁶
80 g/L, 0.01 M							
forward average	3.96 ± 0.05	2.70 × 10 ⁻⁵ ± 8.62 × 10 ⁻⁶	6.76 ± 0.14	9.95 × 10 ⁻⁶ ± 2.47 × 10 ⁻⁶	9.30 ± 0.03	2.41 × 10 ⁻⁵ ± 6.34 × 10 ⁻⁶	6.10 × 10 ⁻⁵ ± 1.73 × 10 ⁻⁵
reverse average	3.91 ± 0.03	2.80 × 10 ⁻⁵ ± 8.59 × 10 ⁻⁶	6.68 ± 0.11	9.98 × 10 ⁻⁶ ± 2.38 × 10 ⁻⁶	9.28 ± 0.05	2.40 × 10 ⁻⁵ ± 6.22 × 10 ⁻⁶	6.20 × 10 ⁻⁵ ± 1.71 × 10 ⁻⁵
combined average	3.93 ± 0.05	2.75 × 10 ⁻⁵ ± 8.22 × 10 ⁻⁶	6.72 ± 0.13	9.96 × 10 ⁻⁶ ± 2.31 × 10 ⁻⁶	9.29 ± 0.04	2.40 × 10 ⁻⁵ ± 5.99 × 10 ⁻⁶	6.15 × 10 ⁻⁵ ± 1.64 × 10 ⁻⁵
100 g/L, 0.01 M							
forward average	3.52 ± 0.40	3.85 × 10 ⁻⁵ ± 7.59 × 10 ⁻⁶	5.64 ± 0.85	2.13 × 10 ⁻⁵ ± 8.26 × 10 ⁻⁶	9.10 ± 0.18	3.22 × 10 ⁻⁵ ± 2.64 × 10 ⁻⁶	9.20 × 10 ⁻⁵ ± 1.35 × 10 ⁻⁵
reverse average	3.67 ± 0.20	3.96 × 10 ⁻⁵ ± 6.97 × 10 ⁻⁶	5.80 ± 0.64	1.80 × 10 ⁻⁵ ± 3.86 × 10 ⁻⁶	9.14 ± 0.12	3.20 × 10 ⁻⁵ ± 3.13 × 10 ⁻⁶	8.96 × 10 ⁻⁵ ± 8.42 × 10 ⁻⁶
combined average	3.59 ± 0.31	3.90 × 10 ⁻⁵ ± 6.98 × 10 ⁻⁶	5.72 ± 0.72	1.97 × 10 ⁻⁵ ± 6.39 × 10 ⁻⁶	9.12 ± 0.15	3.21 × 10 ⁻⁵ ± 2.76 × 10 ⁻⁶	9.08 × 10 ⁻⁵ ± 1.08 × 10 ⁻⁵
0.01 M average	3.88 ± 0.26	3.30 × 10⁻⁵ ± 7.49 × 10⁻⁶	6.45 ± 0.63	1.37 × 10⁻⁵ ± 5.46 × 10⁻⁶	9.28 ± 0.14	2.95 × 10⁻⁵ ± 5.49 × 10⁻⁶	7.62 × 10⁻⁵ ± 1.60 × 10⁻⁵
40 g/L, 0.1 M							
forward average	3.90 ± 0.14	2.18 × 10 ⁻⁵ ± 2.76 × 10 ⁻⁶	6.70 ± 0.19	7.68 × 10 ⁻⁶ ± 4.46 × 10 ⁻⁷	9.16 ± 0.12	2.07 × 10 ⁻⁵ ± 1.17 × 10 ⁻⁶	5.02 × 10 ⁻⁵ ± 2.85 × 10 ⁻⁶
reverse average	4.08 ± 0.16	1.77 × 10 ⁻⁵ ± 2.71 × 10 ⁻⁶	6.78 ± 0.09	7.67 × 10 ⁻⁶ ± 3.26 × 10 ⁻⁷	9.20 ± 0.11	2.03 × 10 ⁻⁵ ± 1.15 × 10 ⁻⁶	4.56 × 10 ⁻⁵ ± 2.63 × 10 ⁻⁶
combined average	3.99 ± 0.17	1.97 × 10 ⁻⁵ ± 3.37 × 10 ⁻⁶	6.74 ± 0.14	7.67 × 10 ⁻⁶ ± 3.62 × 10 ⁻⁷	9.18 ± 0.11	2.05 × 10 ⁻⁵ ± 1.10 × 10 ⁻⁶	4.79 × 10 ⁻⁵ ± 3.54 × 10 ⁻⁶

TABLE C.1 (CONTINUED)

80 g/L, 0.1 M	pK_{a(1)}	[site 1]	pK_{a(2)}	[site 2]	pK_{a(3)}	[site 3]	Total sites
forward average	4.00 ± 0.22	1.72 × 10 ⁻⁵ ± 2.92 × 10 ⁻⁶	6.80 ± 0.17	6.54 × 10 ⁻⁶ ± 4.43 × 10 ⁻⁷	9.12 ± 0.10	1.95 × 10 ⁻⁵ ± 1.56 × 10 ⁻⁶	4.33 × 10 ⁻⁵ ± 1.78 × 10 ⁻⁶
reverse average	4.02 ± 0.28	1.66 × 10 ⁻⁵ ± 3.74 × 10 ⁻⁶	6.73 ± 0.19	6.61 × 10 ⁻⁶ ± 4.87 × 10 ⁻⁷	9.15 ± 0.10	1.90 × 10 ⁻⁵ ± 1.78 × 10 ⁻⁶	4.22 × 10 ⁻⁵ ± 2.48 × 10 ⁻⁶
combined average	4.01 ± 0.23	1.69 × 10 ⁻⁵ ± 3.12 × 10 ⁻⁶	6.77 ± 0.17	6.57 × 10 ⁻⁶ ± 4.32 × 10 ⁻⁷	9.14 ± 0.09	1.93 × 10 ⁻⁵ ± 1.57 × 10 ⁻⁶	4.28 × 10 ⁻⁵ ± 2.08 × 10 ⁻⁶
100 g/L, 0.1 M							
forward average	3.98 ± 0.10	1.67 × 10 ⁻⁵ ± 2.91 × 10 ⁻⁶	6.54 ± 0.12	5.61 × 10 ⁻⁶ ± 8.66 × 10 ⁻⁷	9.21 ± 0.08	1.73 × 10 ⁻⁵ ± 2.06 × 10 ⁻⁶	3.96 × 10 ⁻⁵ ± 5.74 × 10 ⁻⁶
reverse average	3.95 ± 0.12	1.70 × 10 ⁻⁵ ± 3.54 × 10 ⁻⁶	6.46 ± 0.11	5.91 × 10 ⁻⁶ ± 9.31 × 10 ⁻⁷	9.23 ± 0.07	1.72 × 10 ⁻⁵ ± 2.04 × 10 ⁻⁶	4.01 × 10 ⁻⁵ ± 6.41 × 10 ⁻⁶
combined average	3.96 ± 0.11	1.68 × 10 ⁻⁵ ± 3.13 × 10 ⁻⁶	6.50 ± 0.11	5.76 × 10 ⁻⁶ ± 8.83 × 10 ⁻⁷	9.22 ± 0.07	1.73 × 10 ⁻⁵ ± 1.98 × 10 ⁻⁶	3.99 × 10 ⁻⁵ ± 5.88 × 10 ⁻⁶
0.1 M average	3.98 ± 0.16	1.76 × 10⁻⁵ ± 3.33 × 10⁻⁶	6.63 ± 0.19	6.44 × 10⁻⁶ ± 1.04 × 10⁻⁶	9.19 ± 0.09	1.86 × 10⁻⁵ ± 2.17 × 10⁻⁶	4.26 × 10⁻⁵ ± 5.63 × 10⁻⁶
100 g/L, 0.3 M							
forward average	4.43 ± 0.15	5.19 × 10 ⁻⁶ ± 1.22 × 10 ⁻⁶	6.97 ± 0.17	5.81 × 10 ⁻⁶ ± 1.13 × 10 ⁻⁶	9.09 ± 0.10	1.71 × 10 ⁻⁵ ± 4.20 × 10 ⁻⁶	2.81 × 10 ⁻⁵ ± 4.04 × 10 ⁻⁶
reverse average	4.56 ± 0.16	4.68 × 10 ⁻⁶ ± 1.36 × 10 ⁻⁶	6.84 ± 0.16	4.72 × 10 ⁻⁶ ± 4.93 × 10 ⁻⁷	9.06 ± 0.11	1.76 × 10 ⁻⁵ ± 3.57 × 10 ⁻⁶	2.70 × 10 ⁻⁵ ± 4.43 × 10 ⁻⁶
combined average	4.50 ± 0.16	4.94 × 10 ⁻⁶ ± 1.22 × 10 ⁻⁶	6.90 ± 0.17	5.26 × 10 ⁻⁶ ± 9.94 × 10 ⁻⁷	9.07 ± 0.10	1.74 × 10 ⁻⁵ ± 3.62 × 10 ⁻⁶	2.76 × 10 ⁻⁵ ± 3.97 × 10 ⁻⁶

TABLE C.2

CALCULATED $\text{PK}_{A(i)}$ VALUES AND SITE CONCENTRATIONS (MOL/G) FROM
THE 3-SITE MODEL OF *S. ONEIDENSIS* EXUDATE TITRATIONS.

	$\text{pK}_{a(1)}$	[site 1]	$\text{pK}_{a(2)}$	[site 2]	$\text{pK}_{a(3)}$	[site 3]	Total sites
40 g/L, 0.01 M							
forward average	3.56 ± 0.41	8.91 × 10 ⁻⁶ ± 6.08 × 10 ⁻⁶	6.83 ± 0.03	6.32 × 10 ⁻⁶ ± 3.09 × 10 ⁻⁷	9.34 ± 0.02	2.20 × 10 ⁻⁵ ± 3.23 × 10 ⁻⁷	3.72 × 10 ⁻⁵ ± 5.92 × 10 ⁻⁶
reverse average	3.44 ± 0.06	8.85 × 10 ⁻⁶ ± 1.03 × 10 ⁻⁶	6.63 ± 0.07	6.68 × 10 ⁻⁶ ± 8.12 × 10 ⁻⁷	9.32 ± 0.02	2.22 × 10 ⁻⁵ ± 3.35 × 10 ⁻⁷	3.77 × 10 ⁻⁵ ± 8.62 × 10 ⁻⁷
combined average	3.50 ± 0.28	8.88 × 10 ⁻⁶ ± 4.04 × 10 ⁻⁶	6.73 ± 0.12	6.50 × 10 ⁻⁶ ± 6.00 × 10 ⁻⁷	9.33 ± 0.02	2.21 × 10 ⁻⁵ ± 3.20 × 10 ⁻⁷	3.75 × 10 ⁻⁵ ± 3.92 × 10 ⁻⁶
80 g/L, 0.01 M							
forward average	3.67 ± 0.10	7.56 × 10 ⁻⁶ ± 1.97 × 10 ⁻⁶	6.82 ± 0.04	5.88 × 10 ⁻⁶ ± 5.64 × 10 ⁻⁷	9.34 ± 0.02	2.18 × 10 ⁻⁵ ± 5.98 × 10 ⁻⁷	3.52 × 10 ⁻⁵ ± 2.91 × 10 ⁻⁶
reverse average	3.71 ± 0.09	7.01 × 10 ⁻⁶ ± 1.62 × 10 ⁻⁶	6.73 ± 0.03	6.01 × 10 ⁻⁶ ± 5.52 × 10 ⁻⁷	9.32 ± 0.02	2.11 × 10 ⁻⁵ ± 4.75 × 10 ⁻⁷	3.41 × 10 ⁻⁵ ± 2.54 × 10 ⁻⁶
combined average	3.69 ± 0.09	7.28 × 10 ⁻⁶ ± 1.69 × 10 ⁻⁶	6.77 ± 0.06	5.95 × 10 ⁻⁶ ± 5.22 × 10 ⁻⁷	9.33 ± 0.02	2.15 × 10 ⁻⁵ ± 6.27 × 10 ⁻⁷	3.47 × 10 ⁻⁵ ± 2.60 × 10 ⁻⁶
100 g/L, 0.01 M							
forward average	3.82 ± 0.07	7.49 × 10 ⁻⁶ ± 4.06 × 10 ⁻⁶	6.75 ± 0.13	5.64 × 10 ⁻⁶ ± 6.87 × 10 ⁻⁷	9.33 ± 0.01	2.18 × 10 ⁻⁵ ± 3.05 × 10 ⁻⁶	3.49 × 10 ⁻⁵ ± 7.79 × 10 ⁻⁶
reverse average	3.77 ± 0.07	7.82 × 10 ⁻⁶ ± 4.00 × 10 ⁻⁶	6.67 ± 0.13	5.78 × 10 ⁻⁶ ± 6.23 × 10 ⁻⁷	9.31 ± 0.01	2.11 × 10 ⁻⁵ ± 3.02 × 10 ⁻⁶	3.47 × 10 ⁻⁵ ± 7.64 × 10 ⁻⁶
combined average	3.79 ± 0.07	7.66 × 10 ⁻⁶ ± 3.74 × 10 ⁻⁶	6.71 ± 0.13	5.71 × 10 ⁻⁶ ± 6.11 × 10 ⁻⁷	9.32 ± 0.01	2.14 × 10 ⁻⁵ ± 2.83 × 10 ⁻⁶	3.48 × 10 ⁻⁵ ± 7.14 × 10 ⁻⁶
0.01 M average	3.66 ± 0.21	7.94 × 10⁻⁶ ± 3.25 × 10⁻⁶	6.74 ± 0.10	6.05 × 10⁻⁶ ± 6.49 × 10⁻⁷	9.32 ± 0.02	2.17 × 10⁻⁵ ± 1.64 × 10⁻⁶	3.57 × 10⁻⁵ ± 4.90 × 10⁻⁶
40 g/L, 0.1 M							
forward average	3.87 ± 0.23	1.16 × 10 ⁻⁵ ± 1.79 × 10 ⁻⁶	6.73 ± 0.02	1.11 × 10 ⁻⁵ ± 1.80 × 10 ⁻⁶	9.44 ± 0.04	4.27 × 10 ⁻⁵ ± 6.64 × 10 ⁻⁶	6.53 × 10 ⁻⁵ ± 8.09 × 10 ⁻⁶
reverse average	4.14 ± 0.44	9.16 × 10 ⁻⁶ ± 2.84 × 10 ⁻⁶	6.71 ± 0.01	1.11 × 10 ⁻⁵ ± 1.89 × 10 ⁻⁶	9.42 ± 0.07	4.11 × 10 ⁻⁵ ± 6.18 × 10 ⁻⁶	6.14 × 10 ⁻⁵ ± 6.40 × 10 ⁻⁶
combined average	4.01 ± 0.35	1.04 × 10 ⁻⁵ ± 2.55 × 10 ⁻⁶	6.72 ± 0.02	1.11 × 10 ⁻⁵ ± 1.71 × 10 ⁻⁶	9.43 ± 0.05	4.19 × 10 ⁻⁵ ± 6.00 × 10 ⁻⁶	6.33 × 10 ⁻⁵ ± 7.07 × 10 ⁻⁶
80 g/L, 0.1 M							
forward average	3.76 ± 0.06	1.73 × 10 ⁻⁵ ± 4.16 × 10 ⁻⁶	6.50 ± 0.16	9.99 × 10 ⁻⁶ ± 1.20 × 10 ⁻⁶	9.39 ± 0.06	3.31 × 10 ⁻⁵ ± 4.84 × 10 ⁻⁶	6.04 × 10 ⁻⁵ ± 1.05 × 10 ⁻⁶
reverse average	3.79 ± 0.05	1.68 × 10 ⁻⁵ ± 4.63 × 10 ⁻⁶	6.48 ± 0.13	1.01 × 10 ⁻⁵ ± 1.40 × 10 ⁻⁶	9.39 ± 0.04	3.23 × 10 ⁻⁵ ± 4.59 × 10 ⁻⁶	5.92 × 10 ⁻⁵ ± 1.43 × 10 ⁻⁶
combined average	3.78 ± 0.05	1.71 × 10 ⁻⁵ ± 4.08 × 10 ⁻⁶	6.49 ± 0.13	1.00 × 10 ⁻⁵ ± 1.21 × 10 ⁻⁶	9.39 ± 0.05	3.27 × 10 ⁻⁵ ± 4.39 × 10 ⁻⁶	5.98 × 10 ⁻⁵ ± 1.33 × 10 ⁻⁶
100 g/L, 0.1 M							
forward average	3.74 ± 0.07	1.63 × 10 ⁻⁵ ± 4.89 × 10 ⁻⁶	6.51 ± 0.15	1.04 × 10 ⁻⁵ ± 1.84 × 10 ⁻⁶	9.39 ± 0.05	3.26 × 10 ⁻⁵ ± 2.34 × 10 ⁻⁶	5.92 × 10 ⁻⁵ ± 4.43 × 10 ⁻⁶
reverse average	3.79 ± 0.02	1.54 × 10 ⁻⁵ ± 4.23 × 10 ⁻⁶	6.51 ± 0.08	1.04 × 10 ⁻⁵ ± 1.84 × 10 ⁻⁶	9.39 ± 0.03	3.19 × 10 ⁻⁵ ± 2.05 × 10 ⁻⁶	5.77 × 10 ⁻⁵ ± 4.02 × 10 ⁻⁶
combined average	3.76 ± 0.05	1.59 × 10 ⁻⁵ ± 4.26 × 10 ⁻⁶	6.51 ± 0.11	1.04 × 10 ⁻⁵ ± 1.70 × 10 ⁻⁶	9.39 ± 0.04	3.22 × 10 ⁻⁵ ± 2.07 × 10 ⁻⁶	5.85 × 10 ⁻⁵ ± 4.00 × 10 ⁻⁶
0.1 M average	3.85 ± 0.23	1.44 × 10⁻⁵ ± 4.63 × 10⁻⁶	6.57 ± 0.14	1.05 × 10⁻⁵ ± 1.55 × 10⁻⁶	9.40 ± 0.05	3.56 × 10⁻⁵ ± 6.23 × 10⁻⁶	6.05 × 10⁻⁵ ± 5.00 × 10⁻⁶

TABLE C.2 (CONTINUED)

100 g/L, 0.3 M	pK_{a(1)}	[site 1]	pK_{a(2)}	[site 2]	pK_{a(3)}	[site 3]	Total sites
forward average	4.20 ± 0.06	1.25 × 10 ⁻⁵ ± 3.40 × 10 ⁻⁶	6.44 ± 0.06	1.81 × 10 ⁻⁵ ± 2.84 × 10 ⁻⁶	9.34 ± 0.06	5.40 × 10 ⁻⁵ ± 5.32 × 10 ⁻⁶	8.45 × 10 ⁻⁵ ± 6.42 × 10 ⁻⁶
reverse average	4.35 ± 0.05	1.03 × 10 ⁻⁵ ± 3.45 × 10 ⁻⁶	6.34 ± 0.05	1.73 × 10 ⁻⁵ ± 2.42 × 10 ⁻⁶	9.23 ± 0.05	5.16 × 10 ⁻⁵ ± 5.44 × 10 ⁻⁶	7.92 × 10 ⁻⁵ ± 5.26 × 10 ⁻⁶
combined average	4.27 ± 0.06	1.15 × 10 ⁻⁵ ± 3.46 × 10 ⁻⁶	6.39 ± 0.06	1.77 × 10 ⁻⁵ ± 2.58 × 10 ⁻⁶	9.29 ± 0.06	5.29 × 10 ⁻⁵ ± 5.29 × 10 ⁻⁶	8.21 × 10 ⁻⁵ ± 6.30 × 10 ⁻⁶

REFERENCES

- Adams, L.K., D.Y. Lyon, and P.J.J. Alvarez. 2006. Comparative eco-toxicity of nanoscale TiO₂, SiO₂, and ZnO water suspensions. *Water Research* 40: 3527-3532.
- Aiken, G.R., D.M. McKnight, R.L. Wershaw, and P. MacCarthy, Eds. 1985. *Humic Substances in Soil, Sediment, and Water*. Wiley-Interscience: New York.
- Ams, D.A., J.B. Fein, H. Dong, and P.A. Maurice. 2004. Experimental measurements of the adsorption of *Bacillus subtilis* and *Pseudomonas mendocina* onto Fe-oxyhydroxide-coated and uncoated quartz grains. *Geomicrobiology Journal* 21: 511-519.
- Au, K.-K., A.C. Penisson, S. Yang, and C.R. O'Melia. 1999. Natural organic matter at oxide/water interfaces: Complexation and conformation. *Geochimica et Cosmochimica Acta* 63 (19/20): 2903-2917.
- Bennett, P.C., J.R. Rogers, W.J. Choi, and F.K. Hiebert. 2001. Silicates, silicate weathering, and microbial ecology. *Geomicrobiology Journal* 18: 3-19.
- Beveridge, T.J. and R.G.E. Murray. 1976. Uptake and retention of metals by cell walls of *Bacillus subtilis*. *Journal of Bacteriology* 127: 1502-1518.
- Beveridge, T.J. and R.G.E. Murray. 1980. Sites of metal deposition in the cell wall of *Bacillus subtilis*. *Journal of Bacteriology* 141: 876-887.
- Beveridge, T.J. 1989. Role of cellular design in bacterial metal accumulation and mineralization. *Annual Reviews in Microbiology* 43: 147-171.
- Borch, T., R. Kretzschmar, A. Kappler, P. van Cappellen, M. Ginder-Vogel, A. Voegelin, and K. Campbell. 2010. Biogeochemical redox processes and their impact on contaminant dynamics. *Environmental Science and Technology* 44 (1): 15-23.
- Borrok, D., B.F. Turner, and J.B. Fein. 2005. A universal surface complexation framework for modeling proton binding onto bacterial surfaces in geologic settings. *American Journal of Science* 305 (6-8): 826-853.

- Brantley, S.L. and Y. Chen. 1995. Chemical weathering rates of pyroxenes and amphiboles. *Reviews in Mineralogy: Chemical Weathering Rates of Silicate Minerals* 31: 119-172.
- Brown, G.E., Jr. and G.A. Parks. 2001. Sorption of trace elements on mineral surfaces: modern perspectives from spectroscopic studies, and comments on sorption in the marine environment. *International Geology Review* 43 (11): 963-1073.
- Brunet, L., D.Y. Lyon, E.M. Hotze, P.J.J. Alvarez, and M.R. Wiesner. 2009. Comparative photoactivity and antibacterial properties of C₆₀ fullerenes and titanium dioxide nanoparticles. *Environmental Science and Technology* 43 (12): 4355-4360.
- Cabaniss, S.E., Q. Zhou, P.A. Maurice, Y.-P. Chin, and G.R. Aiken. 2000. A log-normal distribution model for the molecular weight of aquatic fulvic acids. *Environmental Science and Technology* 34 (6): 1103-1109.
- Chernyshova, I.V., M.F. Hochella, Jr., and A.S. Madden. 2007. Size-dependent structural transformations of hematite nanoparticles. 1. Phase transition. *Physical Chemistry Chemical Physics* 9: 1735-1750.
- Chi, F.-H. and G.L. Amy. 2004. Kinetic study on the sorption of dissolved natural organic matter onto different aquifer materials: the effects of hydrophobicity and functional groups. *Journal of Colloid and Interface Science* 274: 380-391.
- Chin, Y.-P., G. Aiken, and E. O'Loughlin. 1994. Molecular weight, polydispersity, and spectroscopic properties of aquatic humic substances. *Environmental Science and Technology* 28 (11): 1853-1858.
- Chorover, J., R. Kretzschmar, F. Garcia-Pichel, and D.L. Sparks. 2007. Soil biogeochemical processes within the critical zone. *Elements* 3: 321-326.
- Choy, C.C., M. Wazne, and X. Meng. 2008. Application of an empirical transport model to simulate retention of nanocrystalline titanium dioxide in sand columns. *Chemosphere* 71: 1794-1801.
- Collins, C.R., K.V. Ragnarsdottir, and D.M. Sherman. 1999. Effect of inorganic and organic ligands on the mechanism of cadmium sorption to goethite. *Geochimica et Cosmochimica Acta* 63 (19/20): 2989-3002.
- Darlington, T.K., A.M. Neigh, M.T. Spencer, O.T. Nguyen, and S.J. Oldenburg. 2009. Nanoparticle characteristics affecting environmental fate and transport through soil. *Environmental Toxicology and Chemistry* 28 (6): 1191-1199.
- Domingos, R.F., N. Tufenkji, and K.J. Wilkinson. 2009. Aggregation of titanium dioxide nanoparticles: role of a fulvic acid. *Environmental Science and Technology* 43 (5): 1282-1286.

- Dong, H., T.C. Onstott, M.F. DeFlaun, M.E. Fuller, T.D. Scheibe, S.H. Streger, R.K. Rothmel, and B.J. Mailloux. 2002. Relative dominance of physical versus chemical effects on the transport of adhesion-deficient bacteria in intact cores from South Oyster, Virginia. *Environmental Science and Technology* 36 (5): 891-900.
- Dunnivant, F.M., P.M. Jardine, D.L. Taylor, and J.F. McCarthy. 1992. Transport of naturally occurring dissolved organic carbon in laboratory columns containing aquifer material. *Soil Science Society of America Journal* 56: 437-444.
- Dunphy Guzman, K.A., M.P. Finnegan, and J.F. Banfield. 2006. Influence of surface potential on aggregation and transport of titania nanoparticles. *Environmental Science and Technology* 40 (24): 7688-7693.
- Fang, J., X.-Q. Shan, B. Wen, J.-M. Lin, and G. Owens. 2009. Stability of titania nanoparticles in soil suspensions and transport in saturated homogeneous soil columns. *Environmental Pollution* 157: 1101-1109.
- Fatissou, J., R.F. Domingos, K.J. Wilkinson, and N. Tufenkji. 2009. Deposition of TiO₂ nanoparticles onto silica measured using a quartz crystal microbalance with dissipation monitoring. *Langmuir* 25 (11): 6062-6069.
- Fein, J.B., J.-F. Boily, N. Yee, D. Gorman-Lewis, and B.F. Turner. 2005. Potentiometric titrations of *Bacillus subtilis* cells to low pH and a comparison of modeling approaches. *Geochimica et Cosmochimica Acta* 69 (5): 1123-1132.
- Filius, J.D., D.G. Lumsdon, J.C.L. Meeussen, T.Hiemstra, and W.H. Van Riemsdijk. 2000. Adsorption of fulvic acid on goethite. *Geochimica et Cosmochimica Acta* 64 (1): 51-60.
- Fortin, D. and T.J. Beveridge. 1997. Role of the bacterium *Thiobacillus* in the formation of silicates in acidic mine tailings. *Chemical Geology* 141: 235-250.
- French, R.A., A.R. Jacobson, B. Kim, S.L. Isley, R.L. Penn, and P.C. Baveye. 2009. Influence of ionic strength, pH, and cation valence on aggregation kinetics of titanium dioxide nanoparticles. *Environmental Science and Technology* 43 (5): 1354-1359.
- Freeze, R.A. and J.A. Cherry. 1979. *Groundwater*. Prentice-Hall: New Jersey.
- Frimmel, F.H. and L. Huber. 1996. Influence of humic substances on the aquatic adsorption of heavy metals on defined mineral phases. *Environmental International* 22 (5): 507-517.
- Gao, Y., R. Wahi, A.T. Kan, J.C. Falkner, V.L. Colvin, and M.B. Tomson. 2004. Adsorption of cadmium on anatase nanoparticles—Effect of crystal size and pH. *Langmuir* 20: 9585-9593.

- Giammar, D.E., C.J. Maus, and L. Xie. 2007. Effects of particle size and crystalline phase on lead adsorption to titanium dioxide nanoparticles. *Environmental Engineering Science* 24 (1): 85-95.
- Gu, B., T.L. Mehlhorn, L. Liang, and J.F. McCarthy. 1996. Competitive adsorption, displacement, and transport of organic matter on iron oxide: II. Displacement and transport. *Geochimica et Cosmochimica Acta* 60 (16): 2977-2992.
- Guo, M. and J. Chorover. 2003. Transport and fractionation of dissolved organic matter in soil columns. *Soil Science* 168 (2): 108-118.
- Ha, J., A. Gélabert, A.M. Spormann, and G.E. Brown, Jr. 2010. Role of extracellular polymeric substances in metal ion complexation on *Shewanella oneidensis*: Batch uptake, thermodynamic modeling, ATR-FTIR, and EXAFS study. *Geochimica et Cosmochimica Acta* 74: 1-15.
- He, Y.T., J. Wan, and T. Tokunaga. 2008. Kinetic stability of hematite nanoparticles: the effect of particle sizes. *Journal of Nanoparticle Research* 10: 321-332.
- Hernes, P.J. and R. Benner. 2003. Photochemical and microbial degradation of dissolved lignin phenols: implications for the fate of terrigenous dissolved organic matter in marine environments. *Journal of Geophysical Research* 108 (C9): 3291-3299.
- Hochella, M.F., Jr., S.K. Lower, P.A. Maurice, R.L. Penn, N. Sahai, D.L. Sparks, and B.S. Twining. 2008. Nanominerals, mineral nanoparticles, and earth systems. *Science* 319: 1631-1635.
- Hur, J. and M.A. Schlautman. 2003. Molecular weight fractionation of humic substances by adsorption onto minerals. *Journal of Colloid and Interface Science* 264: 313-321.
- Jiang, J., D.-R. Chen, and P. Biswas. 2007. Synthesis of nanoparticles in a flame aerosol reactor with independent and strict control of their size, crystal phase and morphology. *Nanotechnology* 18: 1-8.
- Jiang, J., G. Oberdörster, A. Elder, R. Gelein, P. Mercer, and P. Biswas. 2008. Does nanoparticle activity depend upon size and crystal phase? *Nanotoxicology* 2 (1-4): 33-42.
- Jiang, J., G. Oberdörster, and P. Biswas. 2009. Characterization of size, surface charge, and agglomeration state of nanoparticle dispersions for toxicological studies. *Journal of Nanoparticle Research* 11: 77-89.
- Joo, S.H., S.R. Al-Abed, and T. Luxton. 2009. Influence of carboxymethyl cellulose for the transport of titanium dioxide nanoparticles in clean silica and mineral-coated sands. *Environmental Science and Technology* 43 (13): 4954-4959.

- Kaegi, R., A. Ulrich, B. Sinnet, R. Vonbank, A. Wichser, S. Zuleeg, H. Simmler, S. Brunner, H. Vonmont, M. Burkhardt, and M. Boller. 2008. Synthetic TiO₂ nanoparticle emission from exterior facades into the aquatic environment. *Environmental Pollution* 156: 233-239.
- Kaiser, K. and W. Zech. 1999. Release of Natural Organic Matter Sorbed to Oxides and a Subsoil. *Soil Science Society of America Journal* 63: 1157-1166.
- Kaulbach, E.S., J.E.S. Szymanowski, and J.B. Fein. 2005. Surface complexation modeling of proton and Cd adsorption onto an algal cell wall. *Environmental Science and Technology* 39 (11): 4060-4065.
- Kenney, J.P.L., Z. Song, B.A. Bunker, and J.B. Fein. (2010, submitted.) An experimental study of Au removal from solution by bacterial cells. Part 1: Aqueous chemistry results. *Geochimica et Cosmochimica Acta*.
- Koretsky, C. 2000. The significance of surface complexation reactions in hydrologic systems: A geochemist's perspective. *Journal of Hydrology* 230: 127-171.
- Kretzschmar, R. and T. Schäfer. 2005. Metal retention and transport on colloidal particles in the environment. *Elements* 1: 205-210.
- Langmuir, D. 1997. *Aqueous Environmental Geochemistry*. Prentice-Hall: Upper Saddle River.
- Lecoanet, H.F., J.-Y. Bottero, and M.R. Wiesner. 2004. Laboratory assessment of the mobility of nanomaterials in porous media. *Environmental Science and Technology* 38 (19): 5164-5169.
- Lee, J.-U. and J.B. Fein. 2000. Experimental study of the effects of *Bacillus subtilis* on gibbsite dissolution rates under near-neutral pH and nutrient-poor conditions. *Chemical Geology* 166: 193-202.
- Limbach, L.K., P. Wick, P. Manser, R.N. Grass, A. Bruinink, and W.J. Stark. 2007. Exposure of engineered nanoparticles to human lung epithelial cells: Influence of chemical composition and catalytic activity on oxidative stress. *Environmental Science and Technology* 41 (11): 4158-4163.
- Long, T.C., N. Saleh, R.D. Tilton, G.V. Lowry, and B. Veronesi. 2006. Titanium dioxide (P25) produces reactive oxygen species in immortalized brain microglia (BV2): implications for nanoparticle neurotoxicity. *Environmental Science and Technology* 40 (14): 4346-4352.
- Lovely, D.R. 1993. Dissimilatory metal reduction. *Annual Reviews in Microbiology* 47: 263-290.

- Martell, A.E. and R.M. Smith, Eds. 2001. NIST Critically selected stability constants of metal complexes. NIST Standard Reference Database 46, Version 6.0.
- Mattigod, S.V., G.E. Fryxell, K. Alford, T. Gilmore, K. Parker, J. Serne, and M. Engelhard. 2005. Functionalized TiO₂ nanoparticles for use in situ anion immobilization. *Environmental Science and Technology* 39 (18): 7306-7310.
- McKnight, D.M., K.E. Bencala, G.W. Zellweger, G.R. Aiken, G.L. Feder, and K.A. Thorn. 1992. Sorption of dissolved organic carbon by hydrous aluminum and iron oxides occurring at the confluence of Deer Creek with the Snake River, Summit County, Colorado. *Environmental Science and Technology* 26 (7): 1388-1396.
- Meier, M., K. Namjesnik-Dejanovic, P.A. Maurice, Y.-P. Chin, and G.R. Aiken. 1999. Fractionation of aquatic natural organic matter upon sorption to goethite and kaolinite. *Chemical Geology* 157: 275-284.
- Michel, F.M., L. Ehm, S.M. Antao, P.L. Lee, P.J. Chupas, G. Liu, D.R. Strongin, M.A.A. Schoonen, B.L. Phillips, and J.B. Parise. 2007. The structure of ferrihydrite, a nanocrystalline mineral. *Science* 316: 1726-1729.
- Mishra, B., M. Boyanov, B.A. Bunker, S.D. Kelly, K.M. Kemner, and J.B. Fein. 2010. High- and low-affinity binding sites for Cd on the bacterial cell walls of *Bacillus subtilis* and *Shewanella oneidensis*. *Geochimica et Cosmochimica Acta* 74: 4219-4233.
- Mrozik, A. and Z. Piotrowska-Seget. 2010. Bioaugmentation as a strategy for cleaning up of soils contaminated with aromatic compounds. *Microbiological Research* 165: 363-375.
- Münch, J.-M., K.U. Totsche, and K. Kaiser. 2002. Physicochemical factors controlling the release of dissolved organic carbon from columns of forest subsoils. *European Journal of Soil Science* 53: 311-320.
- Namjesnik-Dejanovic, K. and P.A. Maurice. 2000. Conformations and aggregate structures of sorbed natural organic matter on muscovite and hematite. *Geochimica et Cosmochimica Acta* 65 (7): 1047-1057.
- Namjesnik-Dejanovic, K., P.A. Maurice, G.R. Aiken, S. Cabaniss, Y.-P. Chin, and M.J. Pullin. 2000. Adsorption and fractionation of a muck fulvic acid on kaolinite and goethite at pH 3.7, 6, and 8. *Soil Science* 165 (7): 545-559.
- Nel, A., T. Xia, L. Mädler, and N. Li. 2006. Toxic potential of materials at the nanolevel. *Science* 311: 622-627.
- Newman, D.K. and J.F. Banfield. 2002. Geomicrobiology: How molecular-scale interactions underpin biogeochemical systems. *Science* 296: 1071-1077.

- Nugent, M.A., S.L. Brantley, C.G. Pantano, and P.A. Maurice. 1998. The influence of natural mineral coatings on feldspar weathering. *Nature* 395: 588-591.
- Ohnuki, T., T. Yoshida, T. Ozaki, N. Kozai, F. Sakamoto, T. Nankawa, Y. Suzuki, and A.J. Francis. 2007. Chemical speciation and association of plutonium with bacteria, kaolinite clay, and their mixture. *Environmental Science and Technology* 41 (9): 3134-3139.
- Oyama, T., I. Yanagisawa, M. Takeuchi, T. Koike, N. Serpone, and H. Hidaka. 2009. Remediation of simulated aquatic sites contaminated with recalcitrant substrates by TiO₂/ozonation under natural sunlight. *Applied Catalysis B: Environmental* 91: 242-246.
- Pena, M.E., G.P. Korfiatis, M. Patel, L. Lippincott, and X. Meng. 2005. Adsorption of As(V) and As(III) by nanocrystalline titanium dioxide. *Water Research* 39: 2327-2337.
- Penn, R.L., C. Zhu, H. Xu, and D.R. Veblen. 2001. Iron oxide coatings on sand grains from the Atlantic coastal plain: High-resolution transmission electron microscopy characterization. *Geology* 29 (9): 843-846.
- Perry, T.D., C.J. McNamara, R. Mitchell, and G. Hernandez-Duque. 2003. An investigation of bacterial dissolution of Maya limestone: Biodiversity and functional analysis. *Molecular Biology and Cultural Heritage* 137-140.
- Perry, T.D., IV, V. Klepac-Ceraj, X.V. Zhang, C.J. McNamara, M.F. Polz, S.T. Martin, N. Berke, and R. Mitchell. 2005. Binding of harvested bacterial exopolymers to the surface of calcite. *Environmental Science and Technology* 39 (22): 8770-8775.
- Pettibone, J.M., D.M. Cwiertny, M. Scherer, and V.H. Grassian. 2008. Adsorption of organic acids on TiO₂ nanoparticles: effects of pH, nanoparticle size, and nanoparticle aggregation. *Langmuir* 24: 6659-6667.
- Pokrovsky, O.S., L.S. Shirokova, P. Bénézech, J. Schott, and S.V. Golubev. 2009. Effect of organic ligands and heterotrophic bacteria on wollastonite dissolution kinetics. *American Journal of Science* 309: 731-772.
- Pullin, M.J., C.A. Prosser, and P.A. Maurice. 2004. Effects of photoirradiation on the adsorption of dissolved organic matter to goethite. *Geochimica et Cosmochimica Acta* 68 (18): 3643-3656.
- Ridley, M.K., V.A. Hackley, and M.L. Machesky. 2006. Characterization and surface-reactivity of nanocrystalline anatase in aqueous solutions. *Langmuir* 22: 10972-10982.

- Ryan, J.N. and P.M. Gschwend. 1990. Colloid mobilization in two Atlantic coastal plain aquifers: Field studies. *Water Resources Research* 26 (2): 307-322.
- Saito, T., L.K. Koopal, W.H. van Riemsdijk, S. Nagasaki, and S. Tanaka. 2004. Adsorption of humic acid on goethite: Isotherms, charge adjustments, and potential profiles. *Langmuir* 20: 689-700.
- Schlautman, M.A. and J.J. Morgan. 1994. Adsorption of aquatic humic substances on colloidal-size aluminum oxide particles: influence of solution chemistry. *Geochimica et Cosmochimica Acta* 58 (20): 4293-4303.
- Serkiz, S.M. and E.M. Perdue. 1990. Isolation of dissolved organic matter from the Suwannee River using reverse osmosis. *Water Research* 24 (7): 911-916.
- Simon-Deckers, A., B. Gouget, M. Mayne-L'Hermite, N. Herlin-Boime, C. Reynaud, and M. Carrière. 2008. *In vitro* investigation of oxide nanoparticle and carbon nanotube toxicity and intracellular accumulation in A549 human pneumocytes. *Toxicology* 253: 137-146.
- Stumm, W. 1992. *Chemistry of the Solid-Water Interface*. John Wiley & Sons: New York.
- Sun, L., E.M. Perdue, and J.F. McCarthy. 1995. Using reverse osmosis to obtain organic matter from surface and ground waters. *Water Research* 29 (6): 1471-1477.
- Theng, B.K.G. and G. Yuan. 2008. Nanoparticles in the soil environment. *Elements* 4: 395-399.
- Theron, J., J.A. Walker, and T.E. Cloete. 2008. Nanotechnology and water treatment: applications and emerging opportunities. *Critical Reviews in Microbiology* 34: 43-69.
- Tipping, E. 1981. The adsorption of aquatic humic substances by iron oxides. *Geochimica et Cosmochimica Acta* 45 (2): 191-199.
- Tiquia, S.M. 2010. Salt-adapted bacteria isolated from the Rouge River and potential for degradation of contaminants and biotechnological applications. *Environmental Technology* 31 (8-9): 967-978.
- Tkachenko, N.H., Z.M. Yaremko, C. Bellmann, and M.M. Soltys. 2006. The influence of ionic and nonionic surfactants on aggregative stability and electrical surface properties of aqueous suspensions of titanium dioxide. *Journal of Colloid and Interface Science* 299: 686-695.
- Traina, S.J., J. Novak, and N.E. Smeck. 1990. An ultraviolet absorbance method of estimating the percent aromatic carbon content of humic acids. *Journal of Environmental Quality* 19: 151-153.

- Venkateswaran, K., D.P. Moser, M.E. Dollhopf, D.P. Lies, D.A. Saffarini, B.J. MacGregor, D.B. Ringelberg, D.C. White, M. Nishijima, H. Sano, J. Burghardt, E. Stackebrandt, and K.H. Neelson. 1999. Polyphasic taxonomy of the genus *Shewanella* and description of *Shewanella oneidensis* sp. nov. *International Journal of Systematic Bacteriology* 49 (2): 705-724
- Vermeer, A.W.P., W.H. van Riemsdijk, and L.K. Koopal. 1998. Adsorption of humic acid to mineral particles. 1. Specific and electrostatic interactions. *Langmuir* 14: 2810-2819.
- Vermeer, A.W.P., J.K. McCulloch, W.H. Van Riemsdijk, and L.K. Koopal. 1999. Metal ion adsorption to complexes of humic acid and metal oxides: Deviations from the additivity rule. *Environmental Science and Technology* 33 (21): 3892-3897.
- Wang, J.J., B.J.S. Sanderson, and H. Wang. 2007. Cyto- and genotoxicity of ultrafine TiO₂ particles in cultured human lymphoblastoid cells. *Mutation Research* 628: 99-106.
- Waychunas, G.A., C.S. Kim, and J.F. Banfield. 2005. Nanoparticle iron oxide minerals in soils and sediments: Unique properties and contaminant scavenging mechanisms. *Journal of Nanoparticle Research* 7: 409-433.
- Wei, X., M. Shao, R. Horton, and X. Han. 2010. Humic acid transport in water-saturated porous media. *Environmental Modeling and Assessment* 15: 53-63.
- Weigand, H. and K.U. Totsche. 1998. Flow and reactivity effects on dissolved organic matter transport in soil columns. *Soil Science Society of America Journal* 62 (5): 1268-1274.
- Weng, L., W.H. Van Riemsdijk, L.K. Koopal, and T. Hiemstra. 2006. Adsorption of humic substances on goethite: Comparison between humic acids and fulvic acids. *Environmental Science and Technology* 40 (24): 7494-7500.
- Wershaw, R.L., E.C. Llaguno, and J.A. Leenheer. 1996. Mechanism of formation of humus coatings on mineral surfaces 3. Composition of adsorbed organic acids from compost leachate on alumina by solid-state ¹³C NMR. *Colloids and Surfaces A: Physicochemical and Engineering Aspects* 108: 213-223.
- Westall, J.C. 1982. FITEQL, A computer program for determination of chemical equilibrium constants from experimental data. Version 2.0. Report 82-02, Dept. of Chemistry, Oregon State Univ., Corvallis, Oregon.
- Westall, J.C., J.D. Jones, G.D. Turner, and J.M. Zachara. 1995. Models for association of metal ions with heterogeneous environmental sorbents. 1. Complexation of Co(II) by Leonardite humic acid as a function of pH and NaClO₄ concentration. *Environmental Science and Technology* 29 (4): 951-959.

- Wiesner, M.R., G.V. Lowry, P. Alvarez, D. Dionysiou, and P. Biswas. 2006. Assessing the risks of manufactured nanomaterials. *Environmental Science and Technology* 40 (14): 4336-4345.
- Young, K.C., K.M. Docherty, P.A. Maurice, and S.D. Bridgham. 2005. Degradation of surface-water dissolved organic matter: influences of DOM chemical characteristics and microbial populations. *Hydrobiologia* 539: 1-11.
- Zhang, H., B. Chen, and J.F. Banfield. 2009. The size dependence of the surface free energy of titania nanocrystals. *Physical Chemistry Chemical Physics* 11: 2553-2558.
- Zhou, Q., S.E. Cabaniss, and P.A. Maurice. 2000. Considerations in the use of high-pressure size exclusion chromatography (HPSEC) for determining molecular weights of aquatic humic substances. *Water Research* 34 (14): 3505-3514.
- Zhou, Q., P.A. Maurice, and S.E. Cabaniss. 2001. Size fractionation upon adsorption of fulvic acid on goethite: equilibrium and kinetic studies. *Geochimica et Cosmochimica Acta* 65 (5): 803-812.